

11-25-82  
566/3  
p-157

ORIGINAL CONTAINS  
UNCLAS ILLUSTRATIONS  
2

# Final Report on the NASA/JPL Evaluation of Oxygen Interactions with Materials-3 (EOIM-3)

David E. Brinza  
Shirley Y. Chung  
Timothy K. Minton  
Ranty H. Liang

N95-31660

Unclass

G3/25 0056613

December 1994



National Aeronautics and  
Space Administration

Jet Propulsion Laboratory  
California Institute of Technology  
Pasadena, California

(NASA-CR-198865) THE NASA/JPL  
EVALUATION OF OXYGEN INTERACTIONS  
WITH MATERIALS-3 (EOIM-3) Final  
Report (JPL) 107 p



# Final Report on the NASA/JPL Evaluation of Oxygen Interactions with Materials-3 (EOIM-3)

David E. Brinza  
Shirley Y. Chung  
Timothy K. Minton  
Ranty H. Liang

December 1994



National Aeronautics and  
Space Administration

Jet Propulsion Laboratory  
California Institute of Technology  
Pasadena, California



The research described in this publication was carried out by the Jet Propulsion Laboratory, California Institute of Technology, under a contract with the National Aeronautics and Space Administration.

Reference herein to any specific commercial product, process, or service by trade name, trademark, manufacturer, or otherwise, does not constitute or imply its endorsement by the United States Government or the Jet Propulsion Laboratory, California Institute of Technology.



# TABLE OF CONTENTS

<b>ABSTRACT</b> . . . . .	1
<b>1.0 Introduction</b> . . . . .	2
<b>2.0 STS-46 and EOIM-3 Overview</b> . . . . .	4
2.1 EOIM Integration . . . . .	4
2.2 STS-46 Mission Timeline . . . . .	4
2.3 Atomic Oxygen Environment . . . . .	6
2.4 Solar UV Environment . . . . .	8
2.5 Thermal Environment . . . . .	8
2.6 Flight Contamination . . . . .	8
2.7 Post-Flight Inspection . . . . .	13
<b>3.0 EOIM-3 Experiment</b> . . . . .	15
3.1 Sample Handling . . . . .	15
3.2 Sample Characterization Methods . . . . .	15
3.2.1 Photography . . . . .	15
3.2.2 Electron Spectroscopy for Chemical Analysis . . . . .	17
3.2.3 Weight Measurement . . . . .	17
3.2.4 Scanning Electron Microscopy . . . . .	18
3.2.5 High-Performance Liquid Chromatography . . . . .	18
3.2.6 Spectral Reflectance . . . . .	18
3.3 Passive Tray Experiment . . . . .	20
3.3.1 Fluorinated Polystyrene Materials . . . . .	20
3.3.2 Spectrolon . . . . .	22
3.3.3 White Paints . . . . .	22
3.4 Heated Tray and Heated Strip Experiments . . . . .	22
3.4.1 Carbon/Carbon Materials . . . . .	22
3.4.2 Advanced Photovoltaic Solar Array (APSA) Substrates . . . . .	23
3.4.3 Polycyanate and Modified-Polycyanate Resins . . . . .	23
3.5 Scatterometer . . . . .	24
3.6 Solar UV Experiment . . . . .	24
3.7 Variable Exposure Experiment . . . . .	24
3.8 Mass Spectrometer and Carousel . . . . .	26
3.9 Ground-Based Scattering Measurements . . . . .	26
<b>4.0 Results and Discussion</b> . . . . .	35
4.1 Passive Tray Samples . . . . .	35
4.1.1 Fluorinated Polystyrene Materials . . . . .	35
4.1.2 Spectrolon . . . . .	35
4.1.3 White Paints . . . . .	37
4.2 Heated Tray and Heated Strip Samples . . . . .	37
4.2.1 Carbon/Carbon Materials . . . . .	37

## TABLE OF CONTENTS (continued)

4.2.2	<i>APSA Substrates</i>	41
4.2.3	<i>Polycyanate and Modified-Polycyanate Resins</i>	51
4.3	<b>Scatterometer Samples</b>	51
4.4	<b>Solar UV Samples</b>	56
4.5	<b>Variable Exposure Samples</b>	66
4.6	<b>AO/Kapton Scattering Results</b>	67
4.6.1	<i>EOIM-3 Mass Spectra</i>	67
4.6.2	<i>Laboratory Mass Spectra</i>	69
4.6.3	<i>Inelastic Scattering of Oxygen</i>	69
4.6.4	<i>Reactive Scattering of Fast Oxygen and Kapton</i>	71
4.6.5	<i>Comparison of Lab and Space Results</i>	76
5.0	<b>Summary and Conclusions</b>	79
6.0	<b>Acknowledgements</b>	80
7.0	<b>References</b>	81

### List of Figures

2-1.	Sketch showing EOIM-3 experiment pallet location in Shuttle Bay 12	5
2-2.	Orbital history of atomic oxygen density during EOIM-3.	7
2-3.	Temperature history of passive tray N-8.	9
2-4.	Temperature history of 333 K (60°C) tray.	10
2-5.	Temperature history of 473 K (200°C) tray.	11
2-6.	Temperature history of composite stress fixture H2 near scatterometers.	12
3-1.	The EOIM-3 experiment pallet.	16
3-2.	SEM images of mesas used to determine erosion depths [see text for descriptions of (a), (b), and (c)].	19
3-3.	Polystyrene and the fluorinated analogues studied on EOIM-3.	21
3-4.	EOIM-3 scatterometer design.	25
3-5.	Key steps in the synthesis of <sup>13</sup> C-enriched "Kapton."	27
3-6.	Schematic diagram of molecular beam apparatus.	28
3-7.	Time-of-flight distributions of the molecular beam collected at two masses.	31
3-8.	Time-of-flight and translational energy distributions of the O-atom component in the molecular beam.	33



## TABLE OF CONTENTS (continued)

### List of Figures (continued)

3-9.	Time-of-flight and translational energy distributions of the fast O <sub>2</sub> component in the molecular beam. . . . .	34
4-1.	SEM photographs of polystyrene: (a) control, (b) ring-fluorinated, and (c) backbone-fluorinated. . . . .	36
4-2.	Spectral reflectance for exposed (lower) and control (upper) 100-percent reflectance Spectrolon. . . . .	38
4-3.	Photograph of the heated strip APSA samples: (a) preflight and (b) postflight. . . . .	39
4-4.	Postflight photograph of TS15 carbon/carbon composite samples in the heated tray experiment . . . . .	40
4-5.	SEM photographs of TS15 carbon/carbon composite: a) control, b) ambient, c) 333 K (60°C), and d) 473 K (200°C). . . . .	42
4-6.	SEM photographs of SP16 carbon/carbon composite: a) control, b) ambient, c) 333 K (60°C), and d) 473 K (200°C). . . . .	43
4-7.	SEM photographs of SP18 carbon/carbon composite: a) control, b) ambient, c) 333 K (60°C), and d) 473 K (200°C). . . . .	44
4-8.	SEM photographs of unprotected Kapton: a) ambient, b) 333 K (60°C), and c) 473 K (200°C). . . . .	45
4-9.	SEM photographs of carbon-loaded Kapton: a) 333 K (60°C) and b) 473 K (200°C). . . . .	46
4-10.	SEM photographs of SiO <sub>x</sub> -coated Kapton: a) 333 K (60°C) and b) 473 K (200°C). . . . .	47
4-11.	SEM photographs of ITO-coated Kapton: a) 333 K (60°C) and b) 473 K (200°C). . . . .	49
4-12.	SEM photographs of Ge-coated Kapton: a) 333 K (60°C) and b) 473 K (200°C). . . . .	50
4-13.	SEM photographs of base polycyanate: a) control and b) 333 K (60°C). . . . .	52
4-14.	SEM photographs of siloxane-modified polycyanate: a) control and b) 333 K (60°C). . . . .	53
4-15.	SEM photographs of Kapton-HN scatterometer sample with SiO <sub>2</sub> as the scattering surface: (a) surface protected under rim of clamp and (b) exposed region. . . . .	55
4-16.	SEM photographs of polysulfone: a) day, b) night, c) control, and d) day and night exposure. . . . .	57

## TABLE OF CONTENTS (continued)

### List of Figures (continued)

4-17.	SEM photographs of PMMA: a) day, b) night, c) control, and d) day and night exposure. . . . .	58
4-18.	SEM photographs of polystyrene: a) day, b) night, c) control, and d) day and night exposure. . . . .	59
4-19.	HPLC traces for SUV1: polysulfone . . . . .	63
4-20.	HPLC traces for SUV2: PMMA . . . . .	64
4-21.	HPLC traces for SUV4: polystyrene . . . . .	65
4-22.	Mass spectra taken with EOIM-3 mass spectrometer viewing $^{13}\text{C}$ -enriched Kapton on the carousel. . . . .	68
4-23.	Time-of-flight distributions of O and $\text{O}_2$ scattered from a $^{13}\text{C}$ -enriched Kapton surface. . . . .	70
4-24.	Time-of-flight distributions of $\text{CO}_2$ products emerging from Kapton HN ( $^{12}\text{C}$ Kapton) and $^{13}\text{C}$ -enriched Kapton surfaces. . . . .	72
4-25.	Time-of-flight distributions of CO products emerging from Kapton HN ( $^{12}\text{C}$ Kapton) and $^{13}\text{C}$ -enriched Kapton surfaces. . . . .	74
4-26.	Time-of-flight distributions of $\text{H}_2\text{O}$ and NO products emerging from Kapton HN ( $^{12}\text{C}$ Kapton) and $^{13}\text{C}$ -enriched Kapton surfaces. . . . .	75
4-27.	Comparison of mass spectra collected in space (top and bottom panels) and in the laboratory (center panel). . . . .	77

### List of Tables

Table 3-1.	Molecular weight distributions of polystyrenes. . . . .	20
Table 4-1.	Temperature dependence of atomic oxygen erosion and thermo-optical properties of EOIM-3 carbon/carbon composite. . . . .	41
Table 4-2.	Temperature dependence of oxide layer thickness for EOIM-3 germanium-coated Kapton. . . . .	48
Table 4-3.	Mass loss and erosion data for EOIM-3 solar UV specimens. . . . .	60

## **TABLE OF CONTENTS (continued)**

### **List of Tables (continued)**

Table 4-4.	Comparison of day and night erosion of EOIM-3 solar UV specimens. . . . .	61
Table 4-5.	Comparison of EOIM solar UV erosion efficiencies with LDEF results. . . . .	62
Table 4-6.	Molecular weight distributions for EOIM-3 solar UV specimens. . . . .	66

### **List of Appendices**

Appendix A	Tables of Materials . . . . .	A-1
Appendix B	Mass Data . . . . .	B-1
Appendix C	ESCA Data . . . . .	C-1



## ABSTRACT

The deleterious effects of hyperthermal atomic oxygen (AO) found in low-Earth-orbit (LEO) environments on critical flight materials has been known since early Shuttle flights. This corrosive effect is of considerable concern because it compromises the performance and longevity of spacecraft/satellite materials deployed for extended periods in LEO.

The NASA Evaluation of Oxygen Interactions with Materials-3 (EOIM-3) experiment served as a testbed for a variety of candidate flight materials for space assets. A total of 57 JPL test specimens were present in six sub-experiments aboard EOIM-3. In addition to a number of passive exposure materials for flight and advanced technology programs, several sub-experiments were included to provide data for understanding the details of atomic oxygen interactions with materials. Data and interpretations are presented for the heated tray, heated strips, solar ultraviolet exposure, and scatterometer sub-experiments, along with a detailed description of the exposure conditions experienced by materials in the various experiments.

Mass spectra of products emerging from identical samples of a  $^{13}\text{C}$ -enriched polyimide polymer (chemically equivalent to Kapton) under atomic oxygen bombardment in space and in the laboratory were collected. Reaction products unambiguously detected in space were  $^{13}\text{CO}$ ,  $\text{NO}$ ,  $^{12}\text{CO}_2$ , and  $^{13}\text{CO}_2$ . These reaction products and two others,  $\text{H}_2\text{O}$  and  $^{12}\text{CO}$ , were detected in the laboratory, along with inelastically scattered atomic and molecular oxygen. Qualitative agreement was seen in the mass spectra taken in space and in the laboratory; the agreement may be improved by reducing the fraction of  $\text{O}_2$  in the laboratory molecular beam. Both laboratory and space data indicate that  $\text{CO}$  and  $\text{CO}_2$  products come preferentially from reaction with the imide component of the polymer chain, raising the possibility that the ether component may degrade in part by the "evaporation" of higher molecular weight fragments. Laboratory time-of-flight distributions showed 1) incomplete energy accommodation of impinging  $\text{O}$  and  $\text{O}_2$  species that do not react with the surface and 2) both hyperthermal and thermal  $\text{CO}$  and  $\text{CO}_2$  products, suggesting two distinct reaction mechanisms with the surface.

## 1.0 Introduction

Future NASA missions will rely on long-lifetime high-performance space assets that will be exposed to various orbital and interplanetary space environments. The recently recovered Long Duration Exposure Facility (LDEF) satellite dramatically illustrates the detrimental effect of long space exposure on thermal control materials, composites, optical materials, and other vulnerable components. To ensure end-of-life performance of future space assets, it is critical to perform material selection and design for each spacecraft system. The NASA Evaluation of Oxygen Interactions with Materials (EOIM-3) experiment was developed to expand the database for materials exposed to the low-Earth-orbit (LEO) atomic oxygen (AO) environment in an accelerated, moderate fluence test.

To determine the temperature dependence of AO degradation processes of erosion and oxidation, active tray experiments were carried out at 333 K (60°C) and 473 K (200°C). To study the synergistic effect of UV with AO, a variable solar ultraviolet exposure experiment was planned for 25, 50, and 75 percent of total combined exposure. Model materials were exposed to AO scattered from a variety of primary target materials. The lack of energetic AO directly impinging on the test material, substantially reduces AO degradation. The Air Force Phillips Laboratory (AFPL) mass spectrometer allows accurate AO reaction rate determination and also permits direct observation of reaction products generated.

Recently, a protocol [1] has been written with the objective of providing "guidelines for materials testing in ground-based atomic oxygen environments for the purpose of predicting the durability of the tested materials in low-Earth-orbit (LEO)." The validity of testing under this protocol, or any other set of criteria, rests on the proven ability of the ground-based test facility to produce results that can be related in a straightforward manner to atomic-oxygen-induced effects on materials in LEO. Both space- and ground-based studies on identical materials are required to evaluate ground-based test methods aimed at predicting materials durability in space. Such a ground-space correlation study, which involved materials exposure on the EOIM-3 flight experiment, has been reported [2].

Proven agreement between laboratory and space experiments also adds value to the results of scientific experiments in the laboratory. It is much easier to perform sophisticated experiments in the laboratory than in space. Laboratory experiments therefore have the potential to reveal more information than space experiments about the interaction mechanisms of hyperthermal oxygen atoms with materials in LEO. The extent to which the laboratory results can lead to inferences about O-atom interactions in LEO depends on the ability of the laboratory experiment to predict effects seen in the actual LEO environment.

The EOIM-3 carousel experiment provided an ideal "calibration point" for powerful molecular beam/surface scattering experiments that were conducted at the Jet Propulsion Laboratory (JPL). This report contains new data, both from EOIM-3 and from our laboratory at JPL, on the interaction of hyperthermal O atoms with an isotopically labeled, Kapton-like polyimide surface. The molecular beam experiment provides the capability to examine the identity of products that emerge from the surface, as well as their directions and velocities. These diagnostic capabilities permit the interaction dynamics of fast O atoms with a surface to be inferred. The EOIM-3 carousel experiment yields information only on the identity of the scattered species; nevertheless, this information provides a common point of reference for assessing the value of the laboratory results. The new laboratory results agree qualitatively with the space observations and point the way to a clearer understanding of O-atom interactions with materials in LEO.

Subsequent sections of this report also provide a detailed description of the exposure conditions experienced by materials in various experimental trays, a description of the materials tested, the pre- and post-flight exposure characterization methods, and the results of the AO exposure experiments.

## **2.0 STS-46 and EOIM-3 Overview**

The STS-46 mission included two primary payloads, the European Retrievable Carrier (EURECA) satellite and the Tethered Satellite System (TSS-1), and two secondary experiments, the Thermal Energy Management Processes experiment (TEMP 2A-3) and EOIM-3. STS-46 also carried four "Get-Away Special" canisters—the Limited Duration Candidate Experiment (LDCE-1,2,3) and the Consortium of Materials Space Processing Complex Autonomous Payload (CONCAP-II & -III).

### **2.1 EOIM Integration**

The investigators integrated test materials into EOIM-3 sub-experiment fixtures in a clean room environment. The sub-experiment fixtures were integrated into the EOIM-3 pallet by Lockheed Engineering and Space Co. personnel under the direction of the NASA/Johnson Space Center (JSC) experiment manager. The installation took place in a Class-100,000 high-bay clean room at the NASA Kennedy Space Center (KSC) Operations and Configurations (O&C) Building. The individual remove-before-flight covers remained in place until all 15 EOIM-3 passive trays were installed. These individual covers were removed prior to the EOIM-3 pallet integration into the orbiter, where the entire EOIM-3 pallet was protected with a large single pallet cover. The EOIM-3 experiment pallet was installed in Shuttle Bay 12, as illustrated in Figure 2-1, and removed during orbiter close-out activities approximately 70 hours before launch. The payload service structure provided a nominal Class-100,000 environment for the orbiter payload prior to closing the payload bay doors 60 hours before launch. A nitrogen purge through the orbiter payload bay continued from 40 hours before launch until just prior to launch.

### **2.2 STS-46 Mission Timeline**

STS-46 was launched on July 31, 1992, aboard the Space Shuttle Atlantis. Deployment of the EURECA satellite, the first major mission milestone, occurred at a Mission Elapsed Time (MET) of 1 Day, 17 hours, and 8 minutes (01/17:08). Deployment occurred at an orbit altitude of approximately 425 km (230 nmi). Prior to EURECA deployment, the orbiter orientation maintained the payload bay in a solar inertial configuration (-ZSI) for approximately 12 hours starting at MET 0/23:07, with -Z pointing out of the payload bay (see Figure 2-1). After EURECA deployment,



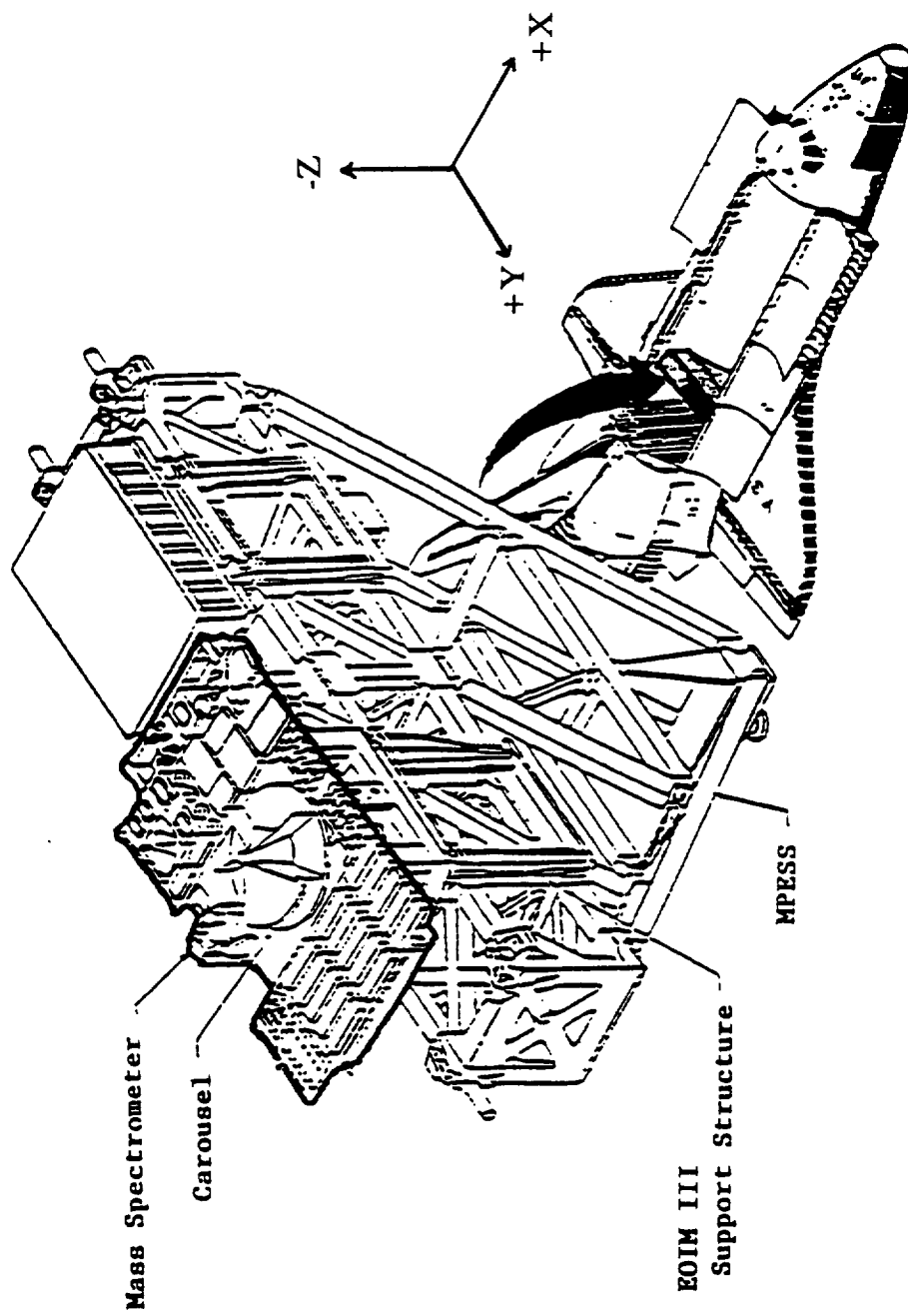


Figure 2-1. Sketch showing EOIM-3 experiment pallet location in Shuttle Bay 12.

STS-46 continued in a station-keeping mode with EURECA, providing a minor period of approximately 4 hours of ram atomic oxygen exposure to EOIM-3. STS-46 then moved into a circular orbit of approximately 300 km (160 nmi) at MET 02/20:28 for TSS-1 operations.

The TSS-1 satellite was to deploy to a distance of approximately 20 km from the Shuttle and conduct an electrodynamic experiment. Due to technical problems, TSS-1 was deployed to only approximately 280 m. Following retrieval and berthing of TSS-1 at MET 05/08:56, the orbiter transferred into a circular orbit of approximately 230 km (123 nmi) at MET 05/19:27.

At MET 05/22:30, the payload bay of Atlantis was oriented into the orbital velocity vector (-ZVV) to begin the EOIM-3 atomic oxygen exposure experiment. Thereafter, the orbiter maintained the ram attitude within  $\pm 5^\circ$  until MET 07/16:45, at which time the payload bay was reoriented out of the velocity direction and prepared for the deorbit burn. The total ram exposure time at 230 km was 42.25 hours.

### 2.3 Atomic Oxygen Environment

The AO fluence for EOIM-3 is estimated to be  $2.2\text{--}2.5 \times 10^{20}$  atoms/cm<sup>2</sup>. Three methods provided estimates of the EOIM-3 atomic oxygen fluence. First, the Mass Spectrometric and Incoherent Scatter (MSIS-86) Thermospheric model, in conjunction with the National Oceanic and Atmospheric Administration (NOAA), reported solar 10.7-cm flux ( $F_{10.7}$ ) and the magnetic indices ( $a_p$ ,  $k_p$ ) were used to estimate the densities for various atmospheric species, including AO. Figure 2-2 provides an orbital history of atomic oxygen density for the EOIM-3 exposure portion of the STS-46 mission. The AO flux was computed by coupling the MSIS-86 density with the orbiter velocity. AO fluence was calculated by integrating the AO flux for the exposure period. Depending on the period in which the solar and magnetic indices were sampled, the estimated AO fluence varied from  $2.0 \times 10^{20}$  atoms/cm<sup>2</sup> to  $2.2 \times 10^{20}$  atoms/cm<sup>2</sup>. The second AO fluence estimate is based on the erosion of Kapton polyimide film. Numerous Kapton samples were located on various passive trays on the EOIM-3 pallet. Erosion was determined by mass loss, scanning electron microscopy (SEM), and profilometry measurements. Based on a reaction efficiency of  $3.0 \times 10^{-24}$  cm<sup>3</sup>/AO atom, the EOIM-3 fluence was calculated to be between  $2.3 \times 10^{20}$  atoms/cm<sup>2</sup> and  $2.5 \times 10^{20}$  atoms/cm<sup>2</sup>. The weight losses varied with sample location and gave rise to the calculated fluence

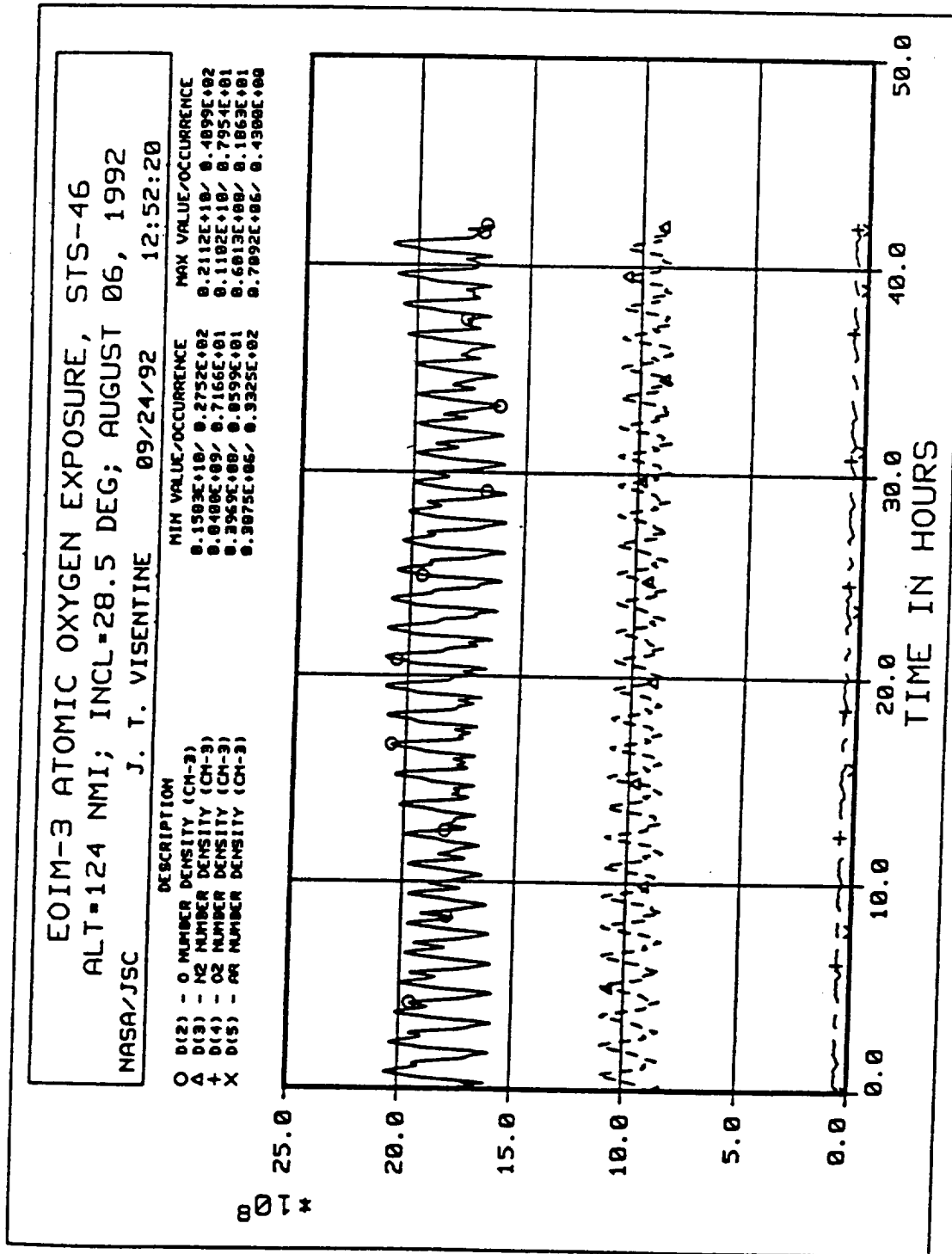


Figure 2-2. Orbital history of atomic oxygen density during EOIM-3.

range. The third AO fluence estimate is based on data from the AFPL mass spectrometer. The on-board spectrometer provided a mission fluence estimate of  $2.2 \pm 0.4 \times 10^{20}$  atoms/cm<sup>2</sup>.

## 2.4 Solar UV Environment

NASA JSC provided the EOIM-3 solar UV exposure estimate. Their estimate is based on integration of the sun angle, orbiter attitude, and ephemeris over the entire mission. The estimate does not account for shadowing from payloads and orbiter structure, but is thought to be accurate within  $\pm 20$  percent. The estimate is 25 equivalent solar hours (ESH) exposure.

## 2.5 Thermal Environment

The EOIM-3 pallet provided 12 temperature sensors as part of the state-of-health and engineering data system. Figure 2-3 shows the on-orbit temperature history for an aluminized Kapton film bonded on a thin aluminum disk to which one of the temperature sensors was mounted. The various phases of the mission are indicated along the base of the plot. During the EURECA operations, the payload bay was held in a solar inertial attitude for approximately 12 hours. The Kapton film reached a temperature in excess of 343 K (70°C) during this period. Later, during the EOIM-3 exposure phase of the mission, the same sensor temperature cycled between 293 K (+20°C) and 318 K (+45°C). Figures 2-4 and 2-5 show the temperature histories of the mounting location for the trays heated to 333 and 473 K, respectively. Figure 2-6 is a temperature history of the composite stress fixture H2 located near the JPL/Neutral Particle Beam scatterometers. The peak temperature during the solar inertial phase reached 328 K (+55°C), and temperatures cycled between 278 K (+5°C) and 293 K (+20°C) during the EOIM-3 exposure period.

## 2.6 Flight Contamination

Surface chemical analyses revealed a small percentage of silicon present on all flight samples. Materials readily eroded by atomic oxygen contained 2–3 atom percent silicon on the surface. The more stable or AO-resistant materials contained 9–12 atom percent silicon on the surface. The stoichiometry indicated that a thin film of SiO<sub>2</sub> had formed on these specimens. For the stable materials, which had received a heavier accumulation of silicon, this film is on the order of 2 nm (20 Å) thick.

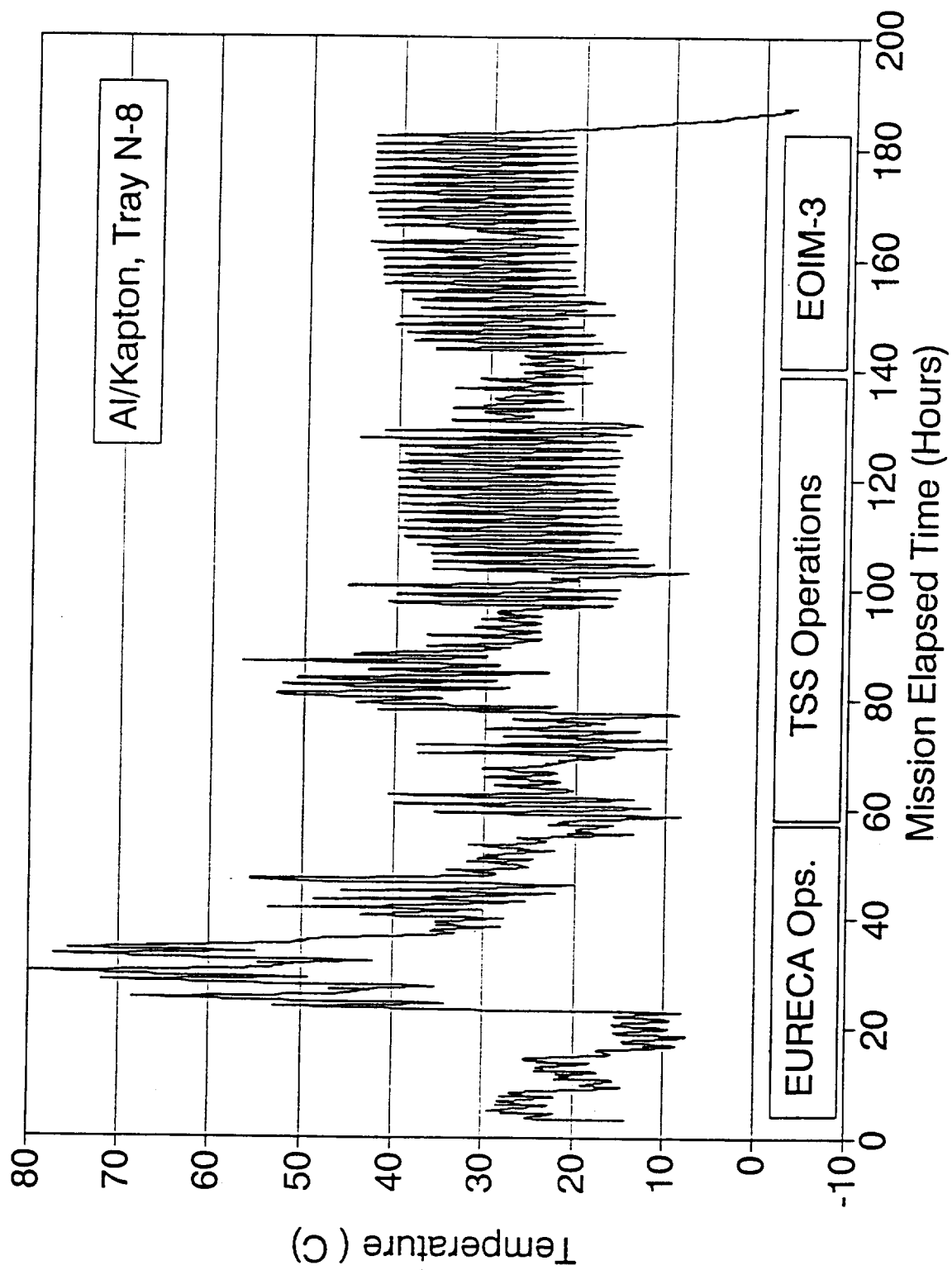


Figure 2-3. Temperature history of passive tray N-8.

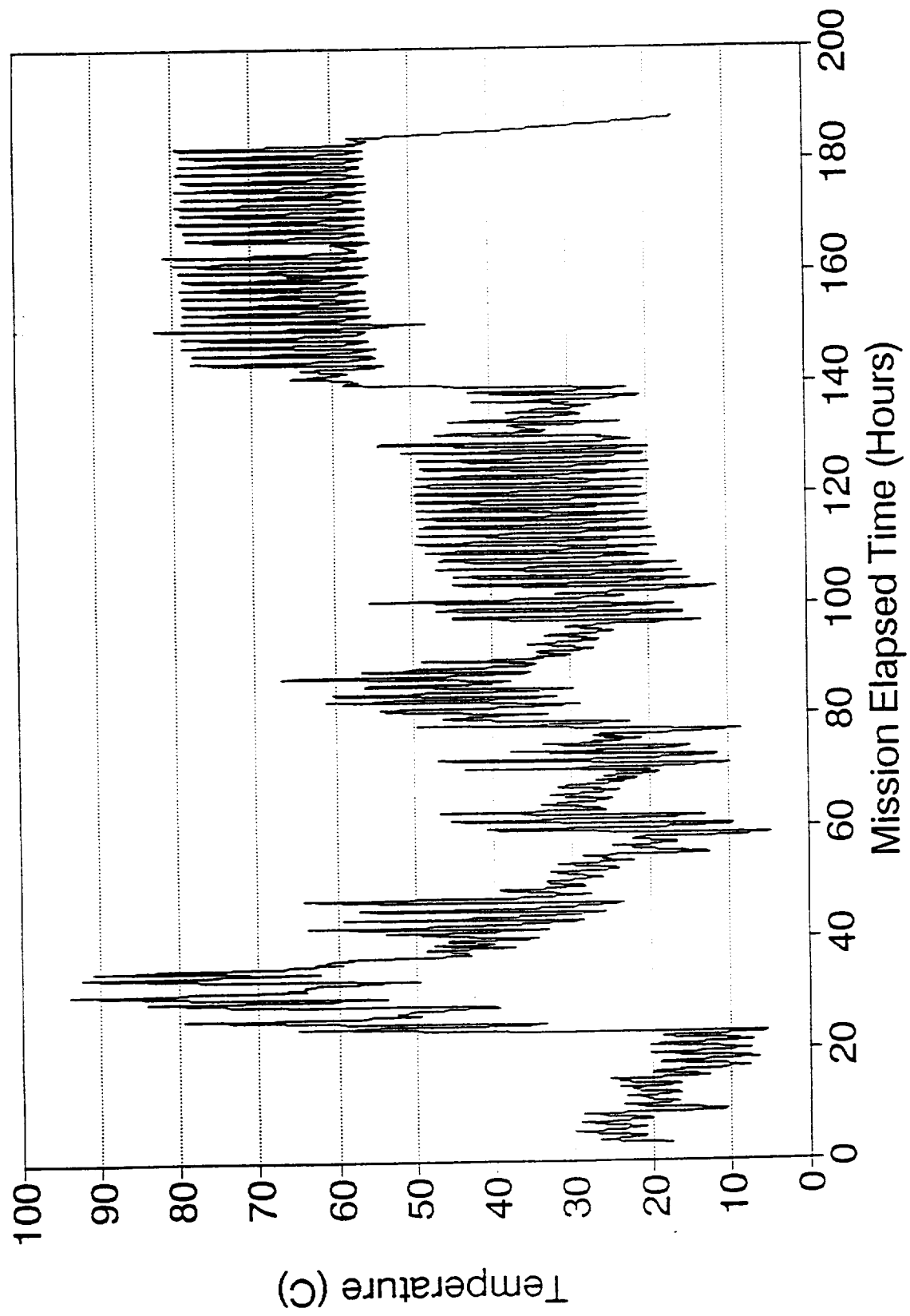


Figure 2-4. Temperature history of 333 K (60°C) tray.

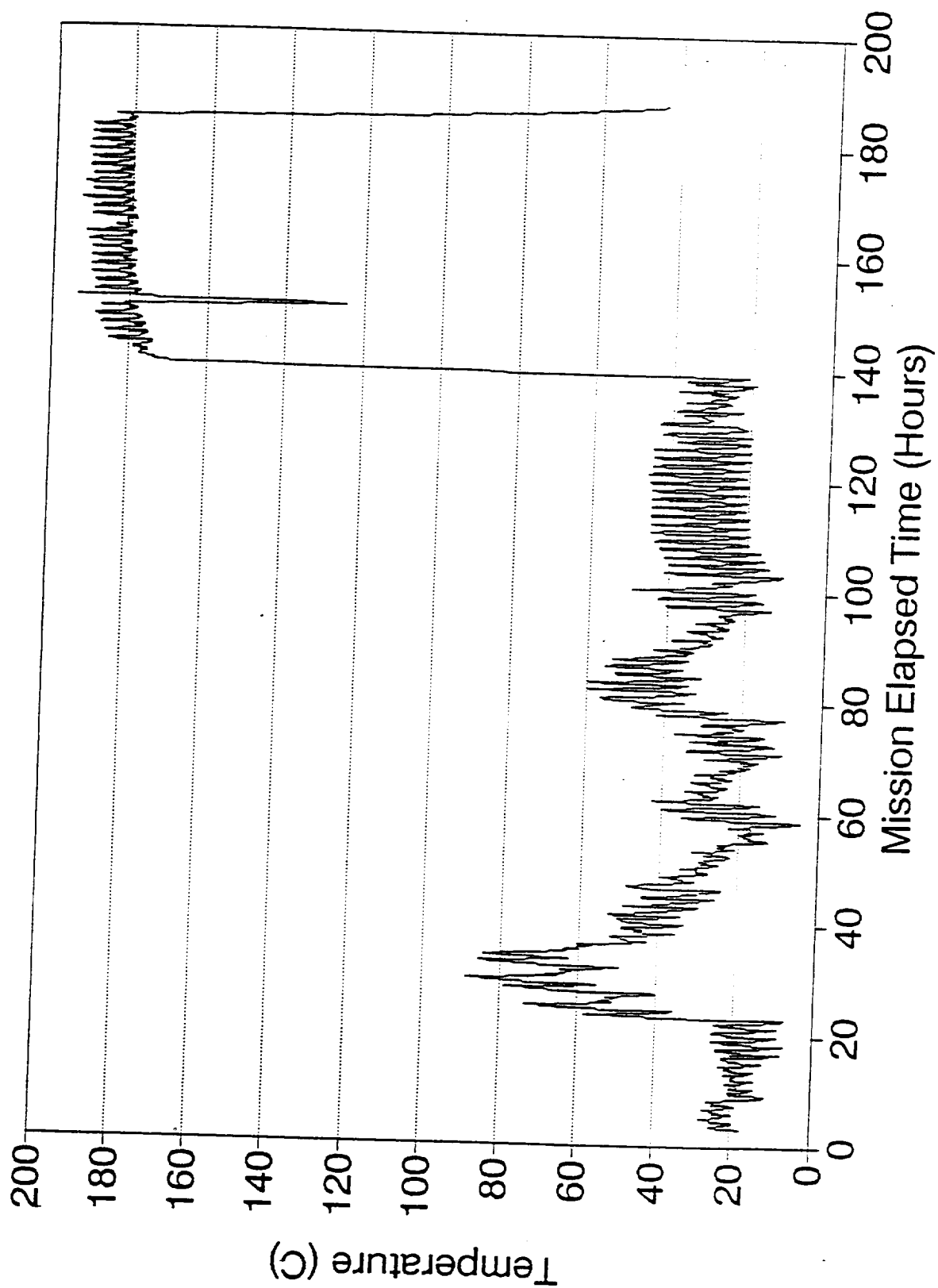


Figure 2-5. Temperature history of 473 K (200°C) tray.

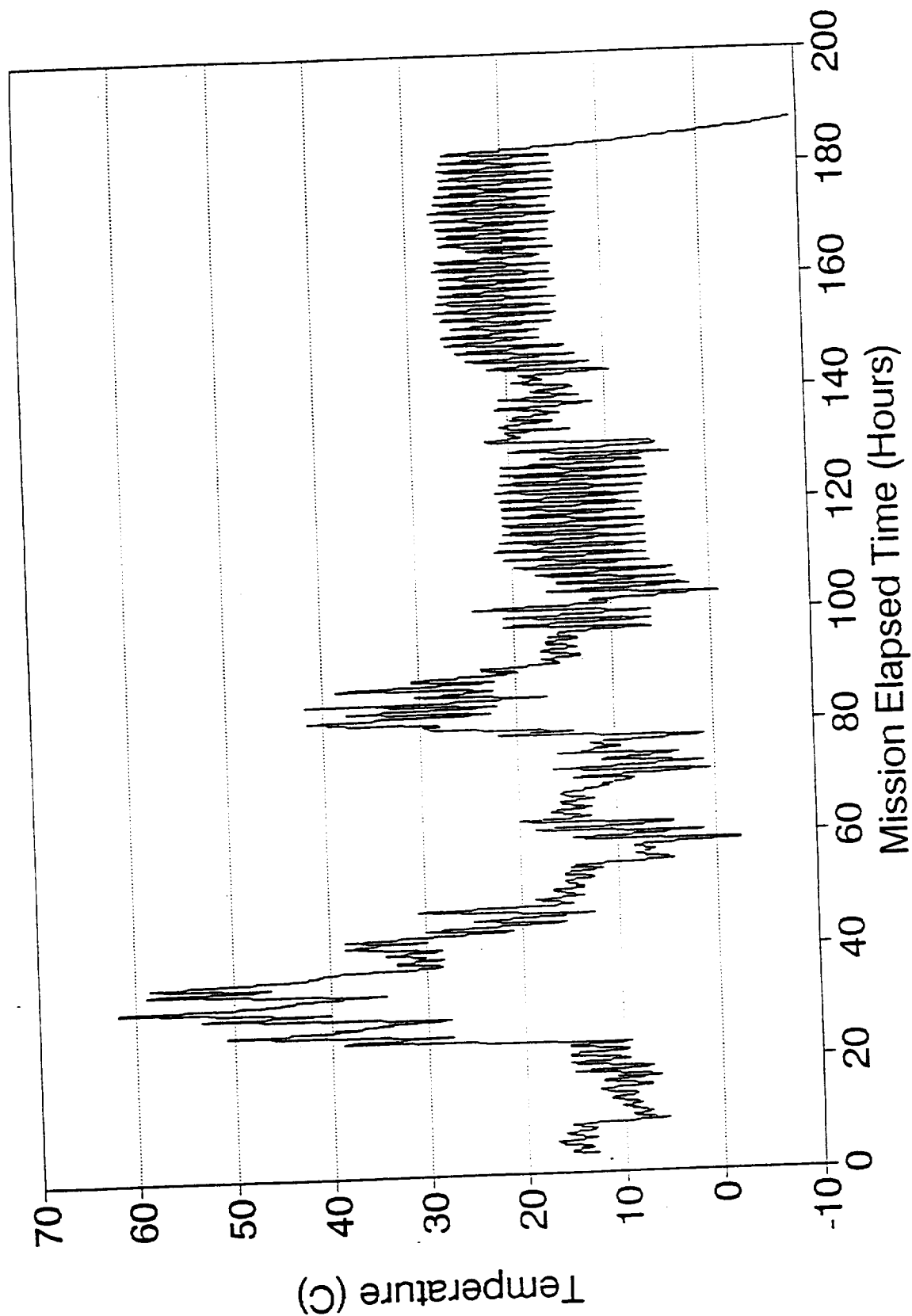


Figure 2-6. Temperature history of composite stress fixture H2 near scatterometers.



The potential sources for silicone contamination have been identified. The forward surfaces of the Orbital Maneuvering System (OMS) pods were just in the field-of-view of the EOIM-3 samples. Since a silicone-based waterproofing agent is applied to the shuttle thermal protection system (TPS) tiles, the tiles are a potential source of silicone contamination. The aft bulkhead is covered with a multilayer insulation blanket with an outer layer of Beta-cloth. Beta-cloth is a woven glass fabric encapsulated in a fluorocarbon resin. In the manufacturing process, the glass fabric is treated with a silicone oil prior to encapsulation to improve the handling characteristics of the material. In the thermal vacuum environment of space, this silicone oil can slowly diffuse from within the fabric, migrate to the surface, and outgas. Yellowing of the Beta-cloth liner is commonly observed and is associated with environmental aging of the silicone film. Silicone oil could outgas and be transported via line-of-sight to sensitive EOIM-3 surfaces.

## **2.7 Post-Flight Inspection**

A team of EOIM-3 coinvestigators and the Mission Manager inspected EOIM-3 in the orbiter payload bay when Atlantis returned to Orbiter Processing Facility Bay 2. The inspection objectives were to assess overall hardware condition, examine hardware and experiments for evidence of contamination, and direct the photographic documentation of EOIM-3. The inspection team members were:

Bruce Banks	NASA Lewis Research Center
David Brinza	NASA Jet Propulsion Laboratory
Rachel Kemenetzky	NASA Marshall Space Flight Center
Jack Triolo	NASA Goddard Space Flight Center
Michael Richardson	NASA Johnson Space Flight Center/LMSC

The team performed two visual inspections of the EOIM-3 hardware and experiments while EOIM-3 was in the bay. The first inspection was performed from the Level 7 platforms approximately 4.5 m above and 6 m outboard (15 and 20 ft) of the payload bay. The second occurred from the Level 13 platforms located adjacent to the payload bay door hinges.

The first inspection provided an overall perspective of the hardware in relationship to the orbiter structures and other payloads in the bay. No obvious regions of contamination were

observed during this inspection. The EOIM-3 hardware itself appeared to be in good condition. The sub-experiment elements all appeared normal.

The second inspection permitted a physically closer evaluation of the experimental hardware and surrounding support structure. The passive trays showed no visibly apparent contamination. The JPL Kapton witness appeared nonspecular and the  $\text{MgF}_2$  witness appeared clean. From this location, the mirror materials and protective coatings appeared visually clean.

The EOIM-3 pallet was removed from Atlantis on August 15, 1992, and transferred to the Operations and Checkout (O&C) Building. EOIM-3 sub-experiment deintegration began ten days later on August 25. Following removal, the sub-experiment hardware was protected by individual hard covers and double-bagged in clean metallized polymer film to avoid contamination during shipment and handling. The test specimens were removed from the sub-experiment hardware in a clean room environment.

### **3.0 EOIM-3 Experiment**

Material samples were integrated into six experimental environments in this EOIM-3 pallet. Their locations are shown in Figure 3-1, which include the heated sample trays (Item A), the scatterometer (Item I), the passive trays (Items N1-15), the variable exposure tray (Item O), the solar UV experiment (Item D), and one of the five carousel compartments. Measurement of the two key parameters of absolute erosion rate and extent of oxidation for the material samples in these experimental environments will provide a comprehensive overview of how they will perform under most deployment conditions. Specifically, the erosion rate and degree of oxidation for ambient, ram-directed AO will come from the passive tray samples, for reflected (scattered) AO from the scatterometer samples, and the temperature dependence of these two processes from the heated tray samples. The specific materials flown and the experimental configurations are listed in Appendix A.

#### **3.1 Sample Handling**

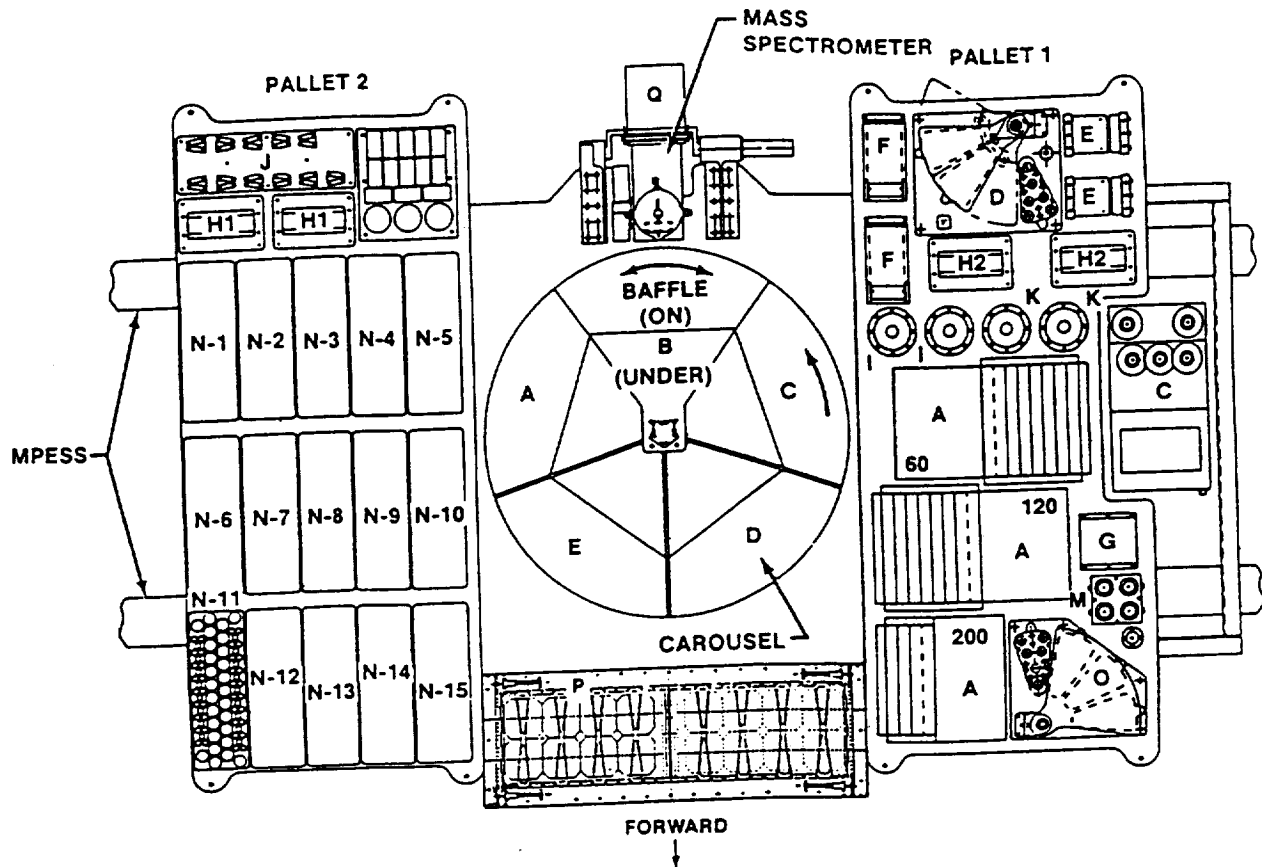
All material samples were handled by personnel wearing vinyl, lint-free Class-100 clean room gloves. Disk samples were maintained in individual Fluoroware containers consisting of polypropylene wafer shippers with polyethylene springs. These containers protected the samples from damage and contamination during shipment and storage. During shipping, the containers were double-bagged in 3M-2110E antistatic reclosable bags.

#### **3.2 Sample Characterization Methods**

This section describes the methods used to characterize the material specimens before and after exposure aboard STS-46.

##### **3.2.1 Photography**

All specimens were photographed at JPL in a Class-100 clean room. For a direct comparison, close-up photographs of each flight-exposed sample adjacent to its control were taken.



**ATOMIC INTERACTION EXPERIMENTS:**

- A - HEATED PLATE (JSC), 3EA
- B - ATOM SCATTERING EXPERIMENT (UAH), 1EA
- C - ENVIRONMENT MONITOR PACKAGE (GSFC), 1EA
- D - SOLAR UV EXPERIMENT (JSC), 1EA
- E - STATIC STRESS FIXTURE (MSFC), 2 EA
- F - UNIFORM STRESS FIXTURE (MSFC), 2 EA
- G - ATOMIC OXYGEN MONITOR (MSFC), 1 EA
- H1 - COMPOSITE STRESS FIXTURE (LaRC), 2EA
- H2 - COMPOSITE STRESS FIXTURE (JSC), 2 EA

- I - SCATTEROMETER (JPL), 2 EA
- J - MECHANICAL STRESS FIXTURE (LaRC), 11 EA
- K - REFLECTOMETER (LaRC), 2 EA
- L - PINHOLE CAMERA (LaRC), 1 EA
- M - SCATEROMETER(AEROSPACE CORP.), 1EA
- N - PASSIVE SAMPLE CARRIERS, 15 EA
- O - VARIABLE EXPOSURE TRAY, 1EA
- P - FREEDOM ARRAY MATERIALS EXPOSURE EXPERIMENT(LaRC), 1 EA
- Q - QUADRUPLER MASS SPECTROMETER, 1 EA

Figure 3-1. The EOIM-3 experiment pallet.

### *3.2.2 Electron Spectroscopy for Chemical Analysis*

The surface chemistry of each control sample was analyzed using Electron Spectroscopy for Chemical Analysis (ESCA), also known as X-ray Photoelectron Spectroscopy (XPS). The analysis ascertained material surface cleanliness and chemical composition.

ESCA spectra were collected with a Surface Science Instruments SSX-501 Spectrometer with monochromatized Al K $\alpha$  X-rays (1486.6 eV). The X-ray source produces spot diameters of 150, 300, 600, and 1000  $\mu\text{m}$ . Both 300- and 600- $\mu\text{m}$  diameter spots were used. The chemical composition of the surface is probed to a depth of 10 nm (100 Å). ESCA can detect all elements except hydrogen. Sample analyses were performed at pressures below 4  $\mu\text{Pa}$  ( $3 \times 10^{-8}$  torr). ESCA spectra were taken of the flight-exposed samples and then compared to their controls.

### *3.2.3 Weight Measurement*

The difference in sample weight before and after exposure provides a way to determine AO effects. Weight loss may indicate erosion; weight increases may also be observed and could indicate water pickup, contamination, or a more complex interaction such as oxidation.

The flight and control samples were weighed before and after exposure. To account for moisture uptake, the materials were conditioned in a 50-percent relative humidity chamber at room temperature for 24 hours per ASTM E-595 procedures prior to each weighing. The chamber used a saturated calcium nitrate solution to maintain constant humidity.

Weight measurements were made on a Mettler AE 163 Balance, which has a 0.01-mg sensitivity. The weighing procedure consisted of removing a sample from the humidity chamber and placing it in the balance immediately. The weight was recorded when the reading stabilized—typically less than one minute. After weighing, the sample was promptly returned to its Fluoroware container.

### 3.2.4 Scanning Electron Microscopy

Atomic oxygen-induced erosion morphologies and features were imaged via Scanning Electron Microscopy (SEM) for many of the EOIM-3 specimens. Nonconductive materials, such as polymers, required a "shadow" of metallization to prevent distortion of the images due to charging of the material. A low-energy magnetron sputtering source was used to coat the nonconductive specimens with approximately 5 nm (50 Å) of a gold/palladium alloy. In order to prevent damage to the very delicate erosion features, SEM imaging was performed at low electron energy (10 kV) and minimum current.

SEM imaging of erosion "mesas" proved very useful in determining the depth of erosion due to atomic oxygen. The mesas, seen in Figure 3-2(a), were formed by a surface contaminant (particle or residue) protecting the underlying erodible material during atomic oxygen exposure. The surrounding unprotected material was removed to a depth characteristic of the material's erosion efficiency, leaving a spire or mesa. SEM images were obtained with known viewing geometries (generally 45° from the surface normal) so the height of the mesas could be readily determined, as indicated in Figure 3-2(b). The principal uncertainty in the mesa height measurement arises from specifying the "shag-carpet" base of the mesas, clearly shown in Figure 3-2(c).

### 3.2.5 High-Performance Liquid Chromatography

Molecular weight distributions were obtained for soluble polymeric test materials via size exclusion High Pressure Liquid Chromatography (HPLC). Chromatographs were obtained on a Waters Associates Model 6000A chromatograph. The Ultrastyrigel columns were calibrated via polystyrene molecular weight standards in the range of 15,000- to 1,860,000-gram molecular weight. Samples were dissolved in tetrahydrofuran (THF) or methylene chloride to provide a 1000 ppm polymer concentration. Detection was performed by a Waters Model 410 Differential Refractometer and a Model 490E Programmable Multi-wavelength Detector operating at 254 nm.

### 3.2.6 Spectral Reflectance

Reflectance spectra were obtained for the Spectrolon materials using a Cary-5E Spectrophotometer with a reflectance attachment and Spectrolon-coated integrating sphere.

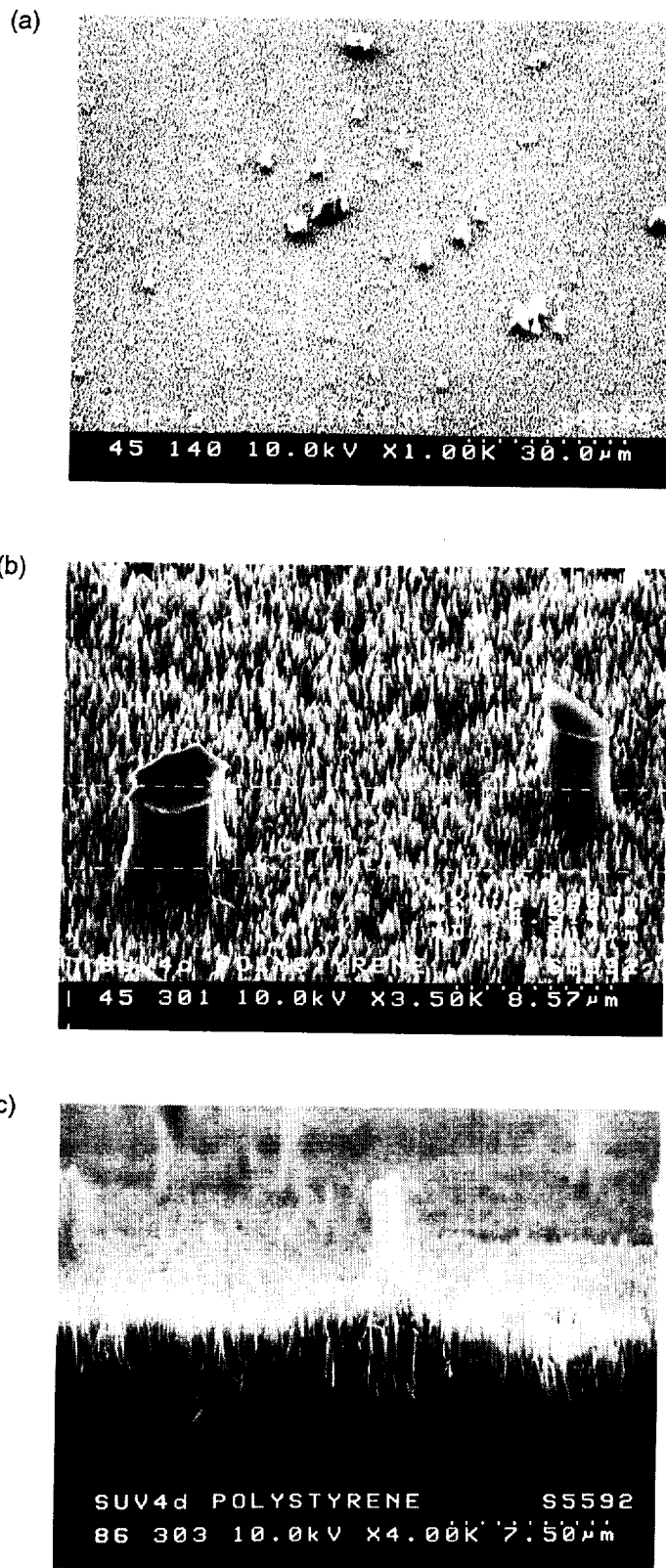


Figure 3-2. SEM images of mesas used to determine erosion depths [see text for descriptions of (a), (b), (c)].

### 3.3 Passive Tray Experiment

To obtain accurate AO erosion rates of the coated candidate materials, 14 passive tray specimens consisting of 2.54-cm (1")-diameter disks of various coatings and materials were prepared for flight exposure. They were integrated into two passive specimen trays (see Appendix A, Table 1) from Johnson Space Center (JSC) and Marshall Space Flight Center (MSFC).

The passive tray flight-exposed samples were photographed along with the control specimens in order to provide a direct visual assessment of gross atomic oxygen erosion effects. Some of these photographs are included in the next section of this report. Mass measurements are included in Appendix B. Surface chemical analyses (ESCA) were performed, with data reported in Appendix C, to assist in identifying chemical changes to material surfaces as a result of atomic oxygen attack, contamination, etc.

#### 3.3.1 Fluorinated Polystyrene Materials

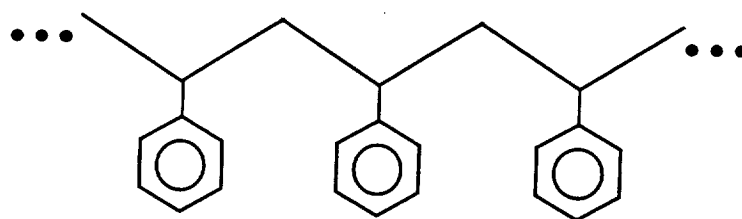
The objective is to determine the effect of selective fluorination of polystyrene on the susceptibility to attack by atomic oxygen. Three variants of polystyrene were exposed to atomic oxygen: unsubstituted molecular weight standard polystyrene, backbone-fluorinated polystyrene, and ring-fluorinated (see Table 3-1 and Figure 3-3). Completely fluorinated polystyrene is highly desirable, but preparation methods for perfluoro-polystyrene are unknown.

The fluorinated polystyrenes were synthesized via emulsion free-radical polymerization of purified monomers. The films were characterized via infrared spectroscopy and high-performance liquid chromatography. The molecular weight distributions for the polystyrene series were determined via size exclusion HPLC and are listed below.

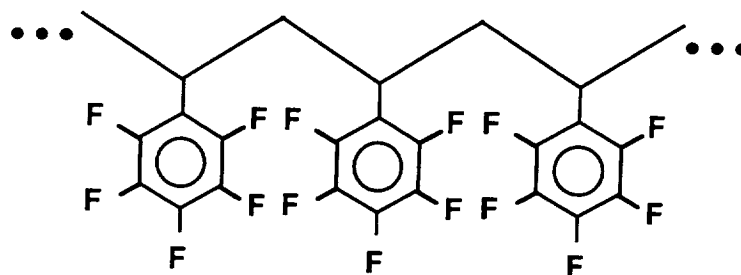
Table 3-1. Molecular weight distributions of polystyrenes

Polymer	$M_w$	$M_n$	$M_w/M_n$
Polystyrene	453,000	174,000	2.6
Trifluoro-Polystyrene (Backbone-fluorinated)	280,000	103,000	2.72
Pentafluoro-Polystyrene (Ring-fluorinated)	431,000	278,000	1.55

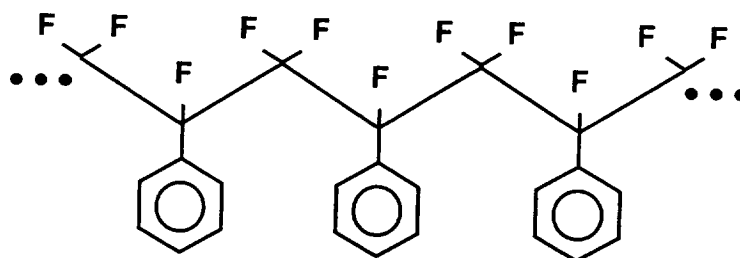




**Polystyrene (1.04 g/cm<sup>3</sup>)**



**Ring-Fluorinated Polystyrene (~1.8 g/cm<sup>3</sup>)**



**Backbone-Fluorinated Polystyrene (~1.4 g/cm<sup>3</sup>)**

**Figure 3-3. Polystyrene and the fluorinated analogues studied on EOIM-3.**

### **3.3.2 Spectrolon**

Spectrolon (TM) specimens of varying solar reflectance were exposed in order to assess the stability of "pure" and carbon-loaded pressed polytetrafluoroethylene (PTFE) reflectance standards. Spectrolon is a candidate calibration target material for space-borne optical systems such as the Multiwavelength Imaging Spectral Radiometer (MISR). The Spectrolon specimens were provided by Labsphere, Inc.

### **3.3.3 White Paints**

Two white paints were evaluated by JPL on the EOIM-3 passive tray. HINCOR, an electrically-conductive zinc ortho-titanate (ZOT) silicate binder white paint developed for the Cassini spacecraft, was characterized for changes in electrical conductivity as well as solar absorptance and hemispherical emittance. An experimental paint containing ZOT pigment and a peroxide-cured polyphosphazene binder were also evaluated on EOIM-3.

## **3.4 Heated Tray and Heated Strip Experiments**

Eighteen material samples were integrated into heated trays and strips to study the temperature dependence of AO erosion at 333 K (60°C) and 473 K (200°C). The heated tray samples were 2.54-cm-diameter circular disks, while the heated copper strips were 2.54 x 22.86 cm (1" x 9") for the 333 K strip, and 2.54 x 25.4 cm (1" x 10") for the 473 K strip. In Appendix A, Tables 2(a) and (b) list the candidate samples located in their respective 333 and 473 K heated trays, while Table 3 lists the materials located in the heated strips.

### **3.4.1 Carbon/Carbon Materials**

Three candidate materials for carbon/carbon composite structures—designated SP18, SP16, and TS15—were integrated into ambient and heated trays. The 2.54-cm disk specimens were cut from panels produced for developmental testing of candidate heat shields for the Solar Probe mission. The atomic oxygen erosion rate for carbon is known to exhibit a significant dependence upon temperature. Quantification of the extent of erosion and changes in thermo-optical properties for these carbon/carbon specimens will help evaluate temperature-dependent effects of atomic oxygen exposure.

A carbon-carbon material designed for high strength, SP18 is composed of T-50, a 3-K fiber woven in a 5 harness weave with an initial phenolic matrix. The material received two graphitization treatments at 2773 K (2500°C) and two 1273 K (1000°C) CVD carbon redensification processing steps. The material final density is approximately 1.6 gm/cm<sup>3</sup>.

Another carbon-carbon material designed for high strength, SP16 is also composed of T-50. The material received two graphitization treatments at 2773 K (2500°C) and two A-240 pitch redensification processing steps, followed by an 1123 K (850°C) carbonization. The material final density is approximately 1.5 gm/cm<sup>3</sup>.

A carbon-carbon material designed for low thermal expansion, TS15 is also composed of T-50. The material was configured quasi-isotropically. The composite received two 1273 K CVD carbon redensification steps, with no graphitization. The material final density is approximately 1.4 gm/cm<sup>3</sup>.

#### *3.4.2 Advanced Photovoltaic Solar Array (APSA) Substrates*

TRW (Space Park) provided a selection of candidate substrate materials for the Advanced Photovoltaic Solar Array (APSA). The test materials included Kapton-HN, SiO<sub>x</sub> (150 nm/1500 Å) on Kapton, 150-nm Indium Tin Oxide (ITO) on Kapton-HN, 150-nm Germanium on Kapton-HN, and Carbon-loaded Kapton films. The effectiveness of the thin film coatings in preventing erosion of Kapton was evaluated at high temperatures (333 and 473 K). The susceptibility of the coated films to cracking, peeling, and undercutting in the thermal vacuum environment in the presence of atomic oxygen was also evaluated.

#### *3.4.3 Polycyanate and Modified-Polycyanate Resins*

Two formulations of polycyanate resins were supplied by ICI to evaluate atomic oxygen stability of materials intended for application as matrices for graphite fiber-reinforced polymeric composites. One of the specimens (MCY) was siloxane-modified to provide resistance against attack by atomic oxygen.

### 3.5 Scatterometer

JPL designed and fabricated atomic oxygen scatterometers (see Figure 3-4), which prevent direct AO interaction with the material samples, but permit scattered AO to impinge them. Various scattering surfaces were applied to the scatterometer chambers. One scatterometer included a polished aluminum surface that reflects most of the entering AO back towards the samples, and a silver surface that reacts with much of the entering AO, thereby greatly attenuating the amount that is scattered back. The aluminum surface provides a determination of the magnitude of degradation due to scattered AO, while the silver surface represents a possible approach to mitigating it. The other scatterometer included scattering targets of carbon, fused silica, polyethylene, and aluminum. Table 4 in Appendix A summarizes the scattering surfaces and reactive target materials flown in the scatterometer.

### 3.6 Solar UV Experiment

The Solar UV experiment permitted an assessment of the synergistic effect of solar exposure and atomic oxygen upon model materials. An occulting baffle, controlled by a photodiode-triggered mechanism, alternately exposed materials to day or night conditions. Four polymeric materials were selected for the solar UV experiment: Udel 1700 polysulfone, amorphous Teflon AF 1600, a molecular-weight standard polymethylmethacrylate (PMMA:  $M_w = 89,000$  and  $M_n = 80,800$ ), and a polystyrene molecular-weight standard ( $M_w = 226,600$  and  $M_n = 217,700$ ). Triplicates of each test material were provided: one for day exposure only, another for night exposure, and one for full (day and night) exposure. Mass loss, ESCA, SEM, and HPLC characterization were performed on three of these materials: the polysulfone, PMMA, and polystyrene specimens.

### 3.7 Variable Exposure Experiment

Boron nitride and HOPG were selected for the variable-exposure experiment that used a baffle system to control the percentage of exposure during the mission. Unfortunately, the baffle moved to the fully open position early in the mission and nullified this experiment. The four duplicate samples of each material received full mission exposure.

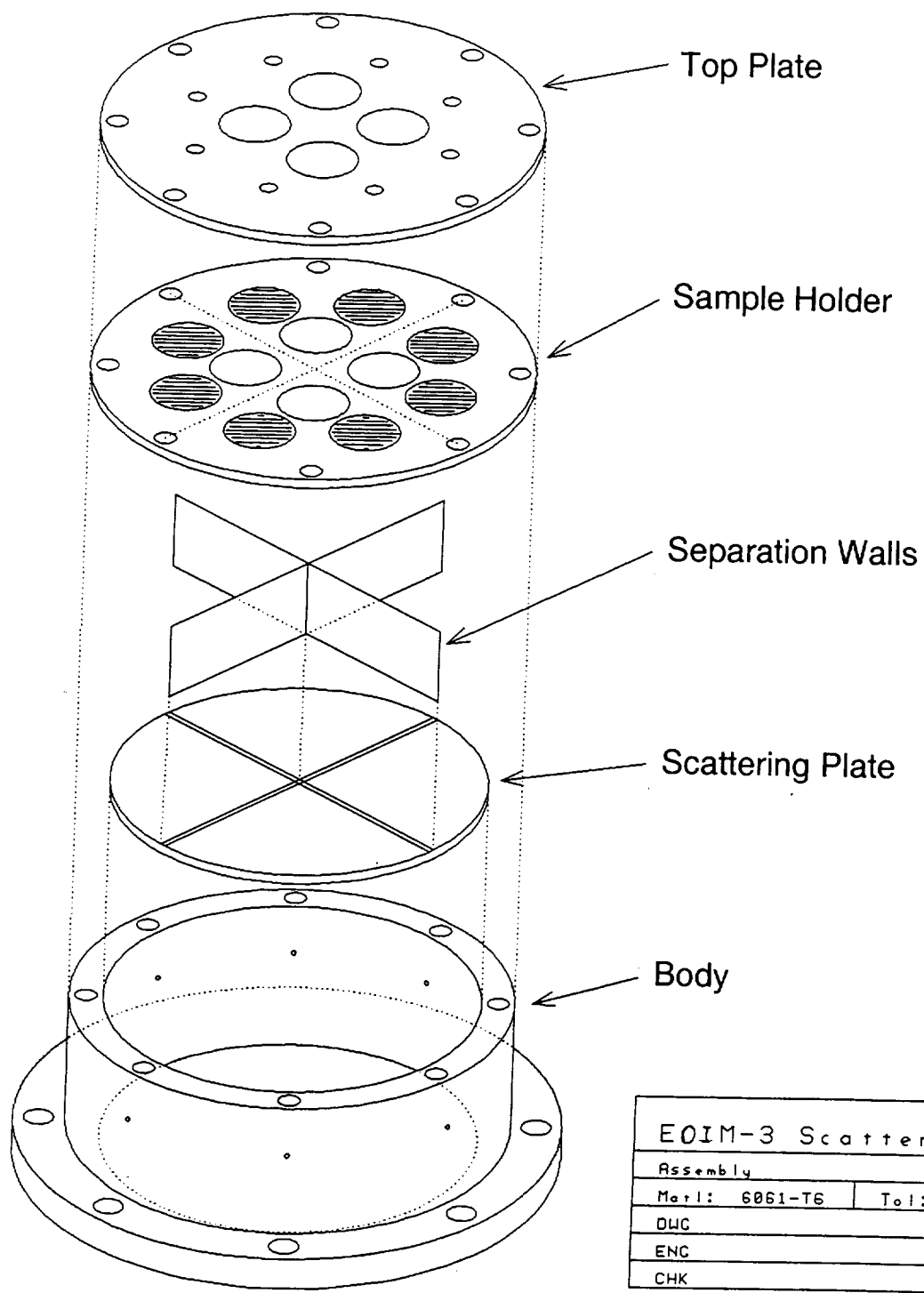


Figure 3-4. EOIM-3 scatterometer design.

### 3.8 Mass Spectrometer and Carousel

A key active experiment on EOIM-3 was the reaction product measurement experiment. Five different materials were mounted on a carousel, such that the surface normal of each material was  $45^\circ$  with respect to the direction of O-atom attack during exposure to atomic oxygen. The carousel could be rotated to place an individual material in view of a mass spectrometer detector, whose nominal viewing axis was  $90^\circ$  to the direction of O-atom impingement. One goal of the carousel experiment was to study the mass spectra of reactive products emerging from the surfaces and use the identity of the volatile products to help infer the reaction mechanisms of fast O atoms in space with the various surfaces. A cover was rotated over the viewed material part of the time to allow for the observation of the differences between the effect of direct O-atom attack and that of scattered O atoms.

JPL supplied one of the carousel materials, a  $^{13}\text{C}$ -enriched polyimide polymer that is chemically equivalent to Kapton HN, which is manufactured by E. I. DuPont de Nemours and Co., Inc. Enrichment with  $^{13}\text{C}$  permits the observation of carbon monoxide (CO) reactive product, which would otherwise be obscured by the high background at a mass-to-charge ratio ( $m/z$ ) of 28 due to molecular nitrogen in the residual atmosphere in LEO. In addition, detection of  $^{13}\text{CO}$  and  $^{13}\text{CO}_2$  proves unambiguously that products of the reaction of the impinging O atoms with the  $^{13}\text{C}$ -enriched polyimide are being observed.

Because the  $^{13}\text{C}$ -enriched polyimide is chemically equivalent to Kapton, we will henceforth refer to it as  $^{13}\text{C}$ -enriched Kapton. Figure 3-5 illustrates the key steps in the synthesis of  $^{13}\text{C}$ -enriched Kapton. All the carbons in one precursor, the ether, were carbon-13. Thus, the resulting polyimide film had a biphenyl ether block in its repeat unit containing 12 carbon atoms that were isotopically labeled as  $^{13}\text{C}$  and an imide block containing 10 unlabeled carbon atoms.

### 3.9 Ground-Based Scattering Measurements

A study of the reaction of hyperthermal O atoms with a Kapton surface in the laboratory has been performed using a crossed molecular beams apparatus [3,4]. This apparatus (see Fig. 3-6) allows beam/surface scattering experiments similar to the EOIM-3 carousel experiment, but it is much more powerful because it permits determination of the velocities and directions of scattered

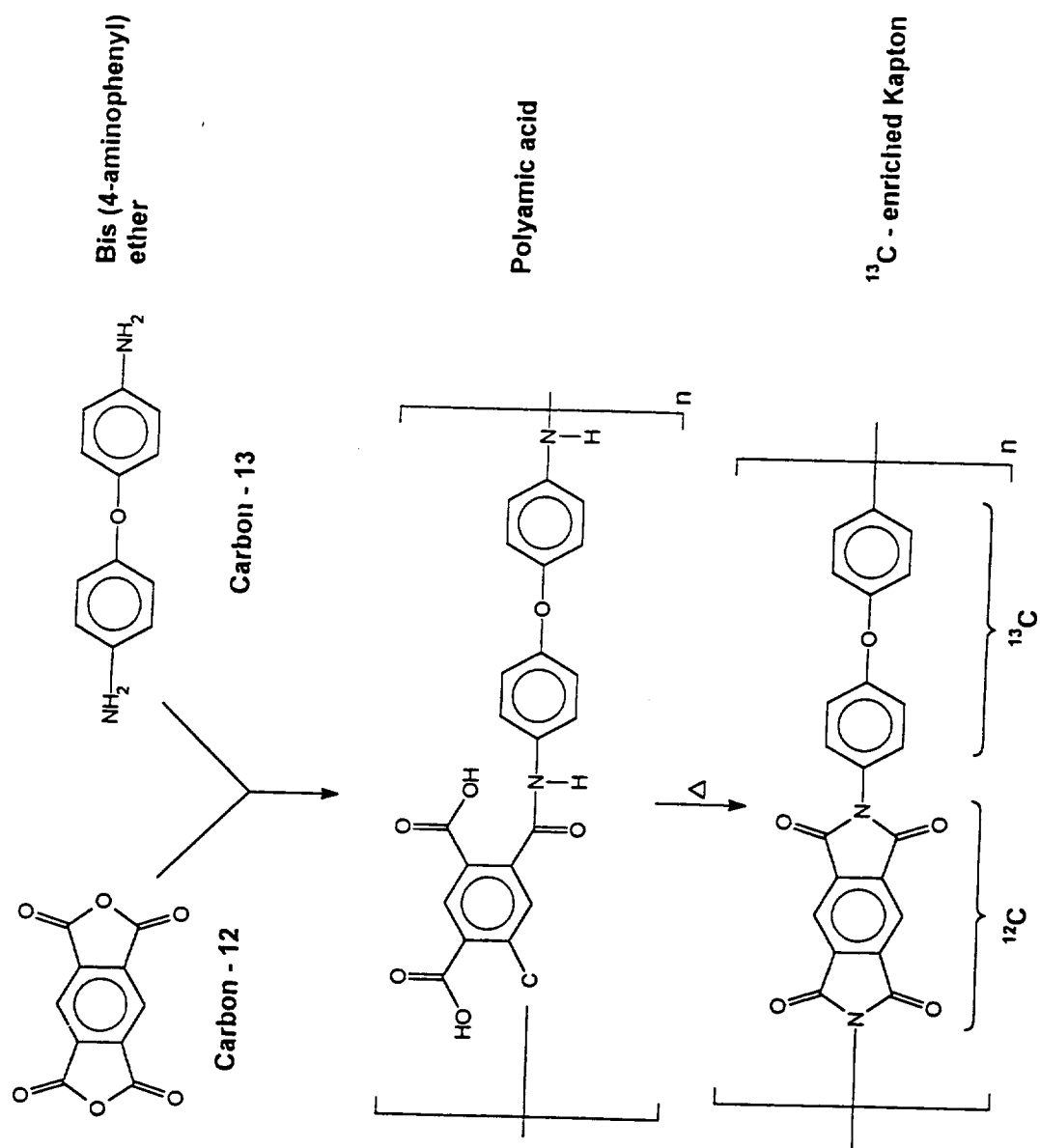


Figure 3-5. Key steps in the synthesis of  $^{13}\text{C}$ -enriched "Kapton."

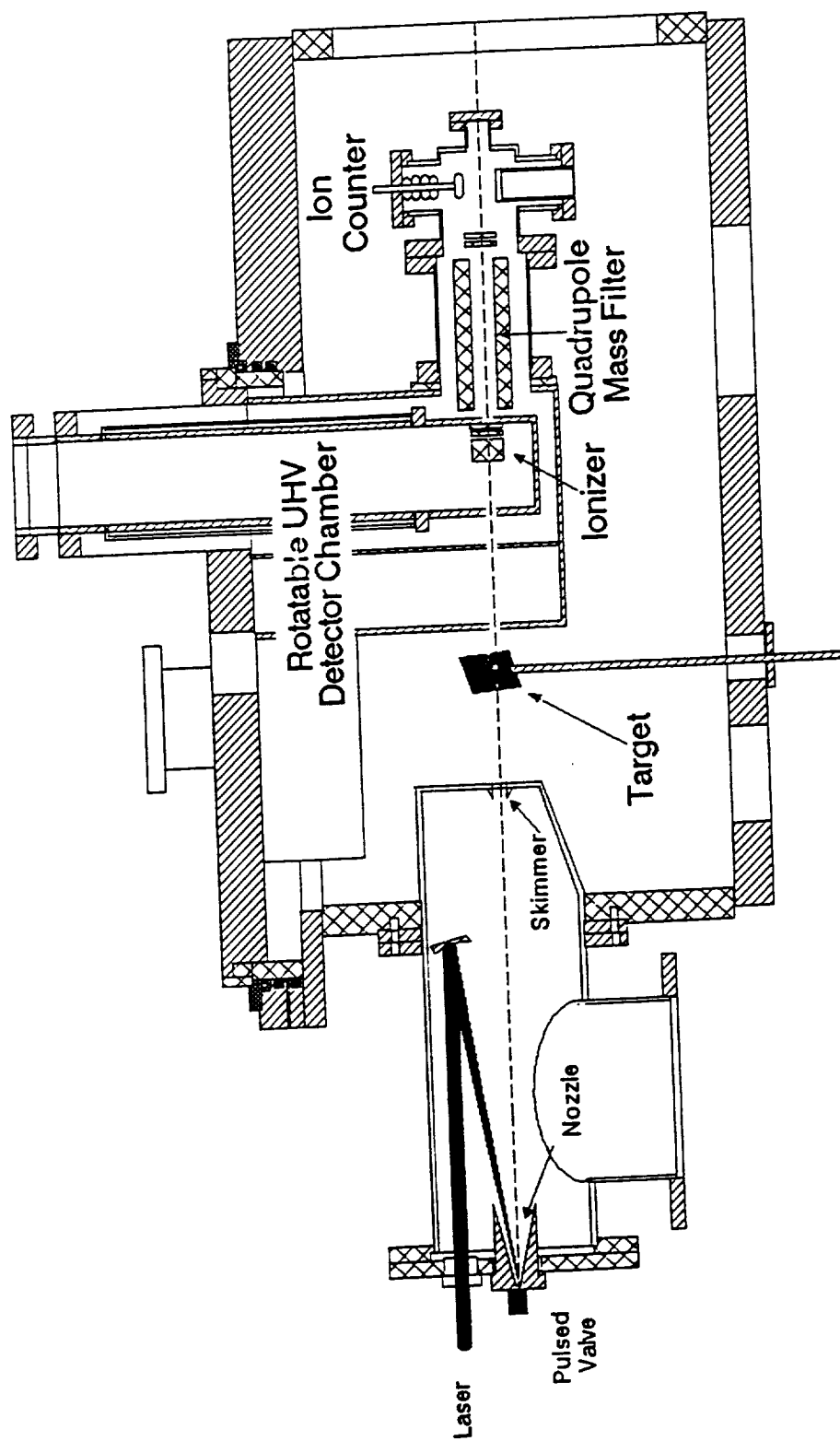


Figure 3-6. Schematic diagram of molecular beam apparatus.



products that emerge from a surface. The atomic oxygen beam source is basically a copy of the source designed by Physical Sciences, Inc. (PSI) [5], where CO<sub>2</sub> laser detonation of oxygen gas is used to produce a pulsed beam of fast O atoms with translational energies near 5 eV. Our source uses a home-built piezoelectric pulsed molecular beam valve [6] to inject O<sub>2</sub> gas into the conical nozzle and a 5 J/pulse Alltec CO<sub>2</sub> laser to induce breakdown in the gas. The pulse repetition rate of the source was 1.8 Hz. For the scattering experiments described herein, the central portion of the hyperthermal beam was selected with a 3-mm-diam. aperture (or "skimmer") placed 80 cm from the apex of the conical nozzle and allowed to impinge on a target 92 cm from the apex of the nozzle, which was mounted on the end of a manipulator. Based on Kapton erosion measurements, we estimate the atomic oxygen flux at the target to be on the order of 10<sup>14</sup> atoms/cm<sup>2</sup>/pulse. A quadrupole mass spectrometer with a triple differentially pumped ionizer can be rotated about the interaction zone on the surface and can detect inelastically and reactively scattered products that emerge from the surface in a particular direction. The distance from the surface to the ionizer of the detector is 34.5 cm, and the detector viewing angle is 3°. The mass spectrometer has been carefully designed with apertures that permit any products entering the ionizer to pass through into another differentially pumped region. The probability of species, which pass through without being ionized, scattering back into the ionizer is therefore extremely low. Thus, measurements of the time-of-flight (TOF) distributions of species entering the detector give a true reflection of their kinetic energies. The target can be lowered out of the beam and the detector can be positioned directly along the beam axis in order to characterize the O-atom beam. When viewing the beam directly, a very small 0.12-mm-diameter aperture is used on the front of the detector to prevent gas buildup in the ionization region.

Two samples of Kapton film, one <sup>13</sup>C-enriched and the other DuPont Kapton HN, were mounted on the end of the manipulator such that either sample could be placed in the beam path without breaking vacuum. The temperature of the sample mount was maintained at 340 K. Although the pressure in the source chamber rose to  $\sim 5 \times 10^{-4}$  torr during the pulse, the pressure in the main scattering chamber remained  $\leq 2 \times 10^{-7}$  torr. The source chamber was evacuated with a 25.4 cm (10") Varian VHS-10 oil diffusion pump, which had a water baffle that was cooled with a refrigerated liquid to 250 K. The main scattering chamber was evacuated with two 25.4 cm (10") CTI-10 cryopumps and a liquid nitrogen cryopanel that covered the bottom of the chamber. Even

with cryopumping of the main chamber and scrupulous cleaning of the samples with ultraclean ethanol prior to mounting in the chamber, a contamination layer accumulated on the samples. Although some contamination was probably being deposited constantly during exposure and thus erosion of the surface, a steady-state condition could be reached where we were certain that we were observing products of a reaction with the actual sample material and not a contamination layer on it. As will be seen below, the use of a  $^{13}\text{C}$ -labeled sample proved that a reaction was occurring with the material. Two different means were used to rid the sample of contamination and reach steady state, as determined by observation of reactive TOF signals at CO and  $\text{CO}_2$  product masses. One method was simply to expose the target to oxygen atoms for a long time— $> 10,000$  pulses. To reach steady state faster, we exposed the surface to a beam of 20 keV electrons during O-atom exposure. The electron gun was oriented such that the electron beam was roughly normal to the target surface when the O-atom beam incident angle was  $45^\circ$ . We found that about 5 minutes of electron exposure at fluxes between 1 and  $10 \mu\text{A}/\text{cm}^2$  cleaned the surface sufficiently that subsequent reactive signals were identical to those seen after more than 10,000 pulses of the atomic oxygen beam alone. Because both methods led to identical reactive signals, it appeared that the short electron exposure did not alter the chemical reactions occurring at the surface. All the laboratory data presented in this report were collected after "cleaning" the surface with the electron beam.

Figure 3-7 shows TOF spectra collected with the mass spectrometer directly viewing the beam. Time zero is when the pulsed valve is triggered to open. At this time, oxygen gas begins to enter the conical nozzle. The spike about  $250 \mu\text{s}$  later corresponds to the firing of the  $\text{CO}_2$  laser. This can be considered the actual time zero for the formation of the hyperthermal beam pulse. The spike comes from photoelectrons produced in the detector by ultraviolet light emanating from the laser-induced plasma. The pulse of hyperthermal species arrives at the detector around  $200 \mu\text{s}$  after the laser fires. Thermal  $\text{O}_2$ , which is not processed by the laser, takes more than 2 ms to travel 126.5 cm to the ionizer. These and all TOF distributions presented here include the ion flight time, which is the time required for an ion to travel from the ionizer to the Daly-type ion counter. The ion flight time for a singly-charged ion of mass  $m$  has been found experimentally, and it can be expressed in  $\mu\text{s}$  by the formula  $\alpha(m)^{1/2}$  where the parameter  $\alpha$  is a function of ion energy and other mass spectrometer parameters and is equal to 2.24.

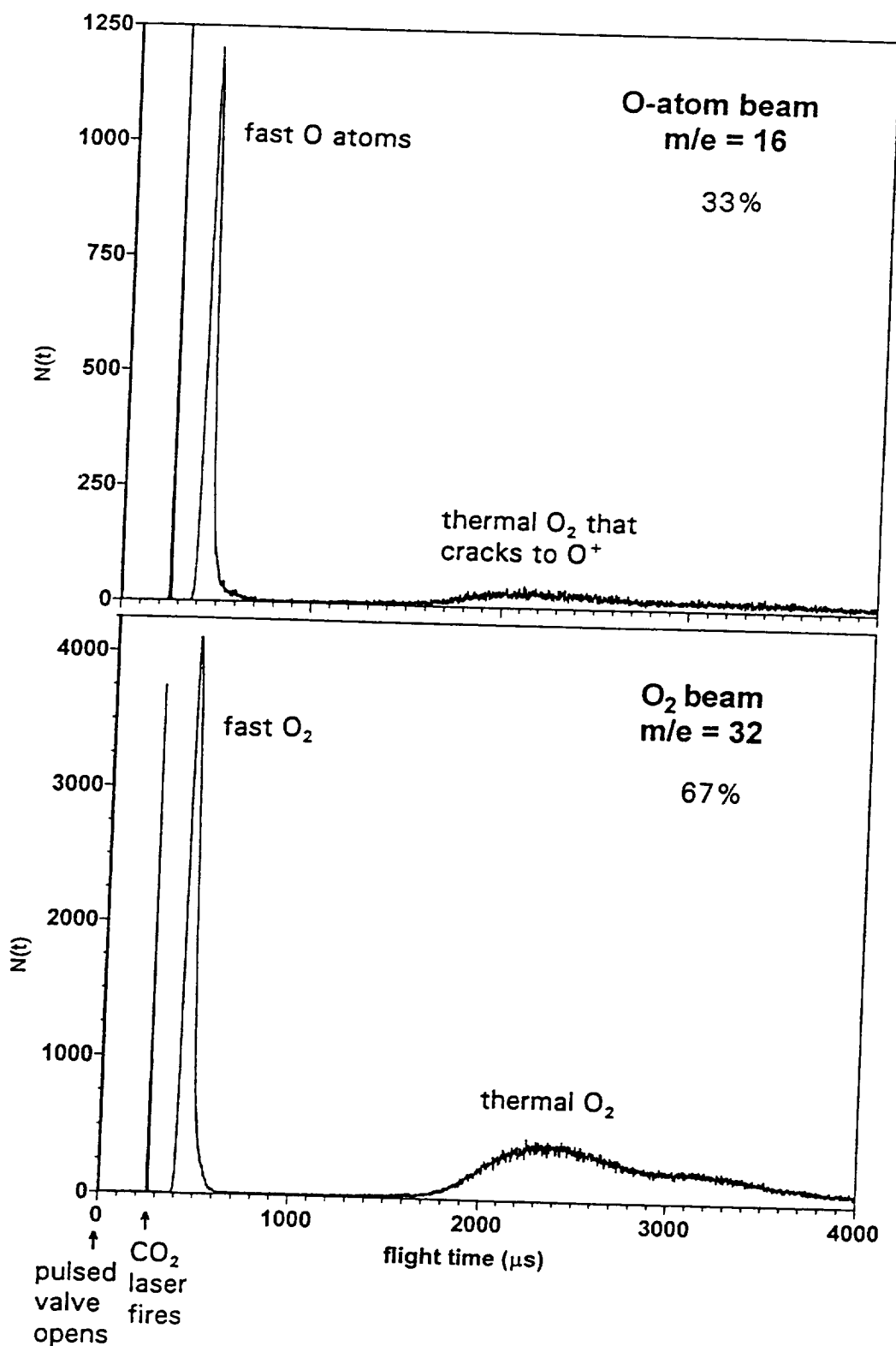


Figure 3-7. Time-of-flight distributions of the molecular beam collected at two masses.

It can be seen from Fig. 3-7 that the fast species in the beam consist of both atomic and molecular oxygen. In fact, for the set of experiments discussed in this report, the O<sub>2</sub> content was roughly twice the O-atom content. The relative O-atom content in the hyperthermal beam pulse is very sensitive to the actual operating conditions of the source. We have observed O-atom fractions from 25 to 70 percent in beams produced in our laboratory. The ion content in a similar beam has been measured at PSI to be about 1 percent, which should be considered an upper limit for our beam. With the ionizer off, there is a tiny signal at  $m/z = 16$  (or 32) whose integral is more than three orders of magnitude lower than the signal with the ionizer on. Given that the detection efficiency should be approximately four orders of magnitude higher for ions, the ion fraction in the beam is probably much less than 1 percent.

Because we measure the arrival time and mass of species that travel a known distance from the source to the ionizer, we can derive the energy distribution of the species in the beam pulse (assuming that the width in the measured TOF distributions is determined by particles traveling at different velocities with a single point of origin in the nozzle cone). We need only take into account the fact that the mass spectrometer is a number density detector while the translational energy distribution is proportional to flux. We thus use the relationship  $P(E) \propto t^2 N(t)$ . Figure 3-8 shows the translational energy distribution of the O-atoms in the beam and the fit this distribution gives to the beam TOF distribution. The average energy of this beam was 4.7 eV, and its width (FWHM) was 2.5 eV. Figure 3-9 shows the analogous energy distribution and fit for the O<sub>2</sub> molecules in the beam. The O<sub>2</sub> component had a much higher average energy (8.7 eV) and energy spread (5.5 eV) than the O-atom component.

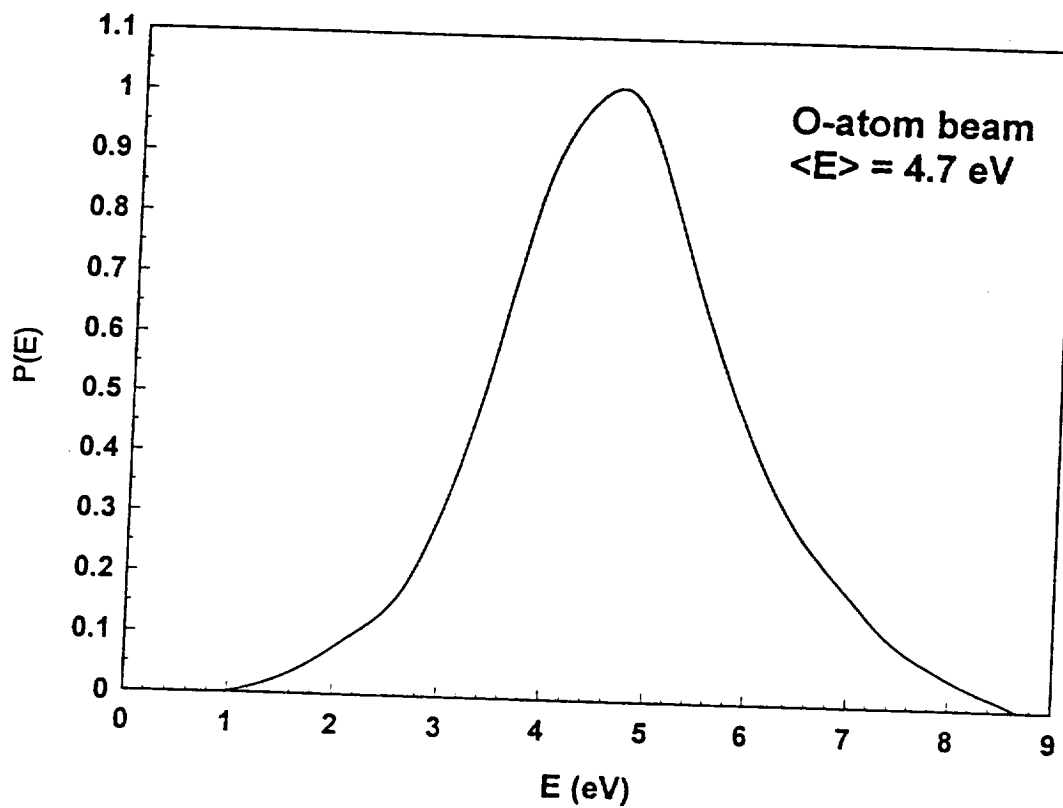
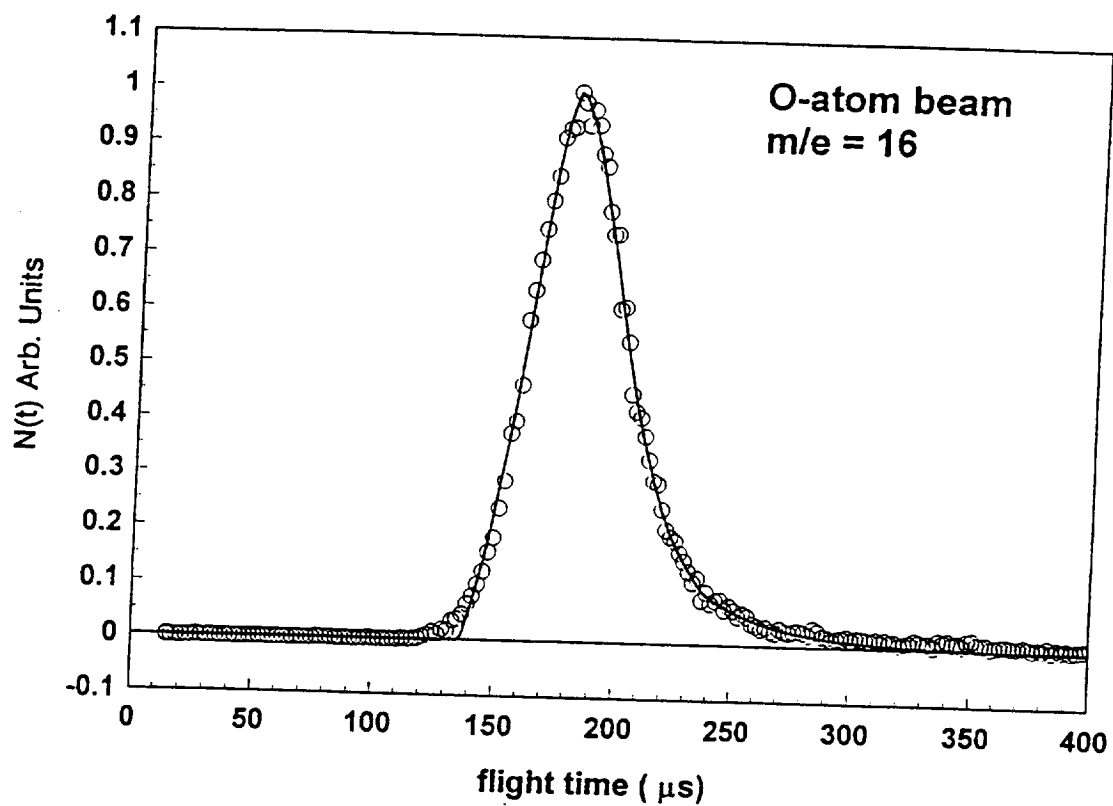


Figure 3-8. Time-of-flight and translational energy distributions of the O-atom component in the molecular beam.

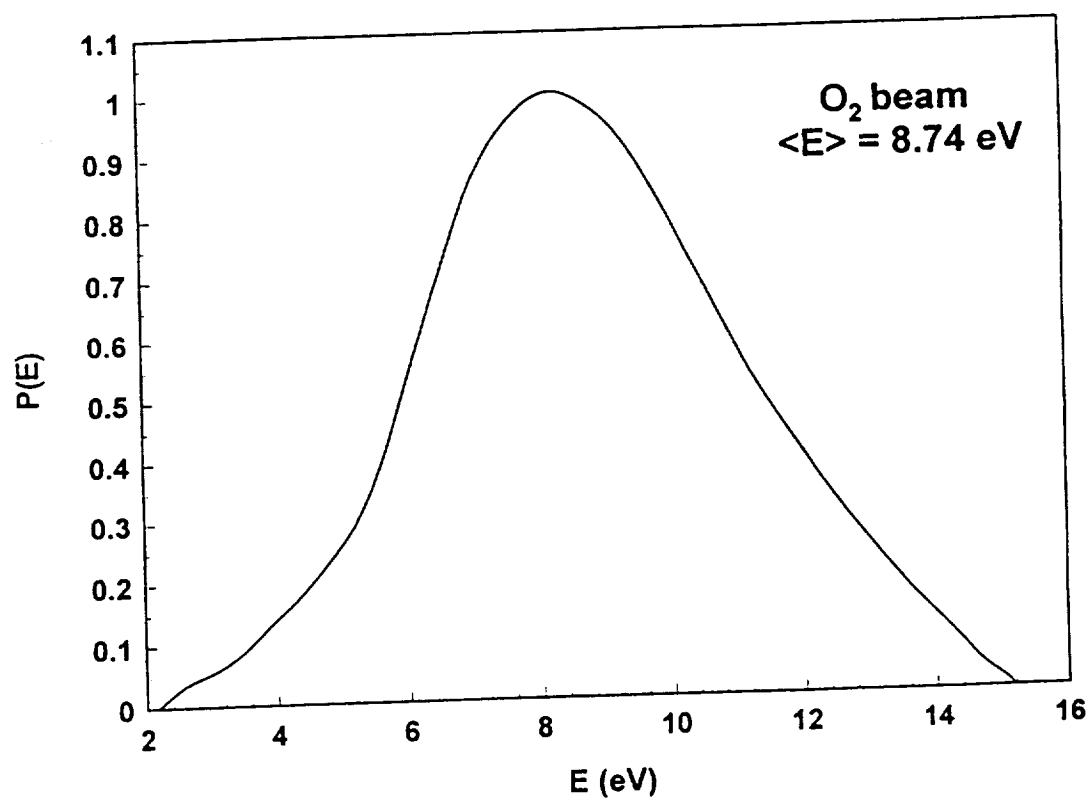
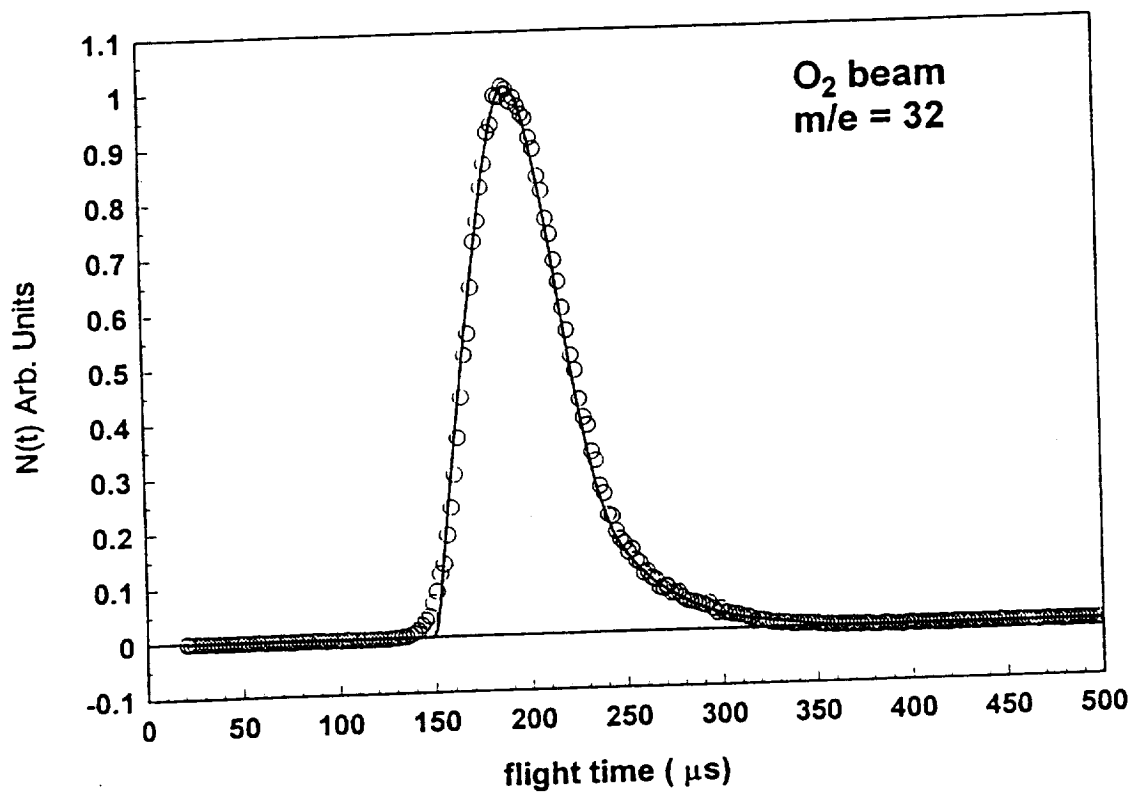


Figure 3-9. Time-of-flight and translational energy distributions of the fast  $O_2$  component in the molecular beam.

## 4.0 Results and Discussion

This section provides discussion of the effects of the flight exposure environment on the various material samples, as deduced by visual inspection, macroscopic photography, Electron Spectroscopy for Chemical Analysis (ESCA), Atomic Force Microscopy (AFM), Scanning Electron Microscopy (SEM), and High-Performance Liquid Chromatography (HPLC). Mass change data and ESCA data referenced here are provided in appendices to this report.

### 4.1 Passive Tray Samples

Passive tray specimens from EOIM-3 were removed and examined for comparative analysis of the effects of atomic oxygen exposure. The next sections describe those results.

#### 4.1.1 Fluorinated Polystyrene Materials

Visual inspection and macrophotography of the flight materials revealed a nonspecular surface in the area exposed to atomic oxygen. Weight loss measurements and erosion depth measurements from "mesas" found in SEM images (Figure 4-1) of the exposed surface indicate that fluorination of the backbone chain affords greater protection from atomic oxygen attack than ring fluorination. The nonfluorinated polystyrene material eroded approximately  $7.7 \pm 1.1 \mu\text{m}$ , corresponding to an erosion yield of  $3.2 \times 10^{-24} \text{ cm}^3/\text{AO}$ . The ring-fluorinated polystyrene eroded approximately  $4.0 \pm 1.0 \mu\text{m}$  while the backbone-fluorinated polystyrene eroded only  $2.5 \pm 0.6 \mu\text{m}$ . Analysis of the ESCA data reveals that the ratio of fluorine to carbon decreases dramatically for ring-fluorinated polystyrene, whereas the same ratio remains almost unchanged for the backbone-fluorinated polymer. The ESCA results support an erosion model where the pentafluorophenyl ring is removed by atomic oxygen attack, leading to fluorine depletion of the ring-fluorinated polymer. The importance of protecting the polymer chain in order to reduce atomic oxygen attack is clearly illustrated for this series of polymers.

#### 4.1.2 Spectrolon

Visual inspection and macrophotography reveal very little, if any, change in the appearance of the Spectrolon specimens. Results from spectral reflectance measurement show only minor decrease in reflectance in the short wavelength region for the 100-percent reflectance specimen (see

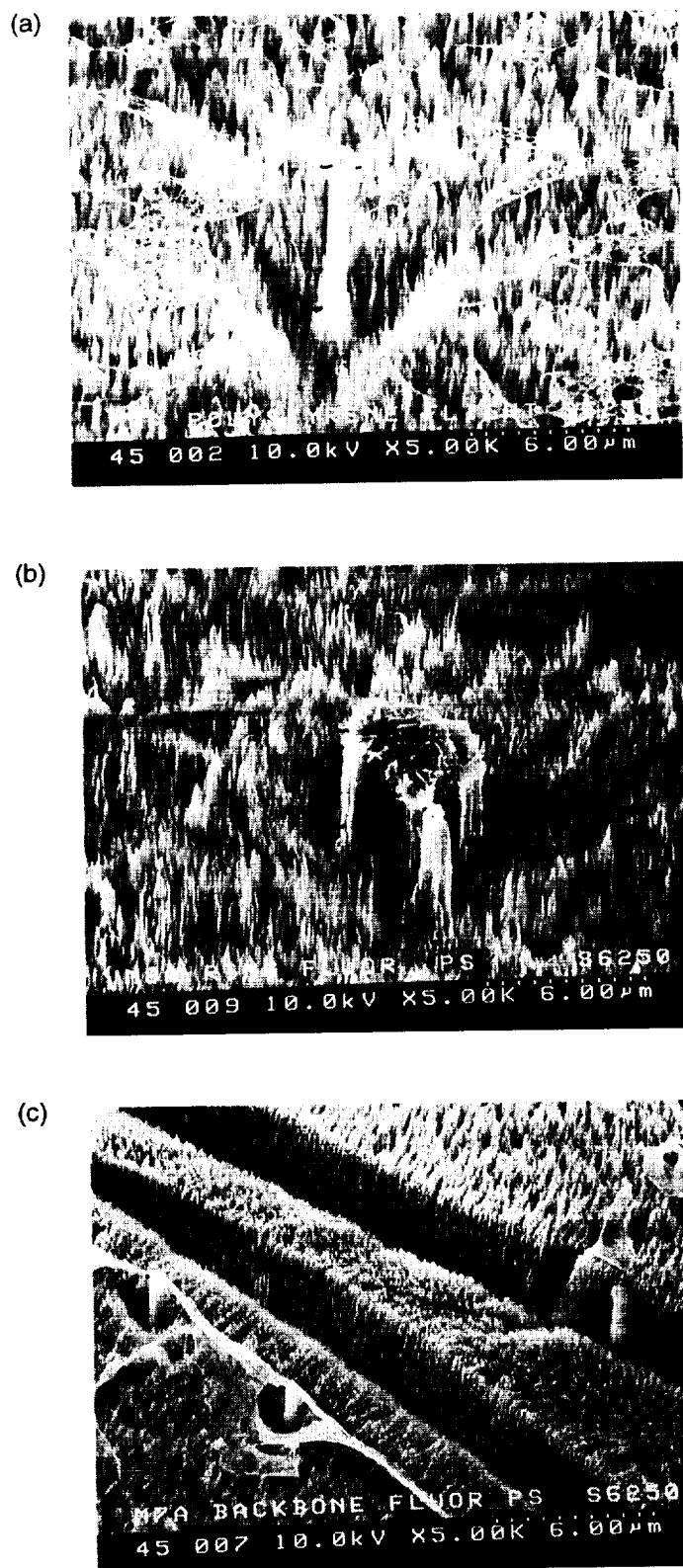


Figure 4-1. SEM photographs of polystyrene: (a) control, (b) ring-fluorinated, and (c) backbone-fluorinated.



Figure 4-2). Reflectance spectra for the carbon-loaded Spectrolon materials did not reveal significant differences for exposed versus control specimens. The ESCA data indicate minor oxidation of the Spectrolon specimens with no discernable trend with increased carbon loading. The carbon particles used in the lower reflectance Spectrolon are apparently sufficiently protected by the PTFE binder to prevent significant loss of carbon content at EOIM-3 atomic oxygen fluence levels. The 100-percent Spectrolon specimen exhibited fluorescence in the exposed region. This phenomenon has been reported for LDEF and other EOIM-3 test materials examined by NASA Marshall Space Flight Center.

#### **4.1.3 White Paints**

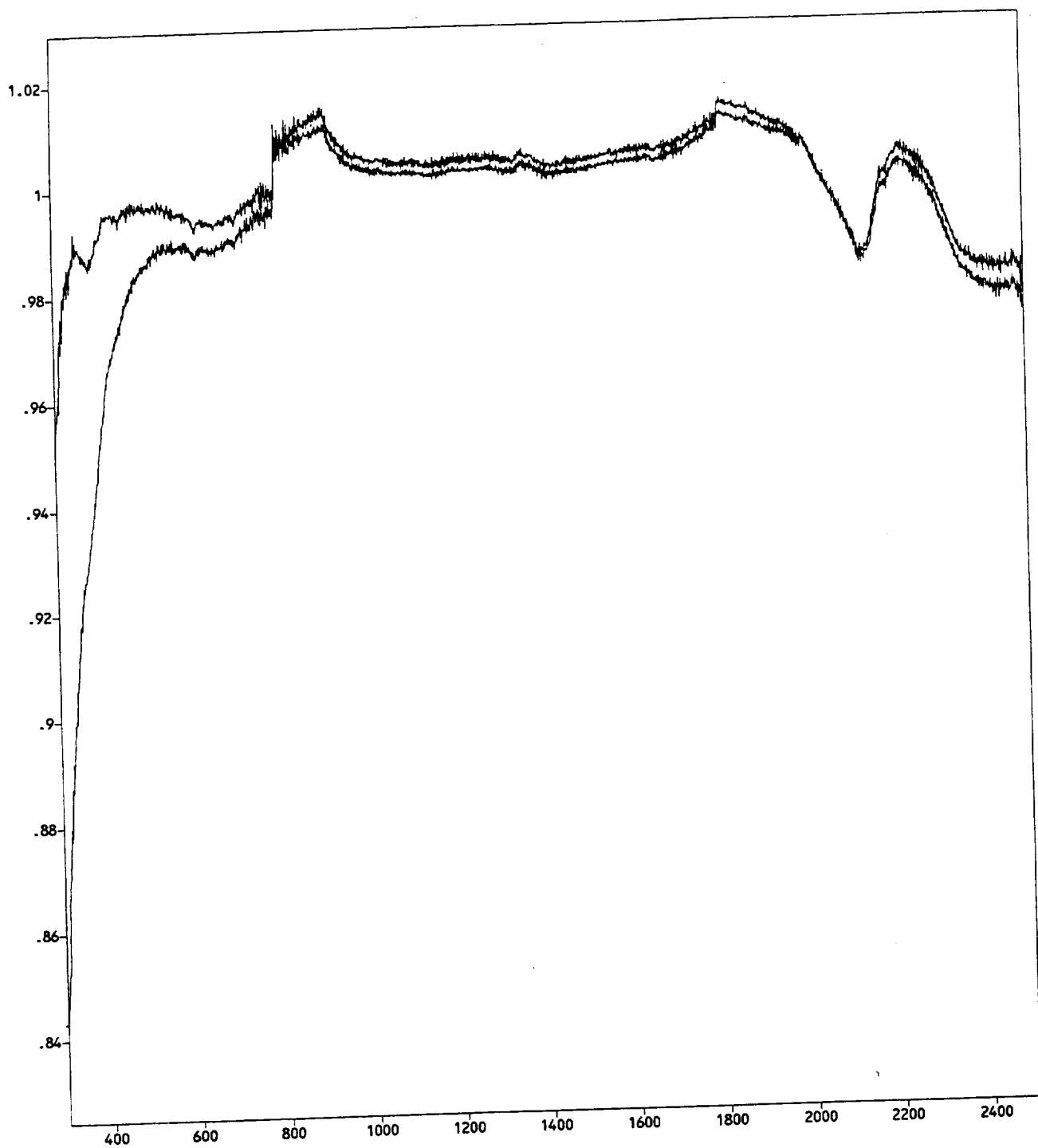
Visual and macrophotography revealed no apparent changes in the polyphosphazene- and silicate-bound ZOT paints. Measurement of thermo-optical properties ( $\alpha, \epsilon$ ) showed no change in the HINCOR (silicate) paints as a result of atomic oxygen exposure. The ESCA data for the HINCOR paint also attest to the exceptional stability of the inorganic paint to atomic oxygen. The polyphosphazene-bound paint showed an expected increase in phosphorus and oxygen content, indicating the propensity for polyphosphazene to form an inorganic phosphate glass coating upon atomic oxygen exposure.

### **4.2 Heated Tray and Heated Strip Samples**

From visual inspection and macrophotography, the copper strips used for mounting the test strip specimens underwent obvious changes in oxidation as a result of exposure to atomic oxygen at elevated temperatures. The most severe oxidation occurred at 473 K (200°C), with the copper strip appearing almost black, while only slight oxidation was witnessed in the 333 K (60°C) copper strip. (See Figure 4-3.)

#### **4.2.1 Carbon/Carbon Materials**

Visual inspection and macroscopic photography of the carbon/carbon disks clearly showed evidence of surface roughening in the exposed regions (Figure 4-4). The somewhat lustrous surface of the carbon/carbon composite appeared flat black following atomic oxygen exposure. Examination



File # 2 = DATA\_17

Transmittance / Nanometers

Res = None

M14A-1

Figure 4-2. Spectral reflectance for exposed (lower) and control (upper) 100-percent reflectance Spectrolon.

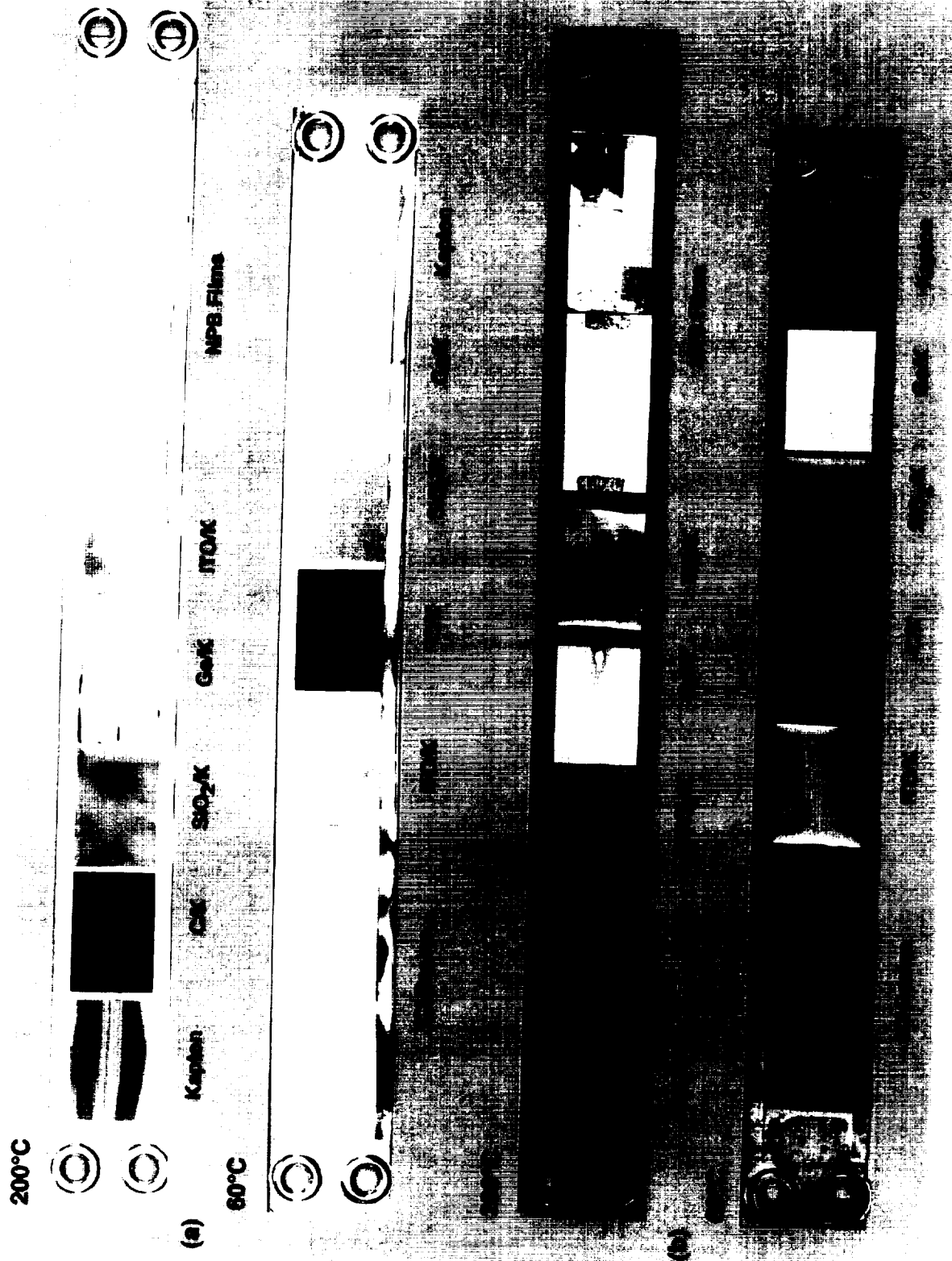
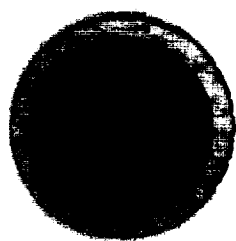
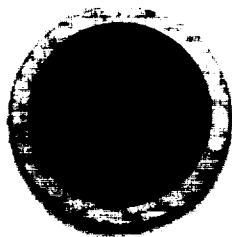


Figure 4-3. Photograph of the heated strip APSA samples: (a) preflight and (b) postflight.

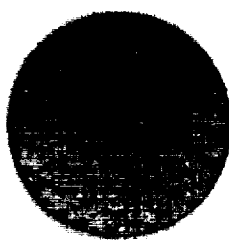




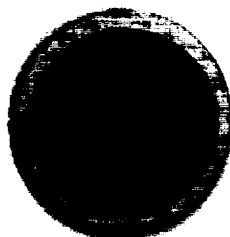
**a) 200°C**



**b) 60°C**



**c) Control**



**d) Passive**

Figure 4-4. Postflight photograph of TS15 carbon/carbon composite samples in the heated tray experiment.



of the SEM images (Figures 4-5 to 4-7) of the composite materials indicated that the extent of erosion increased with increasing temperature. Laboratory and earlier flight experiments indicate that the reaction rate of atomic oxygen and carbon increases rapidly with temperature. Analysis of the ESCA data for the three carbon/carbon materials on EOIM-3 heated trays reveals an interesting trend. The maximum oxidation level is witnessed in the 333 K (60°C) specimens (18–20 percent). The ambient and high temperature specimens (473 K/200°C) consistently show slightly reduced surface oxygen content (15–18 percent). A direct reaction model does not predict such a variation of surface oxidation with temperature. Secondary surface reactions could explain this behavior. Measurements of the solar absorptance and hemispherical emittance for one of the carbon/carbon materials is tabulated below.

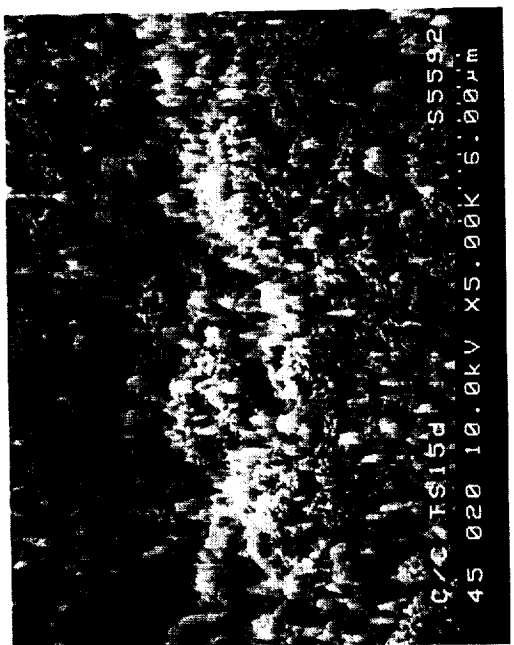
Table 4-1. Temperature dependence of atomic oxygen erosion and thermo-optical properties of EOIM-3 carbon/carbon composite

Specimen	Erosion ( $\mu$ )	$\alpha$	$\epsilon$
SP-18C (Control)	----	0.76	0.41
SP-18D (Ambient)	< 1.0	0.78	0.44
SP-18A (473 K (200°C))	2.0	0.85	0.47

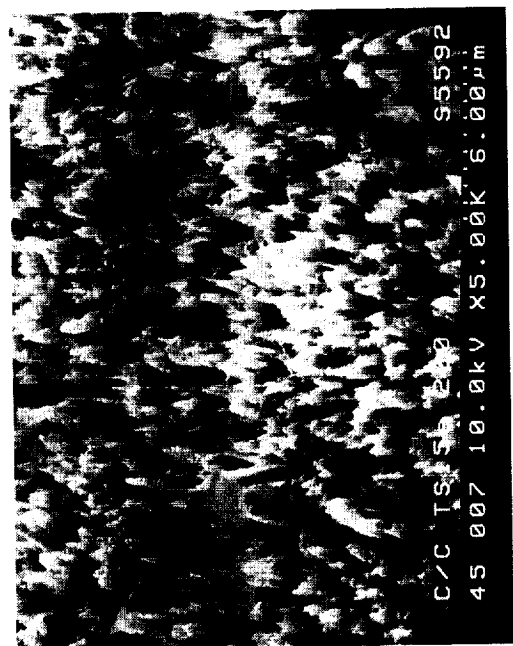
The increases of solar absorptance, hemispherical emittance, and erosion are correlated with the temperature of the test article during atomic oxygen exposure.

#### 4.2.2 APSA Substrates

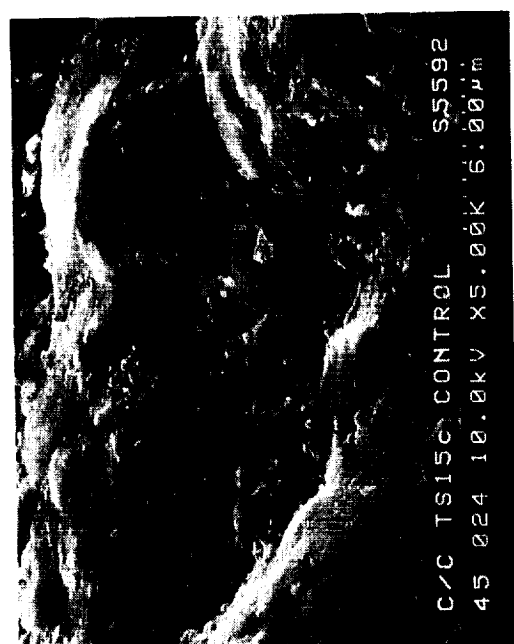
Visual inspection and macrophotographs of the APSA Kapton film specimens showed little damage to the coated films, but distinctive loss of specularly of the unprotected and carbon-loaded Kapton films was apparent. No weight loss data is available for these specimens. The unprotected Kapton films eroded approximately 7  $\mu$ m on both the 333 K (60°C) and 473 K (200°C) strips as determined from analysis of SEM images (Figure 4-8). Carbon-loaded Kapton eroded about 5  $\mu$ m with no discernable differences noted in the SEMs for the 333 K (60°C) and 473 K (200°C) specimens (Figure 4-9). SEM images of the surface of SiO<sub>x</sub>-coated Kapton showed extensive crazing and cracking in both the 333 K (60°C) and 473 K (200°C) specimens (Figure 4-10). Some



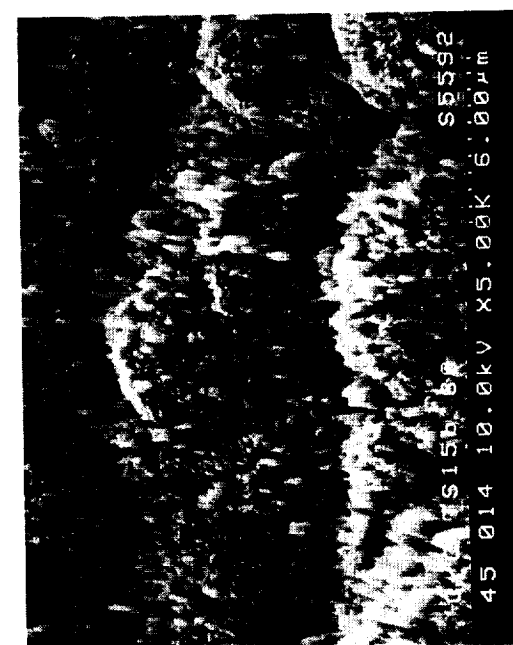
(a)



(b)



(c)



(d)

Figure 4-5. SEM photographs of TS 15 carbon/carbon composite: (a) control, (b) ambient, (c) 333 K (60°C), and (d) 473 K (200°C).



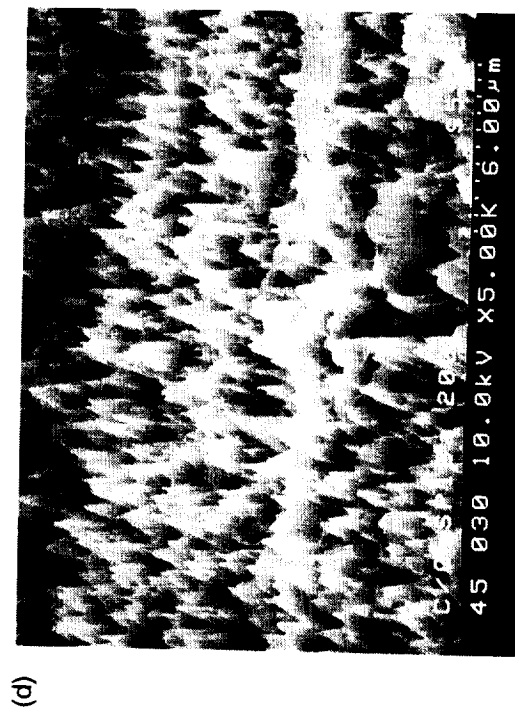
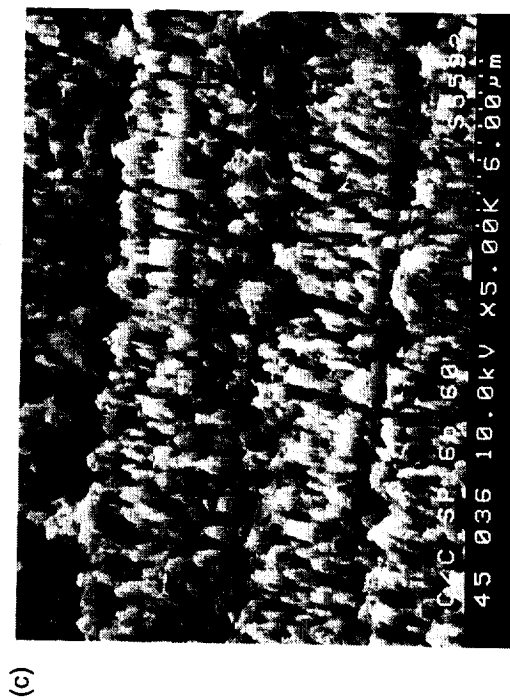
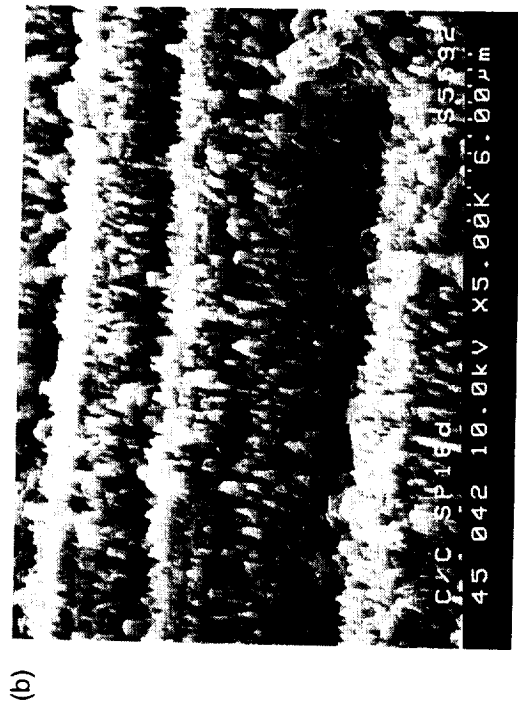
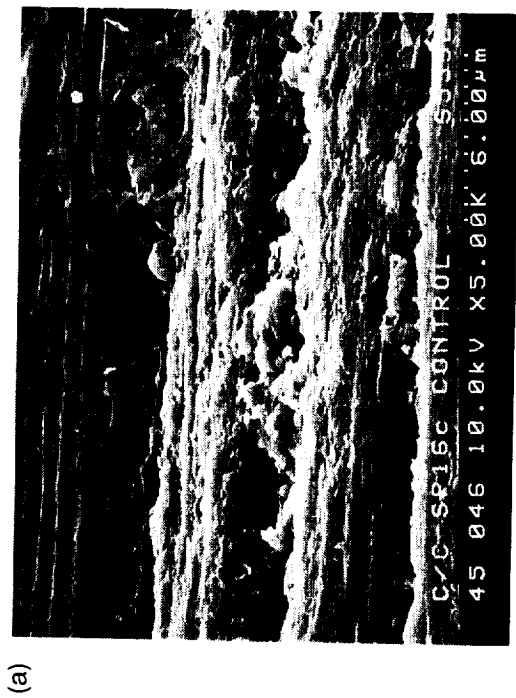


Figure 4-6. SEM photographs of SP 16 carbon/carbon composite: (a) control, (b) ambient, (c) 333 K (60°C), and (d) 473 K (200°C).

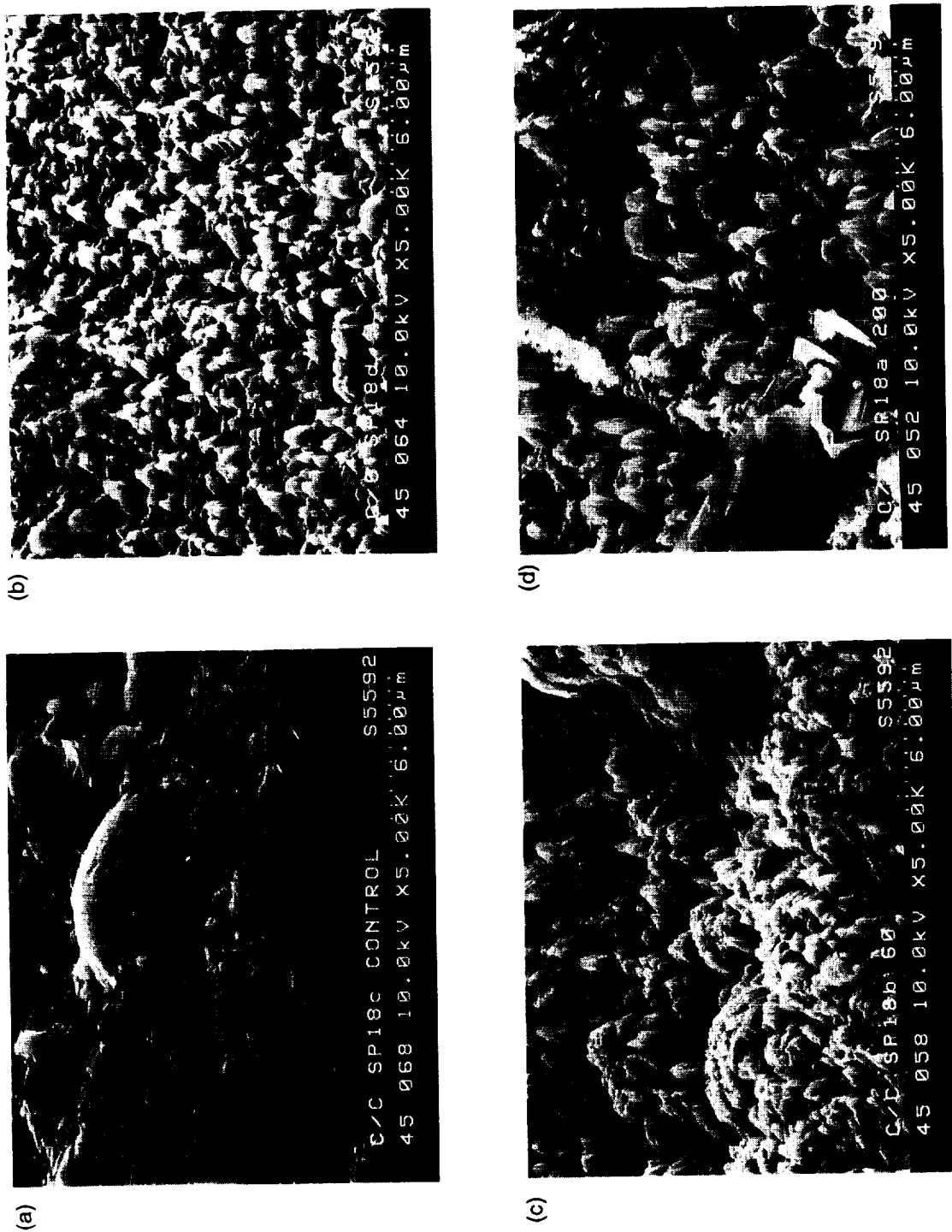


Figure 4-7. SEM photographs of SP 18 carbon/carbon composite: (a) control, (b) ambient, (c) 333 K (60°C), and (d) 473 K (200°C).

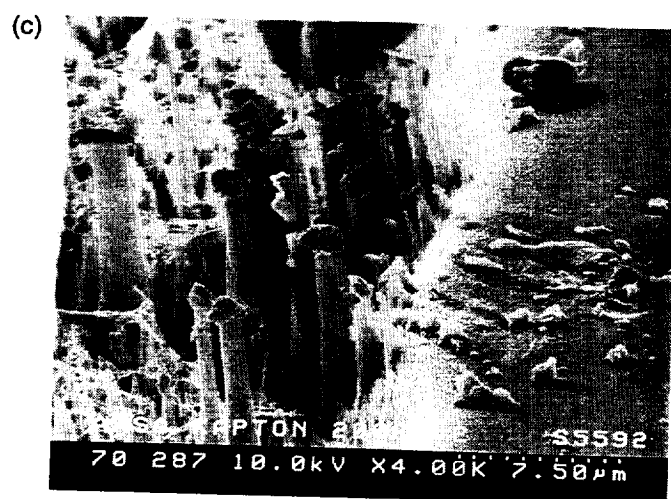
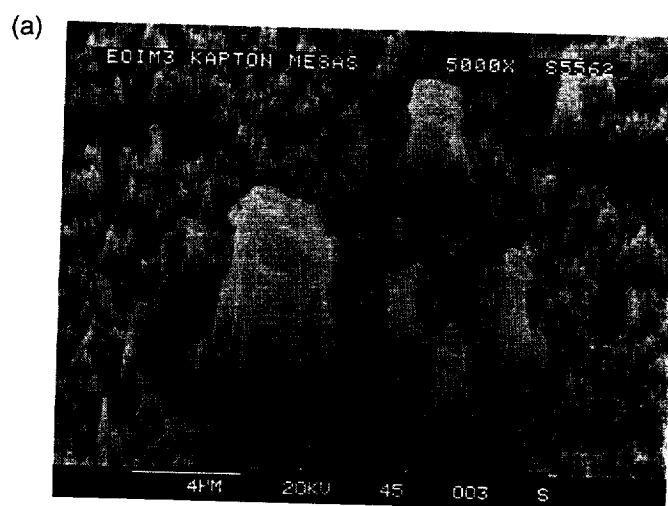
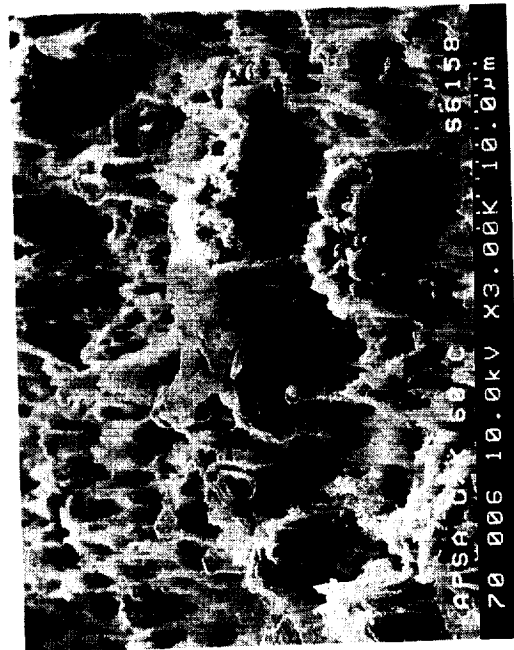


Figure 4-8. SEM photographs of unprotected Kapton: (a) ambient, (b) 333 K (60°C), and (c) 473 K (200°C).



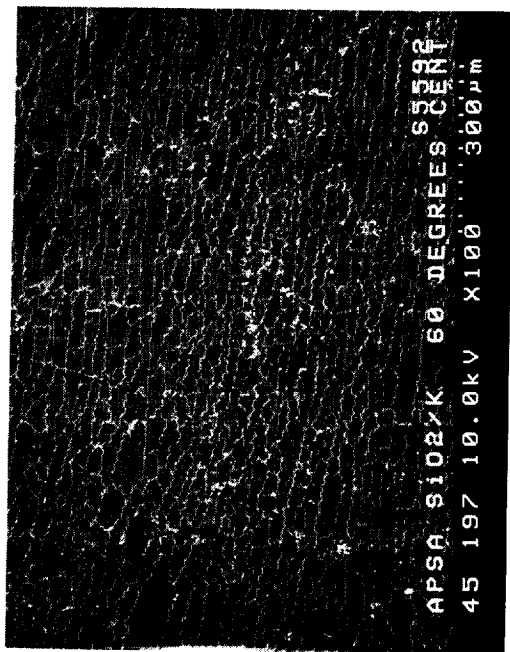
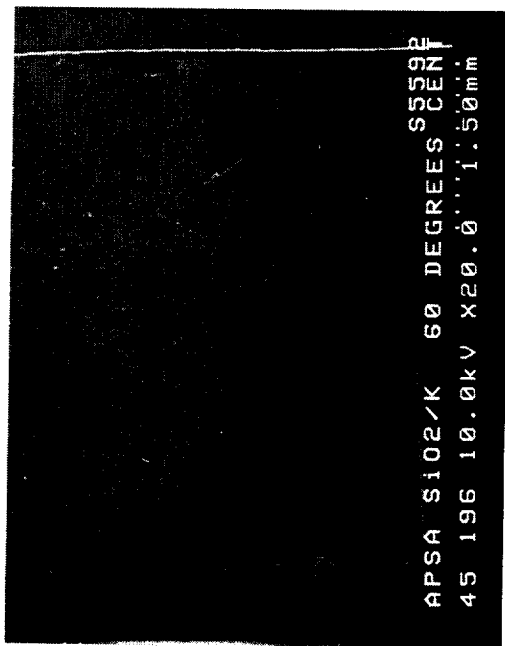
(b)



(a)

Figure 4-9. SEM photographs of carbon-loaded Kapton: (a) 333 K (60°C) and (b) 473 K (200°C).

(a)



(b)

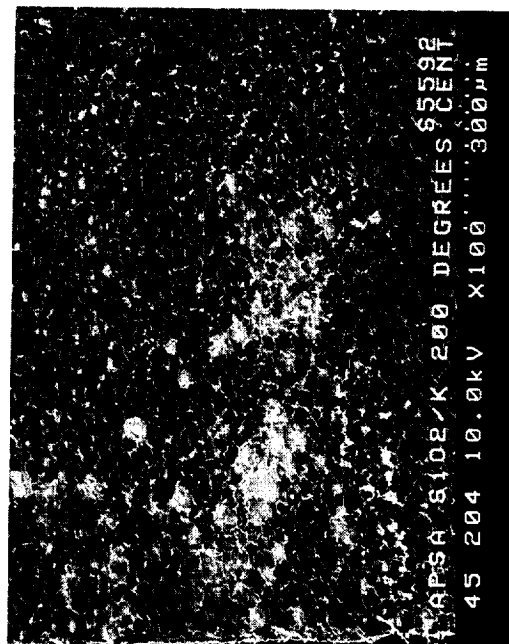


Figure 4-10. SEM photographs of SiO<sub>x</sub>-coated Kapton: (a) 333 K (60°C) and (b) 473 K (200°C).

evidence for undercutting and deep erosion of the underlying Kapton was observed in cracks and local flaws in the coating. The ITO-coated Kapton showed some localized delamination in the 333 K (60°C) specimen with more extensive and regular (rectangular) cracking in the 473 K (200°C) test strip (Figure 4-11). Undercutting and erosion of the Kapton was again visible beneath the delaminations and in the cracks. The germanium-coated Kapton showed very little evidence for cracking, crazing, or delaminations in the 333 K (60°C) specimen, although some flaws and scratches were observed (Figure 4-12). The 473 K (200°C) specimen did show crazing and slight delamination of the germanium coating. Among the thin-film-coated Kapton substrates, the germanium-coated material performed the best, while the SiO<sub>x</sub>-coated material performed the worst.

The germanium-coated Kapton films also provided a study in oxidation chemistry of a semiconductor material. High-resolution ESCA data for the germanium 3-D peaks near 30 eV were analyzed to determine the thickness of the oxide "skin" on the germanium-coated Kapton specimens. The thickness of the oxide layer of germanium was found to *decrease* with increasing temperature as tabulated below.

Table 4-2. Temperature dependence of oxide layer thickness for EOIM-3 germanium-coated Kapton

Specimen Location	GeO <sub>x</sub> Thickness (nm)
Passive (283–313K or 10°–40°C)	6
333 K (60°C) Strip	4
473 K (200°C) Strip	2

The variation in oxide thickness may be attributed to formation of volatile GeO by either direct reaction of atomic oxygen with germanium or disproportionation of stable GeO<sub>2</sub>.

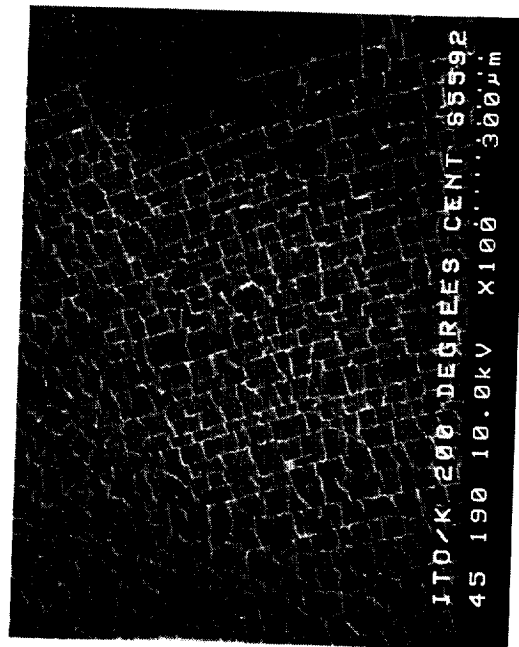
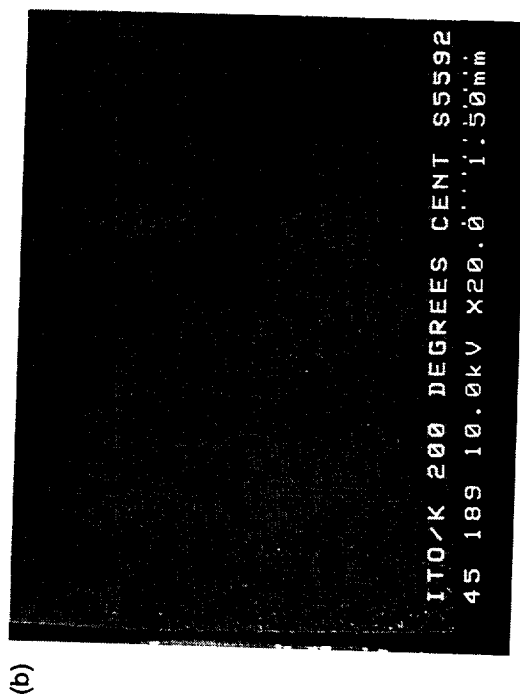
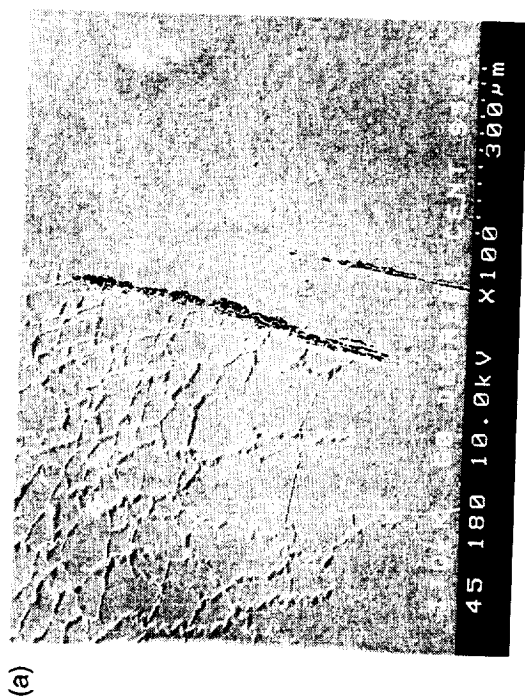
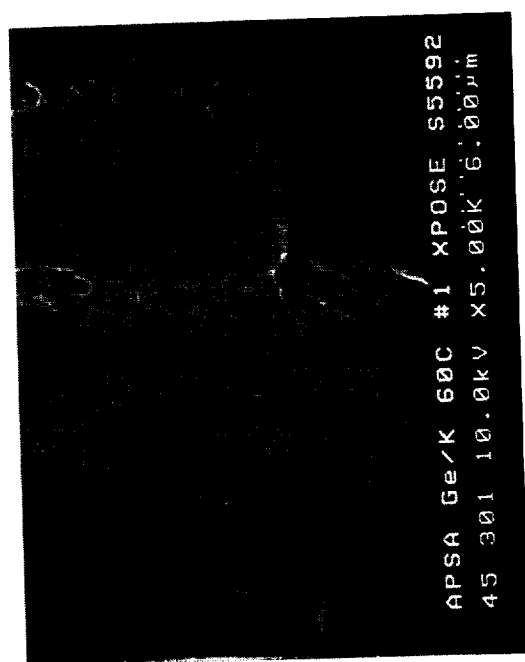
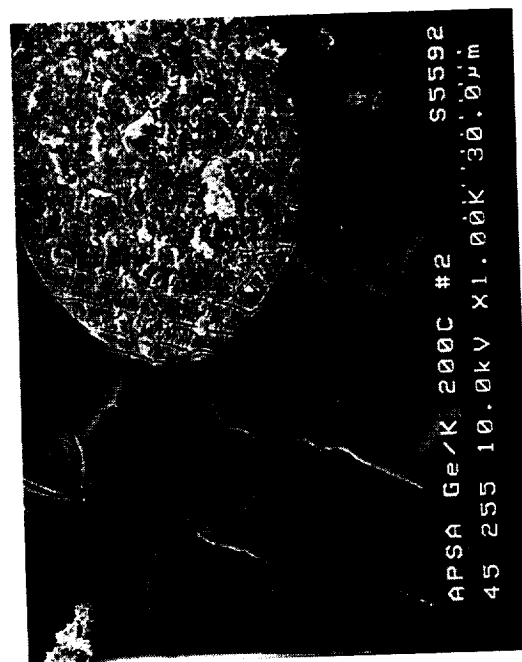


Figure 4-11. SEM photographs of ITO-coated Kapton: (a) 333 K (60°C) and (b) 473 K (200°C).



(a)



(b)

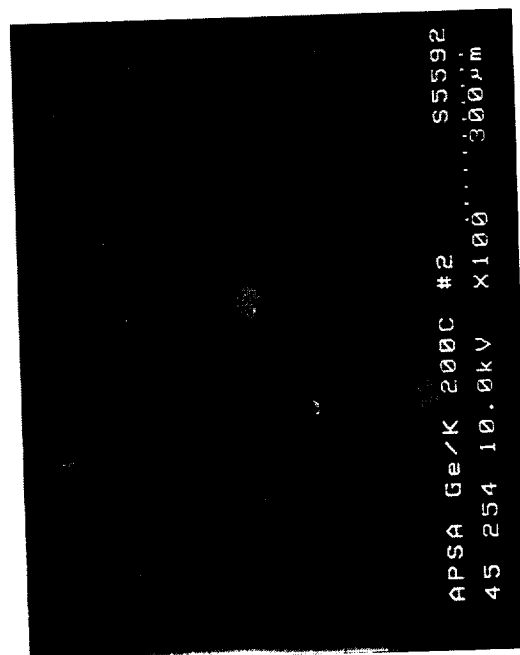
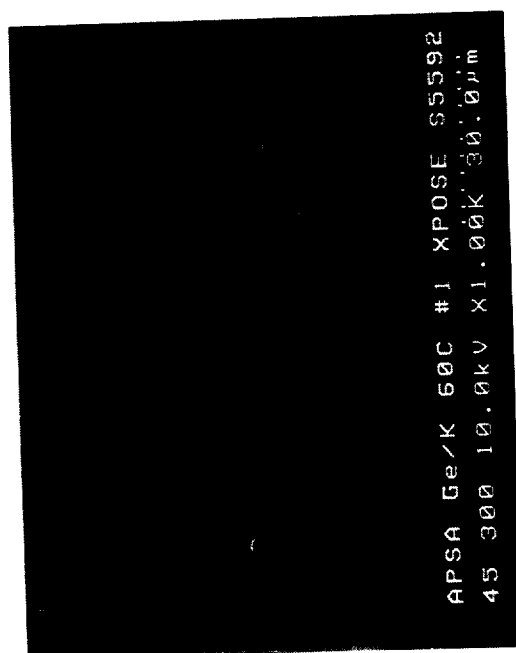


Figure 4-12. SEM photographs of germanium-coated Kapton: (a) 333 K (60°C) and (b) 473 K (200°C).



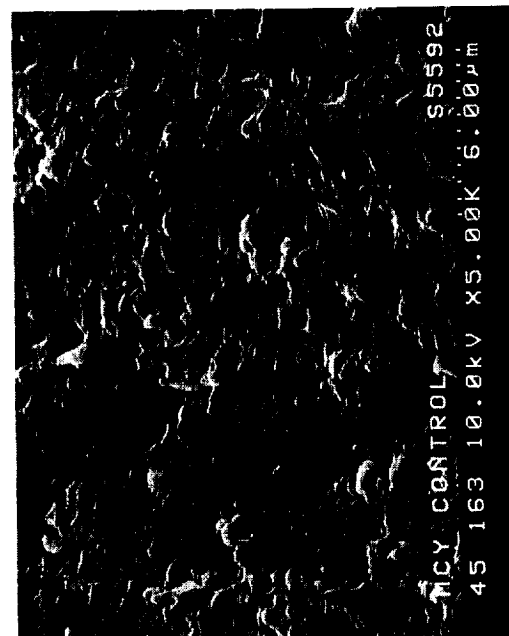
The germanium coating also proved to be an excellent surface for determining the thickness of silicon oxide contamination. The silicon 2p peak area was compared to germanium 3-D peak areas. Assuming the silicon oxide resides on the surface of the germanium coating, an approximate silicon oxide thickness of 2 nm (20 Å) was estimated from the ESCA data.

#### *4.2.3 Polycyanate and Modified-Polycyanate Resins*

Due to the initial roughness of the polycyanate resin specimens, visual inspection and macrophotography does not provide a clear indication of atomic oxygen induced roughening of these test articles. However, SEM images and mass loss data provide a clear indication of the relative erosion characteristics for the base (BCY) and siloxane-modified (MCY) polycyanate materials (see Figures 4-13 and 4-14). The mass loss for the MCY specimen was 20 percent of the value observed for the BCY specimen. This result, though, should not be construed to imply that the erosion rate for MCY is one-fifth that for BCY. The SEM images show clear differences in the erosion morphologies for the two materials. The base cyanate developed the familiar "shag-carpet" erosion morphology witnessed in readily attacked materials such as Kapton. Erosion "mesas" with a height on the order of 3  $\mu\text{m}$  are observed in the base material. The siloxane-modified material shows a "blotchy" erosion surface rather than the well-defined peaks witnessed in the base material. This morphology indicates that the siloxane-modified material may consist of domains of siloxane-rich regions scattered throughout the bulk material. The ESCA data for the modified material show a considerable increase in the surface concentration of silicon in the exposed region. The unexposed material contains approximately 5 percent surface silicon as compared to 25 percent surface silicon for the atomic oxygen-exposed material. This is consistent with the formation of a protective silicon-oxide-enriched "skin" on the MCY specimen as a result of atomic oxygen attack.

#### **4.3 Scatterometer Samples**

Kapton samples that were exposed to indirect attack from atomic oxygen in the scatterometer showed little evidence of erosion. Based on the geometry of the scatterometer, the O-atom fluence on the scatterometer samples is estimated to be less than 10 percent of the ram fluence for the EOIM-3 experiment, so the erosion yield should be low even if the scattered O atoms have the same reactivity as those that impinge directly. Assuming the reduced fluence was  $1 \times 10^{19}$  atoms/cm<sup>2</sup> and a typical reactivity of  $3 \times 10^{-24}$  cm<sup>3</sup>/atom, the recession of the Kapton surface would be about

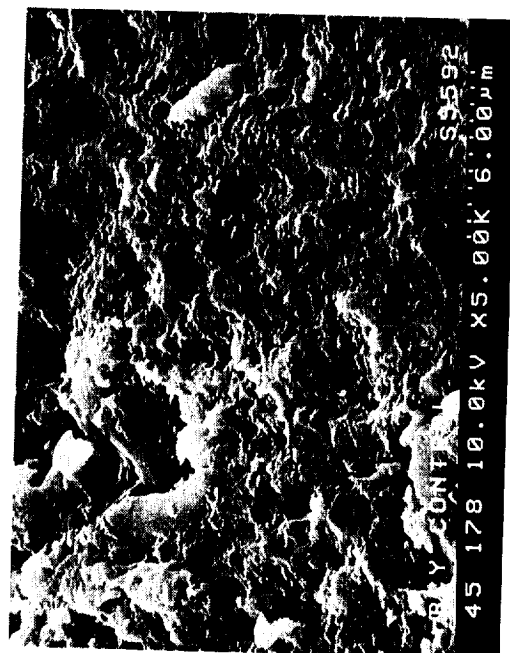


(a)

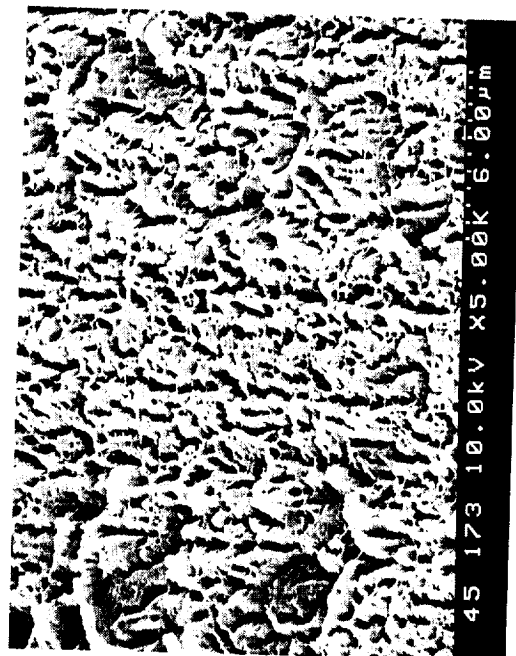


(b)

Figure 4-13. SEM photographs of base polycyanate: (a) control and (b) 333 K (60°C).



(a)



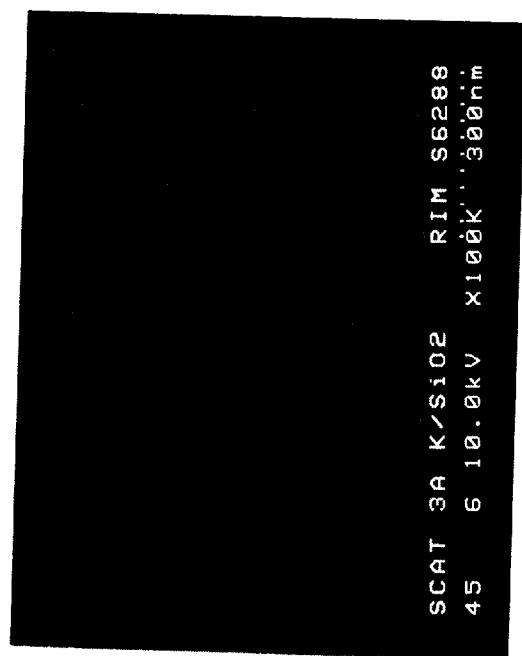
(b)

Figure 4-14. SEM photographs of siloxane-modified polycyanate: (a) control and (b) 333 K (60°C).

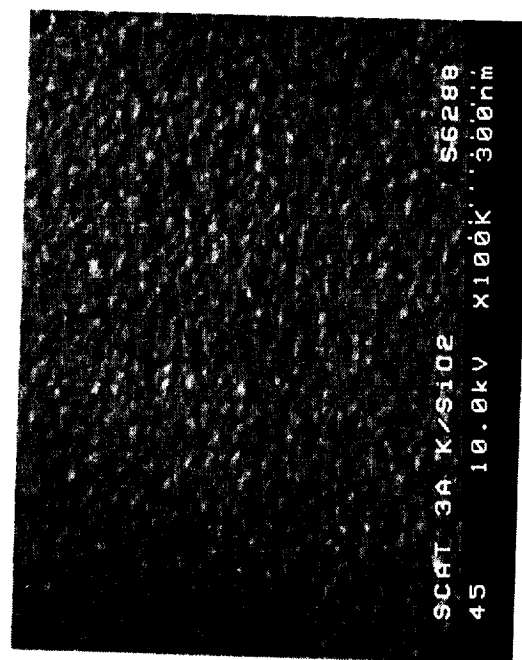
300 nm. Even this low level of erosion should lead to a roughened surface that could easily be seen with the use of a scanning electron microscope; however, scanning electron micrographs of the surfaces showed that they were only slightly roughened. Figure 4-15 shows a SEM photograph of protected and unprotected Kapton that was exposed in the scattering chamber with  $\text{SiO}_2$  as the scattering surface. The exposed surface appears more grainy than the unexposed surface, with a "grain" size less than 30 nm. This example is typical of all the scatterometer samples, which exhibited negligible roughening compared to what would be expected if the fluence on the surfaces came from direct attack from O atoms in the ram. It thus appears that scattered oxygen atoms have reduced reactivity, regardless of the surface from which they scatter.

Although erosion was negligible, the sample surfaces did become oxidized to levels that are typical of Kapton exposed to ram attack (20–24 percent). The results of ESCA survey spectra that sampled a region near the center of each test specimen are found in Appendix C. Each of the Kapton specimens, with the exception of the  $\text{SiO}_2$  scattering target specimen, shows an increase in the relative amount of surface oxygen. The reason for the lack of increased oxidation of the  $\text{SiO}_2$  scattering specimen is unclear.

The observation that scattered oxygen atoms have reduced reactivity confirms the implication of recent inelastic scattering results (see Section 4.6.3) that fast O atoms lose a large fraction of their kinetic energy when they bounce off a surface and thereby become less reactive. The experiments at JPL show that O atoms with kinetic energies of about 5 eV almost always lose more than 50 percent of their initial energy even after one bounce from a surface. In addition, a relatively small fraction (<20 percent) of the scattered O atoms have reached thermal equilibrium with the surface. The exact amount of energy transfer depends on the sum of the initial and final scattering angles, with energy transfer being less for more grazing collisions. Also, the nature of the surface plays an important role in energy transfer. Surfaces that are very smooth and have high molecular weight constituents or a "stiffer" molecular structure lead to low energy transfer. On the other hand, surfaces that are rough with low molecular weight or that are more "pliable" tend to have stronger interactions with incoming atoms and thus lead to more energy transfer. Nevertheless, the average fractional energy transfer is significant, varying from approximately 50 to 90 percent, with



(a)



(b)

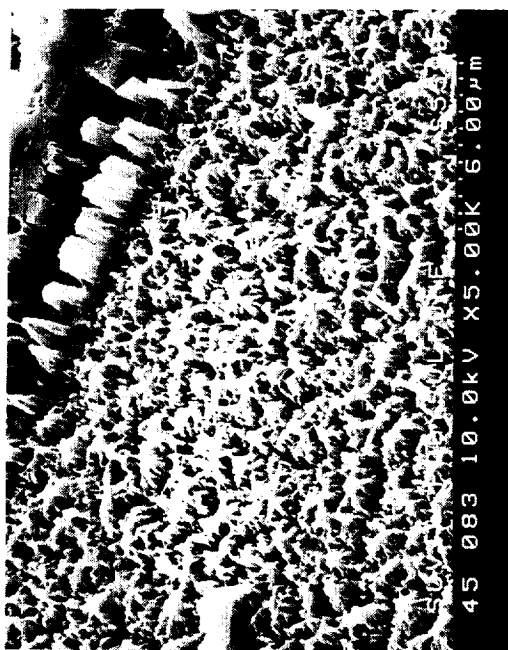
Figure 4-15. SEM photographs of Kapton-HN scatterometer sample with SiO<sub>2</sub> as the scattering surface: (a) surface protected under rim of clamp and (b) exposed region.

polymers tending to absorb more energy than inorganic compounds. Thus, the scattering results suggest that the kinetic energies of the O atoms impinging on the sample surfaces in the scatterometers was in the range of 1-2 eV. The fact that the erosion of the samples was negligible further suggests a strong energy dependence on the O-atom reactivity, although it is difficult to derive the functional form of the dependence. While it is tempting to look for more erosion in the samples that were in the chambers with smooth, inorganic scattering surfaces ( $\text{SiO}_2$  and  $\text{Al}_2\text{O}_3$ ), these are the surfaces that should most efficiently scatter incoming O atoms back in the opposite direction from which they came; therefore, the fluence on the test samples in these chambers should be less than that on the samples in the chambers with the polymer and carbon-13 (rough) surfaces. Furthermore, the energy of the scattered O atoms in any chamber may be low enough to make the erosion rate vanishingly small.

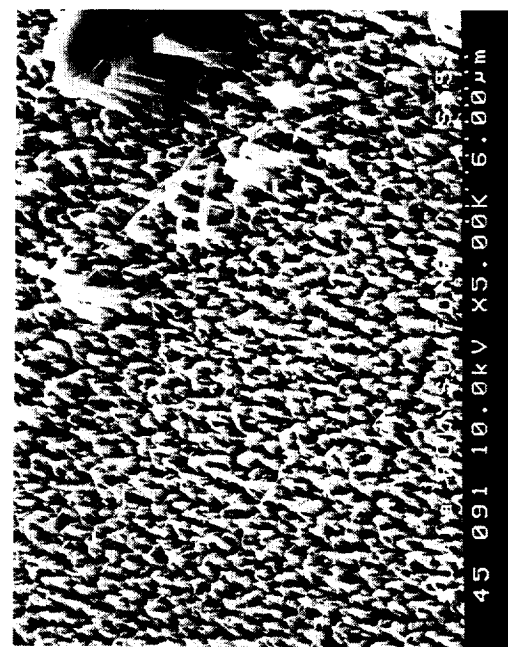
While the scattered O atoms do not appear to induce much erosion in the test samples, they do oxidize them. Even though the erosion rate is small, close inspection with electron microscopy does show that the scatterometer samples had a slight increase in surface roughness. Thus, O atoms did react, albeit with low probability. Perhaps these surfaces that were in the early stages of erosion had already reached a steady state of surface oxidation. Earlier (unpublished) JPL experiments have shown evidence for a plateau in the level of surface oxidation of polyethylene when the fluence exceeded  $\sim 10^{18}$  atoms/cm<sup>2</sup>.

#### 4.4 Solar UV Samples

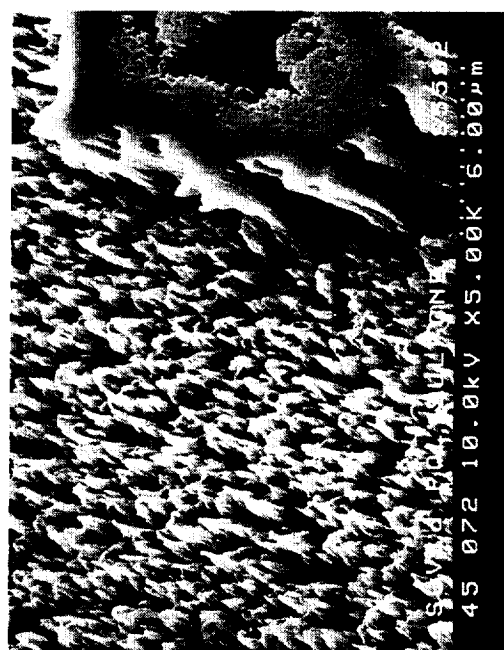
The solar UV specimens were de-integrated at NASA/JSC under the direction of the EOIM-3 experiment manager. The specimens were shipped to JPL for subsequent analysis. SEM images of polysulfone, PMMA, and polystyrene are presented in Figures 4-16 to 4-18, respectively. The data in Table 4-3 summarizes mass loss and erosion information for the solar UV experiment specimens. The data shown for Kapton erosion, as determined by profilometry, was reported by NASA/JSC (S. Koontz). The raw mass data are provided in Appendix B.



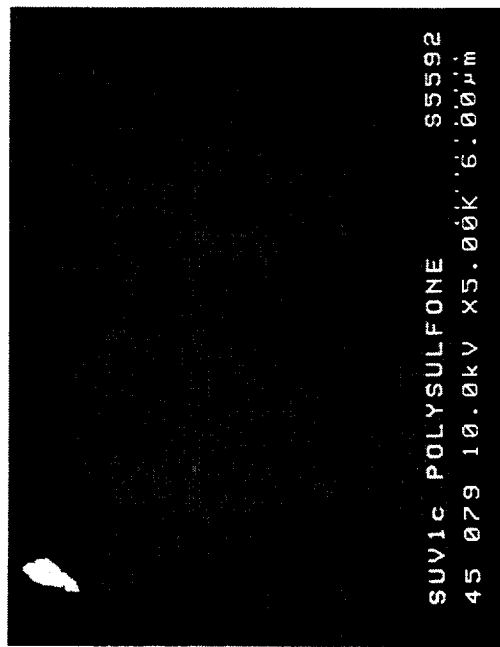
(a)



(b)

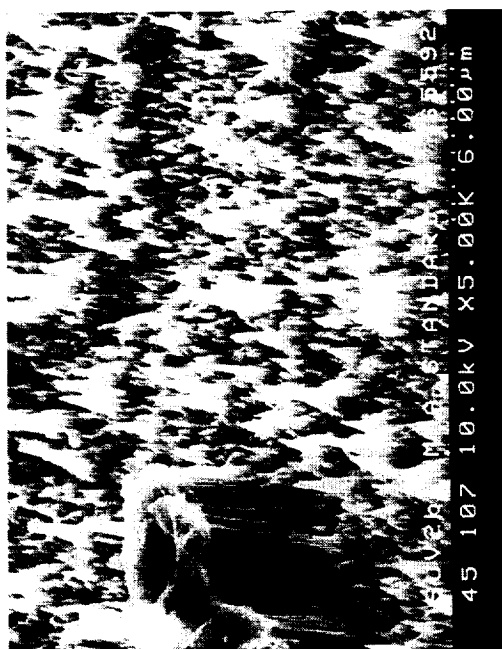


(c)



(d)

Figure 4-16. SEM photographs of polysulfone: (a) day, (b) night, (c) control, and (d) day and night exposure.



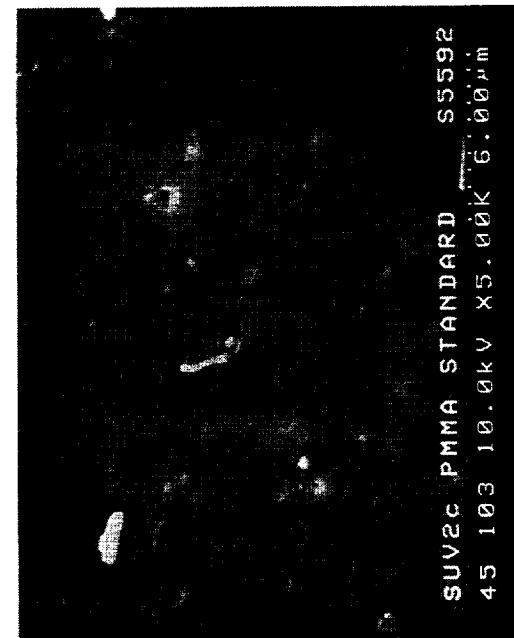
(a)



(b)



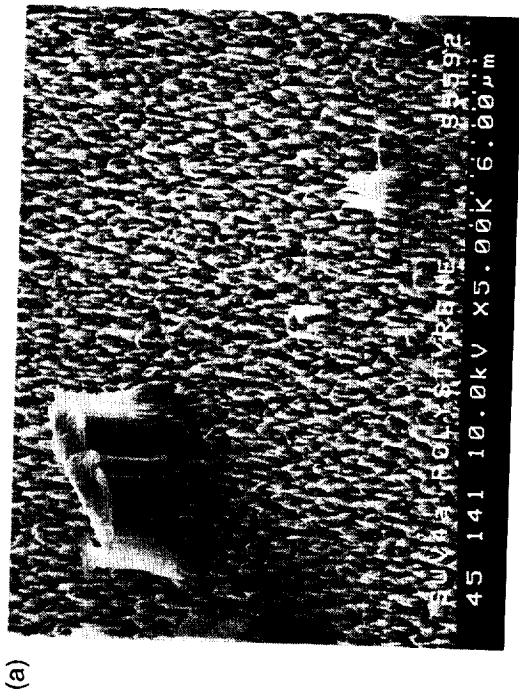
(c)



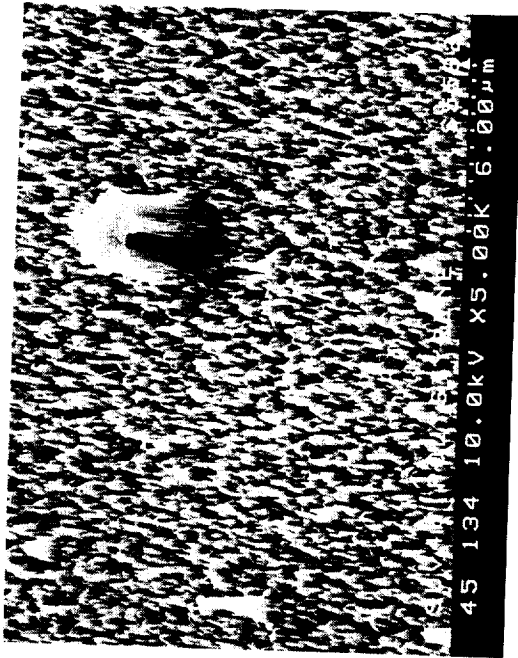
(d)

Figure 4-17. SEM photographs of PMMA: (a) day, (b) night, (c) control, and (d) day and night exposure.

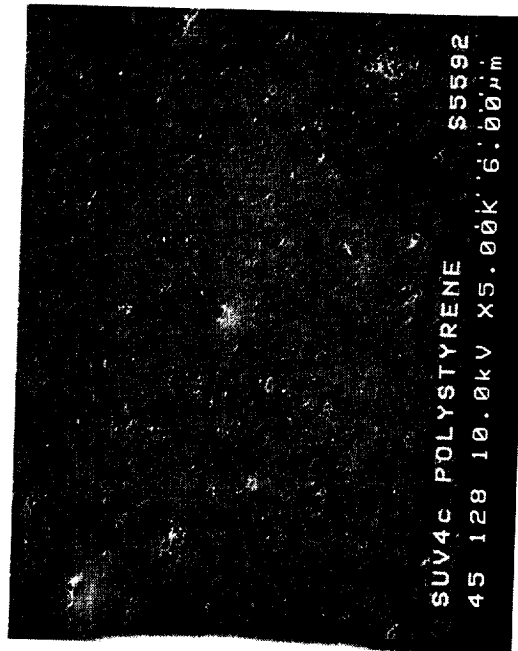




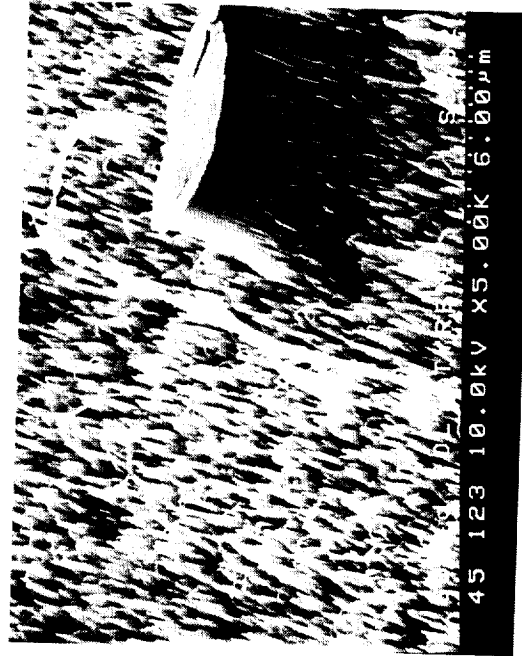
(a)



(b)



(c)



(d)

Figure 4-18. SEM photographs of polystyrene: (a) day, (b) night, (c) control, and (d) day and night exposure.

Table 4-3. Mass loss and erosion data for EOIM-3 solar UV specimens

Material (Exposure)	Mass Loss (mg)	Erosion Depth ( $\mu\text{m}$ ) (mass loss)	Erosion Depth ( $\mu\text{m}$ ) (SEM mesa)
Kapton (Day)	N/A	N/A	5.03*
Kapton (Night)	N/A	N/A	3.08*
Kapton (Full)	N/A	N/A	8.11*
Polysulfone (Day)	1.49	3.0	4.0
Polysulfone (Night)	0.78	1.6	1.7
Polysulfone (Full)	1.99	4.0	5.6
PMMA (Day)	0.57	6.5	6.6
PMMA (Night)	0.58	6.6	4.7
PMMA (Full)	1.11	12.6	12.3
Polystyrene (Day)	0.36	4.6	4.5
Polystyrene (Night)	0.27	3.5	3.4
Polystyrene (Full)	0.57	7.3	7.4

\* Kapton erosion profilometry data provided by S. Koontz (NASA/JSC).

EOIM-3 state-of-health telemetry, provided by NASA/JSC, was analyzed to determine the dwell time for the occulting baffle in the day and night positions. The baffle was in the day position for 86,877 seconds (s) in the "day" position and 59,862 s in the "night" position. The day samples were exposed to ram atomic oxygen for 59 percent of the full-exposure duration whereas the night samples were exposed 41 percent of the time. An estimate of AO fluences, based on the MSIS-86 derived average daytime flux of  $1.7 \times 10^{15}$  AO/cm<sup>2</sup>-s and nighttime flux of  $1.5 \times 10^{15}$  AO/cm<sup>2</sup> leads to a daytime fluence of  $1.5 \times 10^{20}$  AO/cm<sup>2</sup>-s and a nighttime fluence of  $9.1 \times 10^{19}$  AO/cm<sup>2</sup>. The daytime specimens were exposed to 1.64 times the AO fluence experienced by the nighttime specimens.

The effect of solar UV radiation upon AO reactivity may be examined by comparison of the erosion depths of the day and night specimens. Table 4-4 presents relative erosion of the day and night specimens compared to the day and night AO fluence ratio. Examination of the erosion ratios indicates that Kapton erosion tracks the relative AO fluences exactly. This implies that the atomic oxygen erosion efficiency for Kapton is independent of solar irradiation. Polysulfone appears to erode much more efficiently in the daytime phase than at night. In contrast to this enhanced daytime reactivity, PMMA and polystyrene appear to erode less efficiently in the daytime portion of the orbit than at night.

Table 4-4. Comparison of day and night erosion of EOIM-3 solar UV specimens

Material	Day/Full Exposure Erosion Ratio	Night/Full Exposure Erosion Ratio	Day/Night Erosion Ratio
Kapton	0.62	0.38	1.63
Polysulfone	0.71	0.30	2.4
PMMA	0.53	0.38	1.4
Polystyrene	0.61	0.46	1.3
AO Fluence	0.62	0.38	1.64

It is also interesting to compare the erosion efficiencies (depth/fluence) for the day, night and full exposure specimens with data obtained for materials exposed aboard the Long Duration Exposure Facility [7,8] and previous shuttle flights (STS-8). Table 4-5 summarizes these data. Note that the erosion efficiencies of PMMA and polystyrene are about 25% higher for the LDEF exposure than for EOIM-3. Since LDEF materials receive approximately 400 times the amount of solar radiation as experienced on EOIM-3, the enhanced erosion rate is not unexpected. It should be noted that the surfaces of the test materials are also subjected to charged particle radiation consisting of electrons and protons. Although the dose is anticipated to be small, recently laboratory evidence indicated a significant synergistic effect of atomic oxygen and electron radiation for Kapton.

Table 4-5. Comparison of EOIM solar UV erosion efficiencies with LDEF results.

Material or Environment Parameter	EOIM-3 Reaction Efficiency (R.E.) ( $\times 10^{-24}$ cm <sup>3</sup> /atom)			Previous R.E. ( $\times 10^{-24}$ cm <sup>3</sup> /atom)	
	Day	Night	Full	STS-8	LDEF
Kapton (JSC)	3.38	3.38	3.38	3.0	2.89
Polysulfone	2.68	1.87	2.33	2.4	2.3
PMMA	4.43	5.16	5.12	4.91	6.3
Polystyrene	3.02	3.73	3.08	1.8*	4.17
AO Fluence ( $\times 10^{20}$ )	1.49	0.91	2.4	3.5	90.
Equiv. Solar Hours	< 10	0	25	< 25	> 10,000

\* This specimen showed a significant phosphate content in ESCA, possibly reducing erosion.

The ESCA data for the Solar UV specimens are provided in Appendix C. The extent of surface oxidation of the nighttime samples appeared to be slightly greater than that of the daytime specimens. It is interesting to note that silicon contamination appears predominately on the nighttime specimens, while the daytime specimens were free of silicon. It does not appear to be an obvious trend for surface oxidation as compared to relative day/night reactivities for these materials.

The molecular weight distributions for control, day, night, and full-exposure specimens were obtained for the solar UV specimens using HPLC. The measured molecular weight distributions are provided in Figures 4-19 through 4-21. The weight and number average molecular weight data are summarized in Table 4-6. The polysulfone and PMMA specimens show significant decreases in average molecular weights for the full-exposure specimens referenced to the control molecular weights. This is indicative of chain scission processes occurring in the bulk of the polymer. Polystyrene, though, shows a small but consistent increase in molecular weight. Examination of the HPLC trace for the polystyrenes (Figure 4-21) reveals a new molecular weight population near  $M_w = 445,000$ . This feature is indicative of the formation of cross-links between the polystyrene

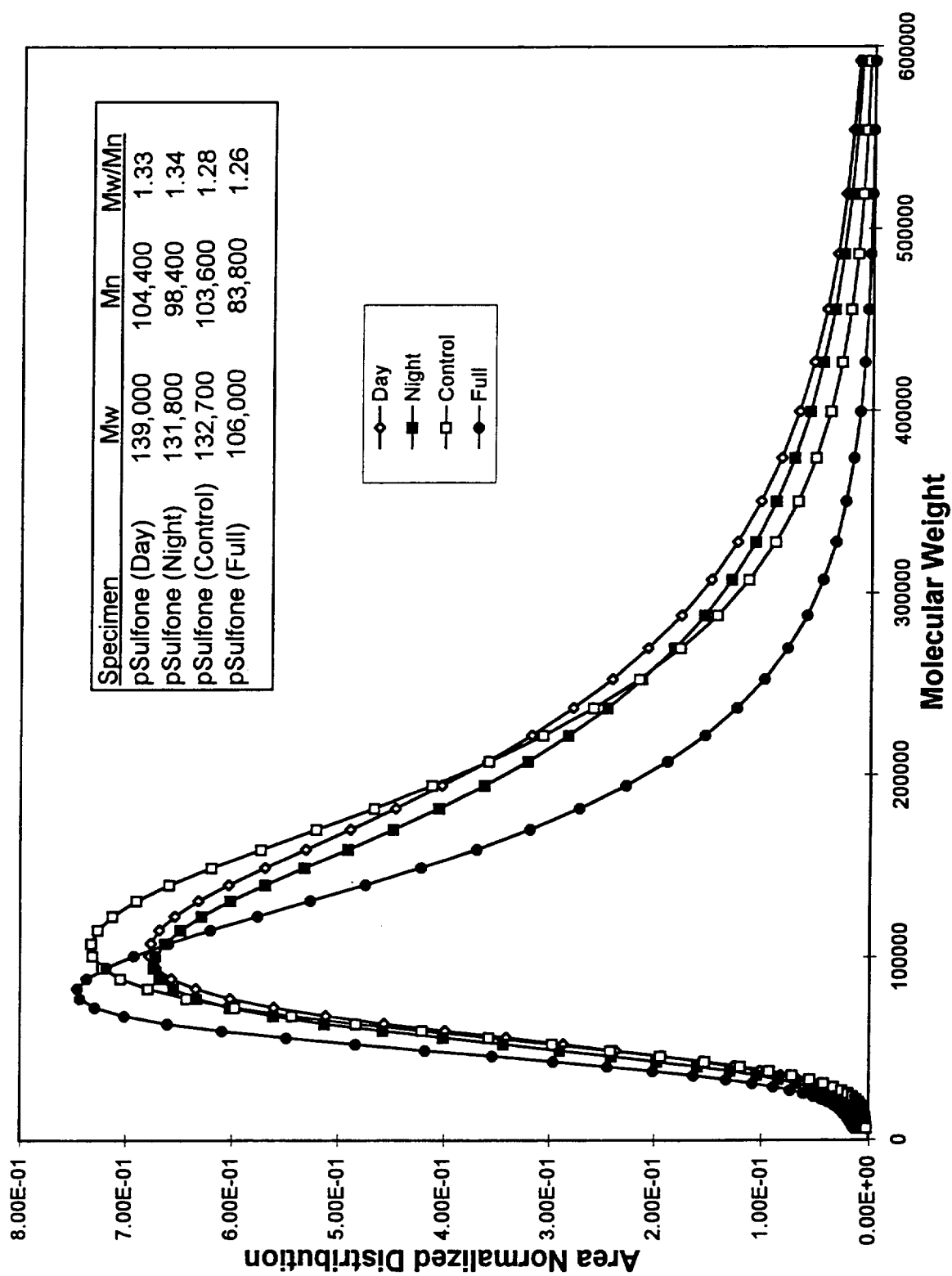


Figure 4-19. HPLC traces for SUV1: polysulfone.

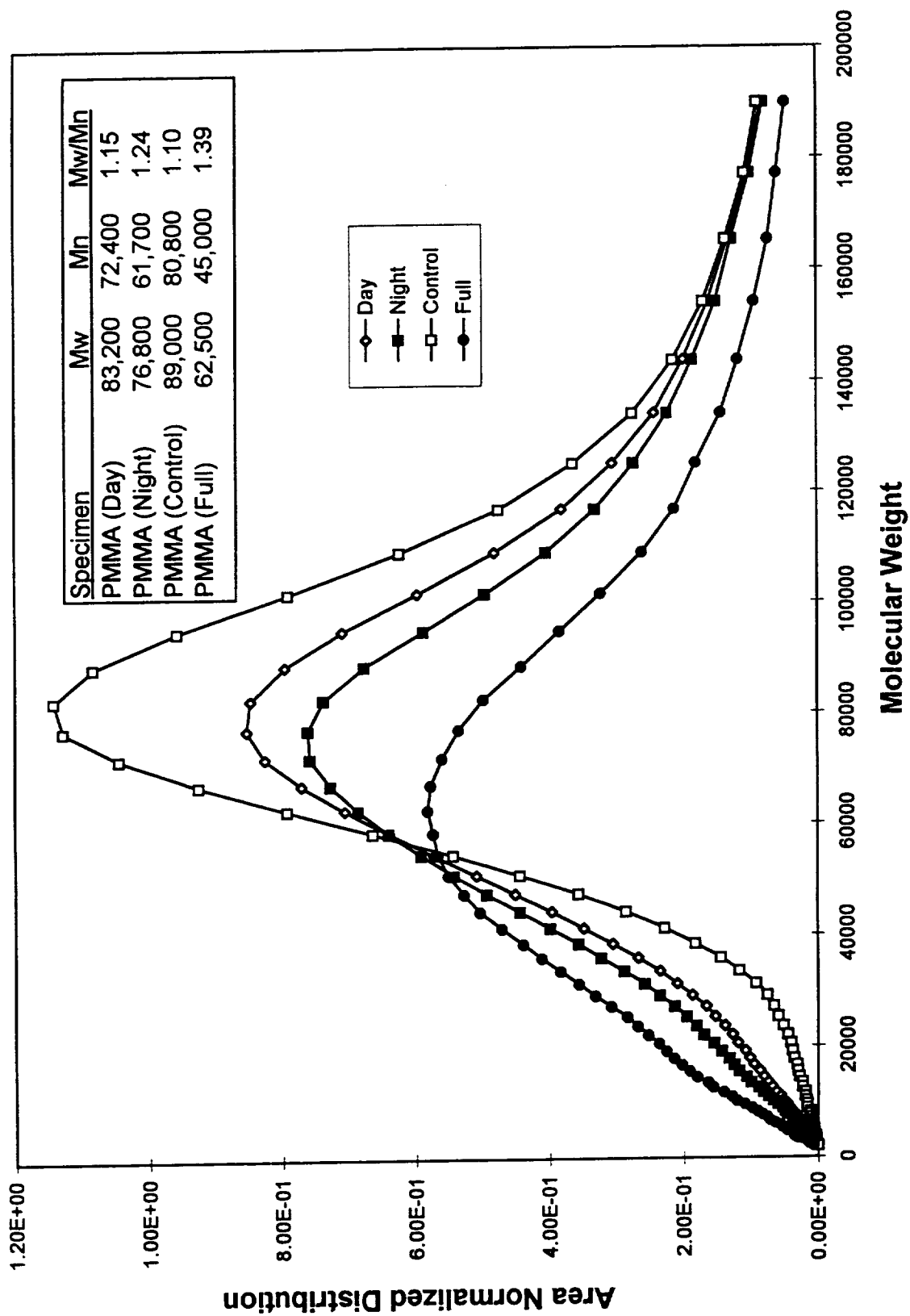


Figure 4-20. HPLC traces for SUV2: PMMA.

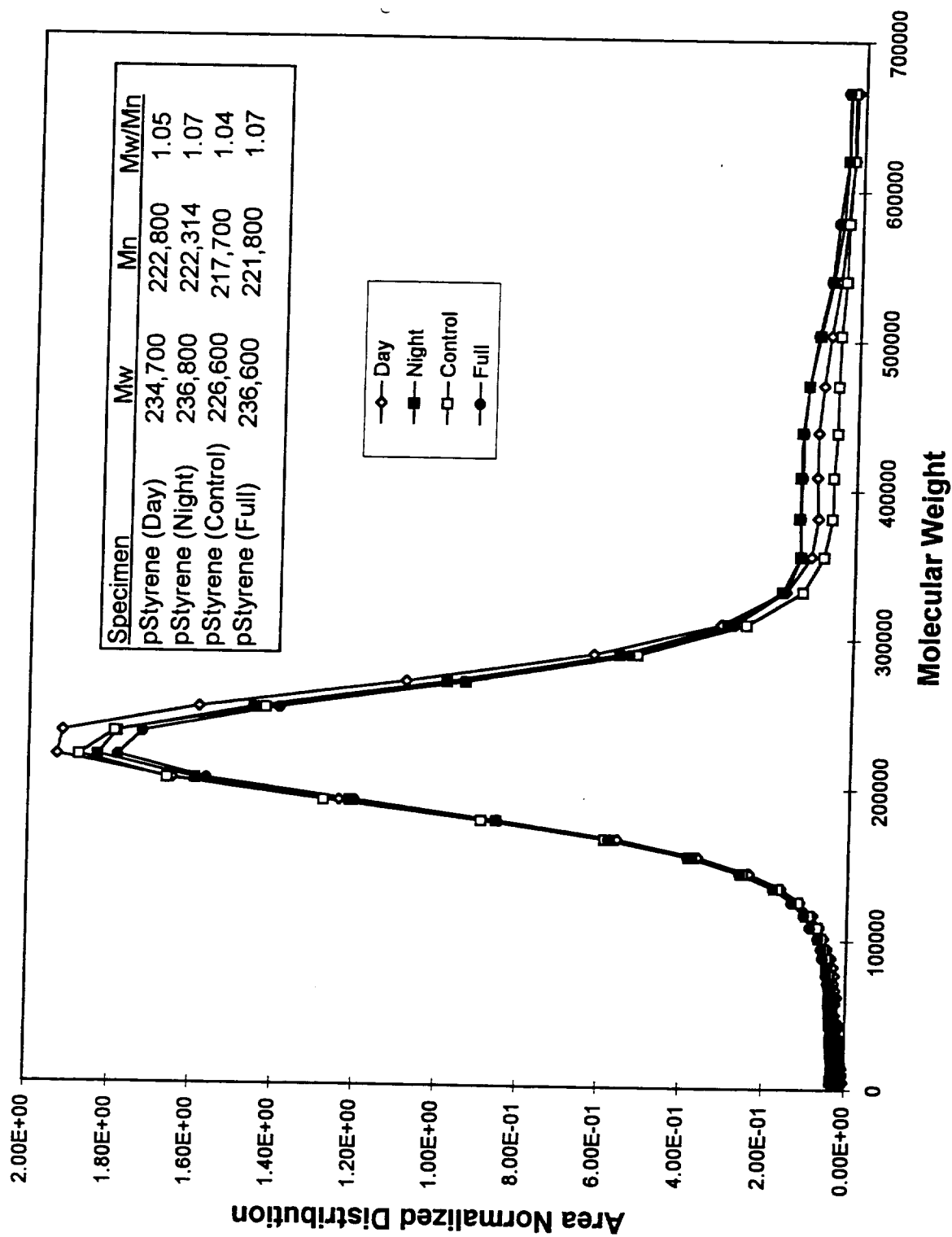


Figure 4-21. HPLC traces for SUV4: polystyrene.

polymer chains. The exposed polysulfone specimens were cross-linked significantly, as insoluble (gel) mass fractions of about 0.06 were found for each of the polysulfone solar UV specimens. A comparison of these data with LDEF results [7] shows consistent chain scission behavior for PMMA and cross-linking processes for polystyrene and polysulfone. A more complete mechanistic interpretation of the erosion and molecular weight data is still evolving for these materials.

Table 4-6. Molecular weight distributions for EOIM-3 solar UV specimens

Specimen	$M_w$	$M_n$	$M_w/M_n$
Polysulfone (Day)	139,000	104,400	1.33
Polysulfone (Night)	131,800	98,400	1.34
Polysulfone (Full)	106,000	83,800	1.26
Polysulfone (Control)	132,700	103,600	1.28
PMMA (Day)	83,200	72,400	1.15
PMMA (Night)	76,800	61,700	1.24
PMMA (Full)	62,500	45,000	1.39
PMMA (Control)	89,000	80,800	1.10
Polystyrene (Day)	234,700	222,800	1.05
Polystyrene (Night)	236,800	222,314	1.07
Polystyrene (Full)	236,600	221,800	1.07
Polystyrene (Control)	226,600	217,700	1.04

#### 4.5 Variable Exposure Samples

The occulting baffle for the variable exposure experiment did not sequentially expose the four sets of specimens to increasing levels of atomic oxygen fluence. Rather, the baffle moved to the full open position shortly after activation. Therefore, only one of each of the variable exposure specimens was examined for changes relative to the control articles. ESCA data, listed in Appendix C, shows that the exposed boron nitride on silicon specimen was oxidized. Atomic oxygen is able to replace the nitrogen in boron nitride, forming boron oxide. Boron oxide is highly hygroscopic,



and readily forms boric acid upon exposure to the terrestrial atmosphere. The boric acid residue does not remain on the surface, due to its volatility. Hence the nitrogen to oxygen ratio measured by ESCA tends to be skewed in favor of nitrogen.

The specimens of highly-oriented pyrolytic graphite (HOPG) were returned to the University of California at Los Angeles for atomic force microscopy measurements. The results of this study have been published [9], but a brief summary of the findings is provided here. The exposed HOPG specimen was eroded by atomic oxygen to a depth of  $2.25 \pm 0.10 \mu\text{m}$  (approximately 6400 monolayers of graphite). The surface roughness was about 85 nm (approximately 240 monolayers of graphite). The observed roughness is a factor of three greater than what would be predicted by a strictly stochastic erosion model. A stochastic erosion model assumes shot noise to be the dominant term in establishing the surface roughness. The expected roughness for this model would be approximated by the square root of the number of monolayers eroded (80 monolayers or about 30 nm). Surface diffusion of oxygen to edges or defects is proposed as a plausible mechanism for development of the rougher than expected surfaces.

#### **4.6 AO/Kapton Scattering Results**

Scattering product data for the  $^{13}\text{C}$ -enriched Kapton interaction with atomic oxygen were obtained by the EOIM-3 mass spectrometer and in the laboratory are discussed in the following sections. Additional information obtained from the laboratory time-of-flight data is used to develop a detailed physical picture of atomic oxygen reacting with a model polymer.

##### **4.6.1 EOIM-3 Mass Spectra**

Figure 4-22 shows representative mass spectra taken with the mass spectrometer viewing the  $^{13}\text{C}$ -enriched Kapton sample when the cover was off and when the cover was on. These data indicate that the net mass spectrum for direct reaction of O atoms with  $^{13}\text{C}$ -enriched Kapton can not be obtained simply by subtracting the cover-on from the cover-off spectrum. Even when the cover is on, a small peak from  $^{13}\text{CO}_2$  can be seen; therefore, scattered O atoms must be reacting with the sample. If the cover was off, some of these reactions might not occur. Without substantial modeling of O-atom inelastic scattering from various surfaces on the EOIM-3 tray, it is difficult to know exactly how to represent the space data. The true mass spectrum for direct O-atom attack

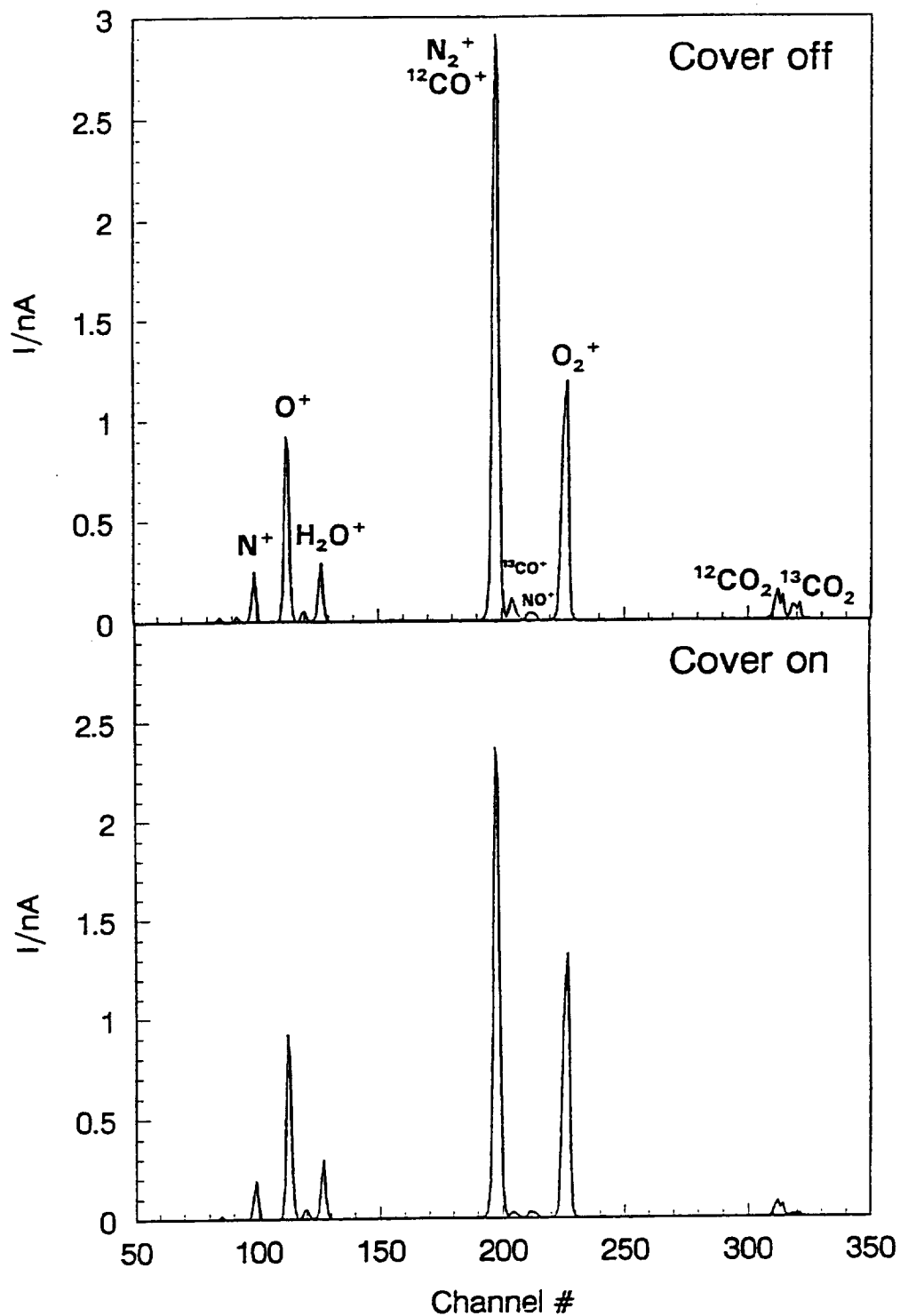


Figure 4-22. Mass spectra taken with EOIM-3 mass spectrometer viewing  $^{13}C$ -enriched Kapton on the carousel.

probably lies somewhere between the cover-off spectrum and the spectrum that is the difference of cover on and cover off.

#### 4.6.2 *Laboratory Mass Spectra*

The hyperthermal oxygen beam, described in Section 3.9, was directed at Kapton and  $^{13}\text{C}$ -enriched Kapton surfaces, and scattered products were monitored with the mass spectrometer detector. The angle of incidence was  $45^\circ$  with respect to the surface normal, and the detector axis was also  $45^\circ$ . Thus, the total included scattering angle was  $90^\circ$ , similar to the EOIM-3 carousel experiment. The beam pulse provided the timing for the experiment; no additional chopping was used. TOF distributions of scattered products were collected at  $m/z = 16(\text{O}^+)$ ,  $18(\text{H}_2\text{O}^+)$ ,  $28(^{12}\text{CO}^+)$ ,  $29(^{13}\text{CO}^+)$ ,  $30(\text{NO}^+)$ ,  $32(\text{O}_2^+)$ ,  $44(^{12}\text{CO}_2)$ , and  $45(^{13}\text{CO}_2)$ . Typical accumulation times for each TOF distribution were 1200 beam pulses. The time resolution was limited by our multichannel scaler to  $2\ \mu\text{s}/\text{channel}$ . All data were collected before a total O-atom fluence of  $2 \times 10^{18}\ \text{atoms}/\text{cm}^2$  was accumulated on either surface, so the familiar "shag-carpet" morphology was not fully developed.

#### 4.6.3 *Inelastic Scattering of Oxygen*

TOF distributions for O and  $\text{O}_2$  scattering from the  $^{13}\text{C}$ -enriched surface are shown in Figure 4-23. Time zero in these distributions corresponds to the firing of the laser, so the observed arrival time includes the flight times of the beam pulse to the surface and scattered products from the surface to the detector. For reference, the respective beam TOF distributions are shown (dashed lines) to illustrate the slowing of the impinging species as a result of energy transfer at the surface. While the O-atom distribution is the result of inelastic scattering from the surface, the  $\text{O}_2$  TOF distribution may have an additional contribution from O-atom recombination at the surface. It is difficult to quantify the amount of O-atom recombination without a careful study of the distributions of the scattered molecular and atomic oxygen as a function of exit angle. Nevertheless, the  $\text{O}_2$  (and O) exhibits a behavior that is typical for inelastic scattering of energetic species from a surface [10–14].

Regardless of whether O-atoms or  $\text{O}_2$  molecules scatter from the surface, we see two components in the TOF distribution—a hyperthermal and roughly thermal component. These two

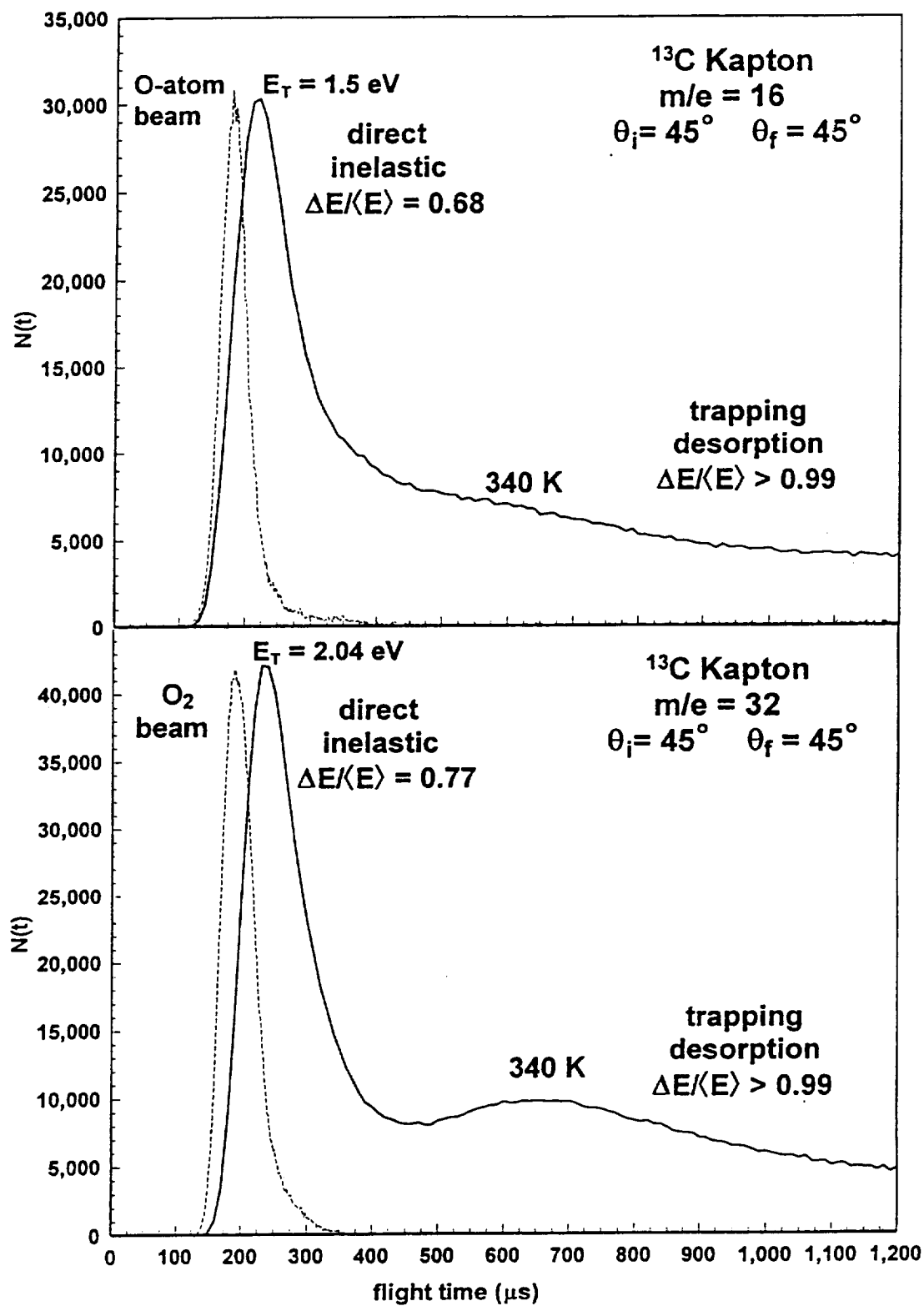


Figure 4-23. Time-of-flight distributions of O and  $\text{O}_2$  scattered from a  $^{13}\text{C}$ -enriched Kapton surface.

components can be understood in terms of two limiting cases of inelastic scattering [10–14]. The first is direct inelastic scattering, where an incoming atom or molecule bounces off the surface after a single collision. In this case, the interaction is too fast to allow for thermal equilibration with the surface and only a fraction of the initial kinetic energy is lost to the surface. The second case is trapping desorption, where the incoming atom or molecule becomes trapped long enough to come into thermal equilibrium with the surface and later desorbs at thermal energies.

Both TOF distributions show a large direct inelastic component, demonstrating clearly that much of the initial energy is not accommodated on the surface. In these particular TOF distributions, the trapping desorption component appears to be enhanced relative to the direct inelastic component because: (1) there is an untrue enhancement of the signal at long times due to inelastic scattering of thermalized O atoms and O<sub>2</sub> molecules that effuse out of the source chamber through the skimmer, and (2) species traveling more slowly through the ionizer have a greater probability of being ionized than faster species (the flux  $I(t)$  is proportional to  $N(t)/t$ ). Therefore, we estimate that the trapping desorption component is less than 20 percent for both O and O<sub>2</sub> inelastic scattering. It is important to note that the relative fraction of trapping desorption may vary considerably depending on the initial and final scattering angles [14].

The average fractional energy transfer for direct inelastic scattering is also dependent on the initial and final scattering angles. Surface roughness may reduce the fraction of direct inelastic scattering; however, we have observed large direct inelastic scattering components in our laboratory even when O-atoms scatter from the very rough surface of a graphite polysulfone composite material. Finally, for comparison, we note that an earlier surface energy accommodation study [15] with roughly 5-eV O atoms impinging on metal and glass surfaces implied a significant amount of direct inelastic scattering with the reported energy accommodation coefficients of approximately  $0.6 \pm 50$  percent.

#### 4.6.4 Reactive Scattering of Fast Oxygen and Kapton

Figure 4-24 shows TOF distributions of carbon dioxide products emerging from the surfaces of Kapton HN and <sup>13</sup>C-enriched Kapton after being struck by the hyperthermal beam pulse. Again, time zero corresponds to the firing of the laser. On the left is signal from Kapton HN and, on the

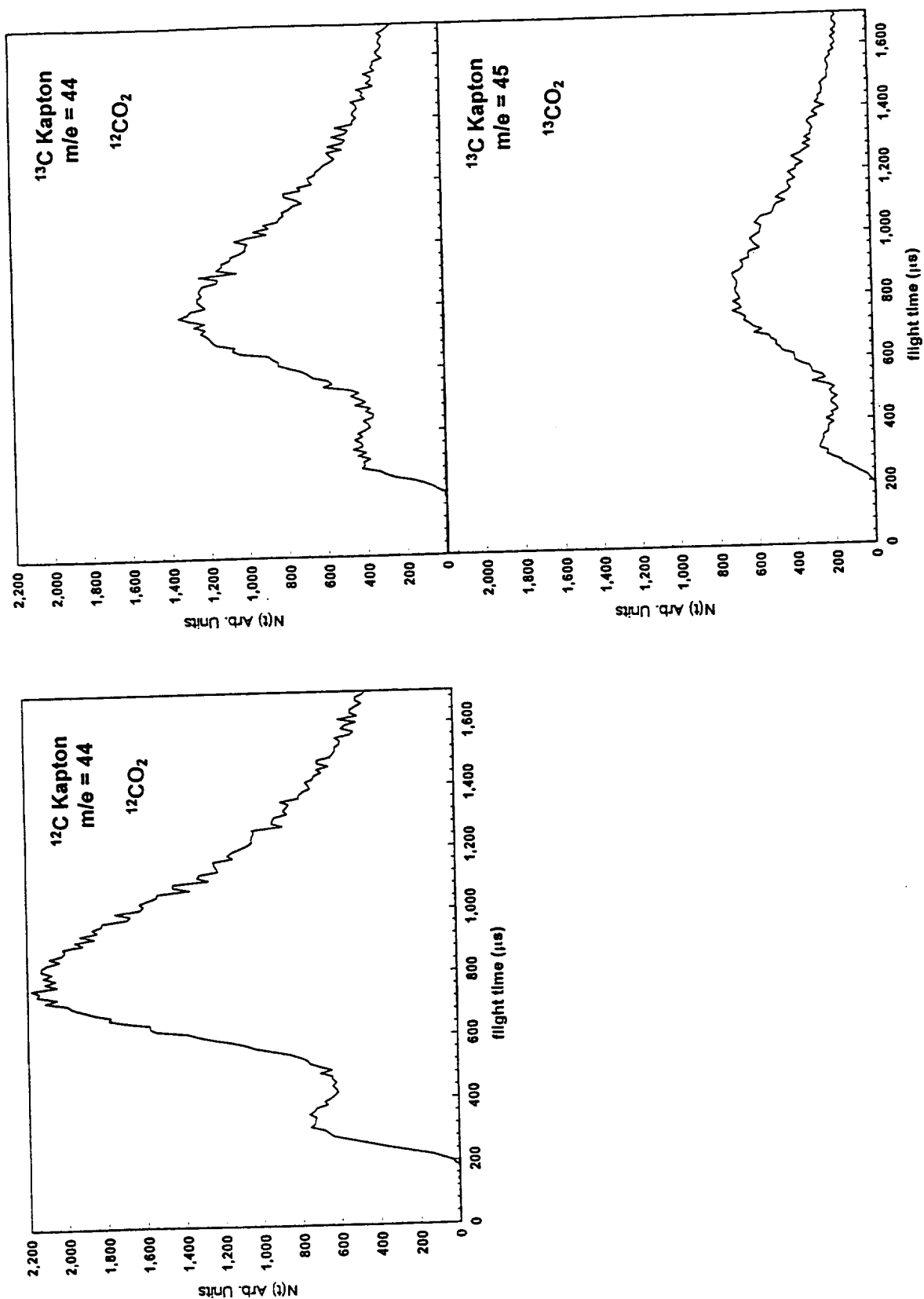


Figure 4-24. Time-of-flight distributions of CO<sub>2</sub> products emerging from Kapton HN (<sup>12</sup>C Kapton) and <sup>13</sup>C-enriched Kapton surfaces.

right, from  $^{13}\text{C}$ -enriched Kapton. As can be seen, the  $^{12}\text{CO}_2$  signal from plain Kapton is distributed between  $^{12}\text{CO}_2$  and  $^{13}\text{CO}_2$  when the reaction occurs with  $^{13}\text{C}$ -enriched Kapton. The fact that the sum of the signals at the two isotopes from  $^{13}\text{C}$ -enriched Kapton add up to the signal at the one isotope from plain Kapton HN indicates that the signals must originate from reactions with the actual sample materials and not contamination on them.

Two key observations stand out in the carbon dioxide TOF distributions. First, the  $^{12}\text{CO}_2$  signal from  $^{13}\text{C}$ -enriched Kapton is higher than the  $^{13}\text{CO}_2$  signal, even though there are more C-13 carbons in the polymer chain. This observation suggests that volatile  $\text{CO}_2$  is coming preferentially from reactions with the imide component of the polymer repeat unit. Second, there are two components in the TOF distributions. It is clear from the bimodal distributions that two kinds of interactions lead to  $\text{CO}_2$  products. The faster signal corresponds to products that are ejected from the surface at hyperthermal energies ( $\sim 0.7$  eV), and the slower signal corresponds to reaction products that leave the surface at velocities given by the surface temperature. The fast products may come from a direct reaction—such as the Eley-Rideal mechanism [16]—on the surface with carbonyl groups that are part of the polyimide polymer or that accumulate on the surface during O-atom bombardment, or perhaps  $\text{CO}_2$  residing on the surface is knocked off by collision-induced desorption. The slow products, on the other hand, are probably the result of a surface reaction that follows initial adsorption of the impinging O atoms on the surface, e.g. the Langmuir-Hinshelwood mechanism [16].

We see an analogous behavior for the CO reactive products (Fig. 4-25). The signal is generally lower, and the relative magnitude of the hyperthermal component is larger.

Figure 4-26 shows TOF distributions collected at two other product masses, corresponding to  $\text{H}_2\text{O}$  and  $\text{NO}$ . As expected, there is not much difference between the two forms of Kapton at these unlabeled masses. The shape of the  $\text{NO}^+$  TOF distribution is uncertain because the raw data contained a relatively large contribution from inelastic scattering of  $\text{O}_2$ , which could still be detected at  $m/z = 30$  with the mass spectrometer resolution employed. We therefore estimated the contribution from  $\text{O}_2$  to the  $m/z = 30$  TOF distribution and subtracted it to arrive at the distribution shown in Fig. 4-26.

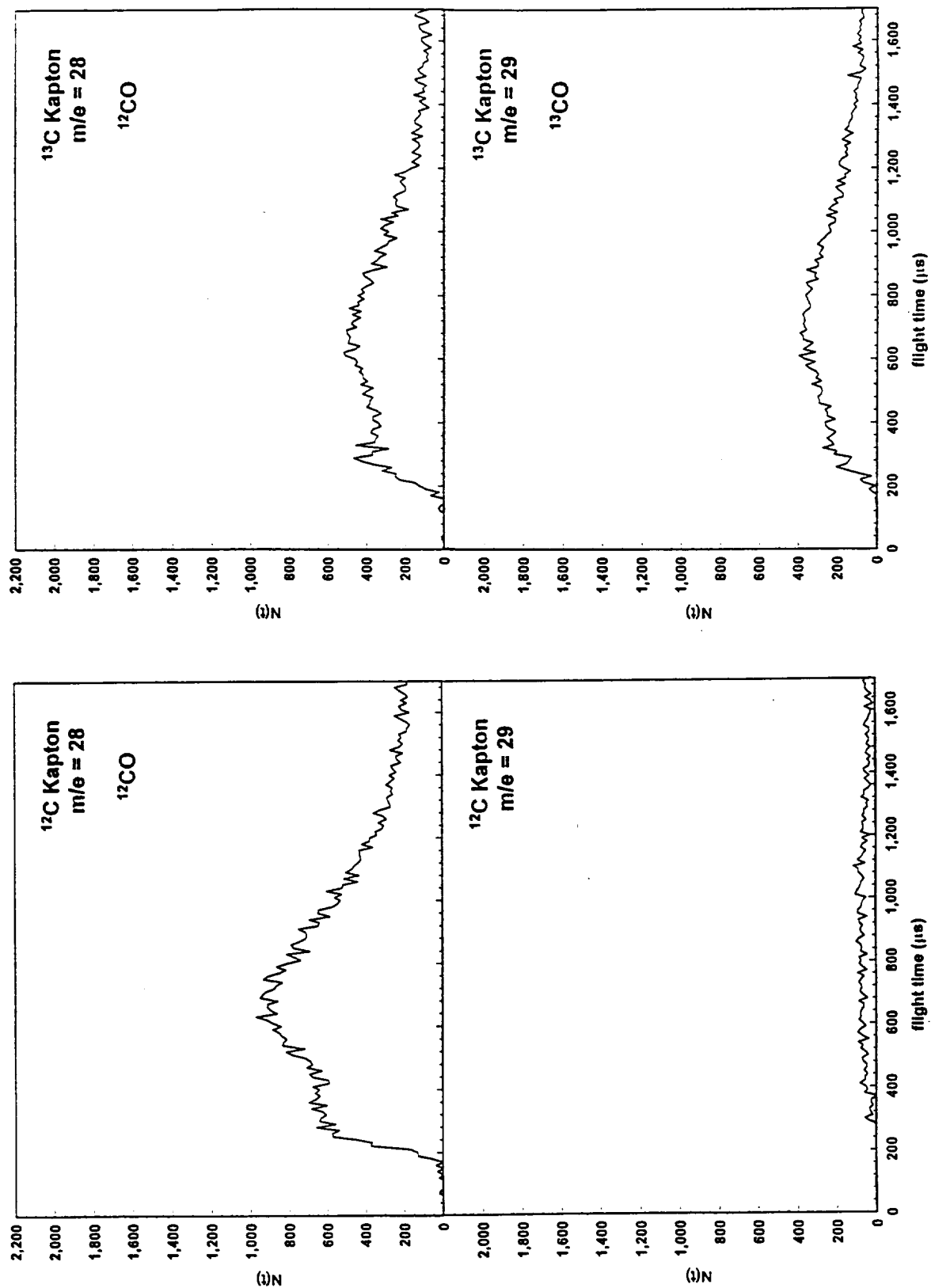


Figure 4-25. Time-of-flight distributions of CO products emerging from Kapton HN ( $^{12}\text{C}$  Kapton) and  $^{13}\text{C}$ -enriched Kapton surfaces.



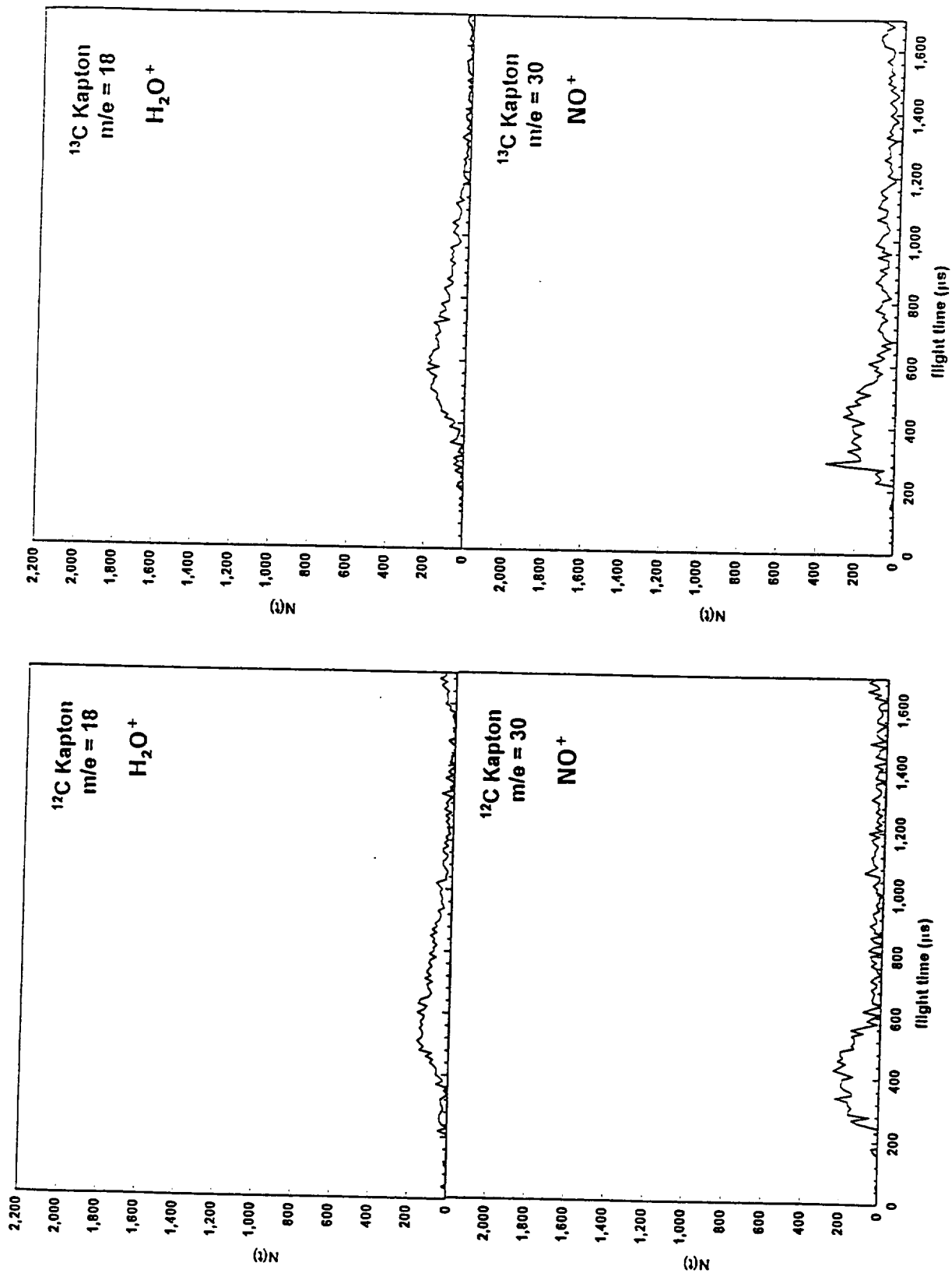


Figure 4-26. Time-of-flight distributions of  $\text{H}_2\text{O}$  and  $\text{NO}$  products emerging from Kapton HN ( $^{12}\text{C}$  Kapton) and  $^{13}\text{C}$ -enriched Kapton surfaces.

These preliminary data show some interesting features that suggest preferential attack at the imide group in the polymer and two types of interaction mechanisms with the surface, giving rise to thermal and hyperthermal products. A complete understanding of these data will require a detailed study of the TOF distributions at many masses as a function of incident angle, final angle, surface temperature, incident energy, and incident species. For example, the hyperthermal, or direct-reaction, signal may depend strongly on incident energy and exit angle and only weakly on surface temperature, whereas the thermal, or indirect-reaction, signal may have a cosine angular distribution regardless of incident kinetic energy, and only a change in surface temperature would affect arrival time.

The observation of more CO and CO<sub>2</sub> products from reaction with the imide component of the polymer raises questions about the fate of the ether component. It appears from our data that the ether component may degrade partly through release of volatile species other than CO or CO<sub>2</sub>. If these volatile species are higher-molecular-weight hydrocarbon fragments, then they could pose a contamination threat on a spacecraft. Future experiments should include a careful search over a wide mass range in order to identify any heavier volatile products that might be evaporating from the surface.

#### 4.6.5 Comparison of Lab and Space Results

The laboratory TOF distributions can be integrated to arrive at a mass spectrum that can be compared with the EOIM-3 carousel mass spectrum from <sup>13</sup>C-enriched Kapton. Figure 4-27 shows two representations of the flight data with the laboratory mass spectrum in the middle. There are four peaks in the flight mass spectrum that can be compared with our laboratory mass spectrum of reactive products:  $m/z = 29(^{13}\text{CO}^+)$ ,  $30(\text{NO}^+)$ ,  $44(^{12}\text{CO}_2^+)$ , and  $45(^{13}\text{CO}_2^+)$ . The water peak ( $m/z = 18$ ) is too large and variable in the flight data to be meaningful, and the  $m/z = 28$  peak in the flight data is dominated by N<sub>2</sub>, which is in the ambient LEO environment.

The lab data show more <sup>12</sup>CO<sub>2</sub> than <sup>13</sup>CO<sub>2</sub>, and the same may be true of the space data. The main difference between the lab and flight data is the relatively high ratio of <sup>13</sup>CO<sub>2</sub> to <sup>13</sup>CO products in the lab as compared with space. The apparently high CO<sub>2</sub> signal in the lab might arise from the high O<sub>2</sub> component in the hyperthermal beam (the fraction of O<sub>2</sub> in the EOIM-3 environment is <5

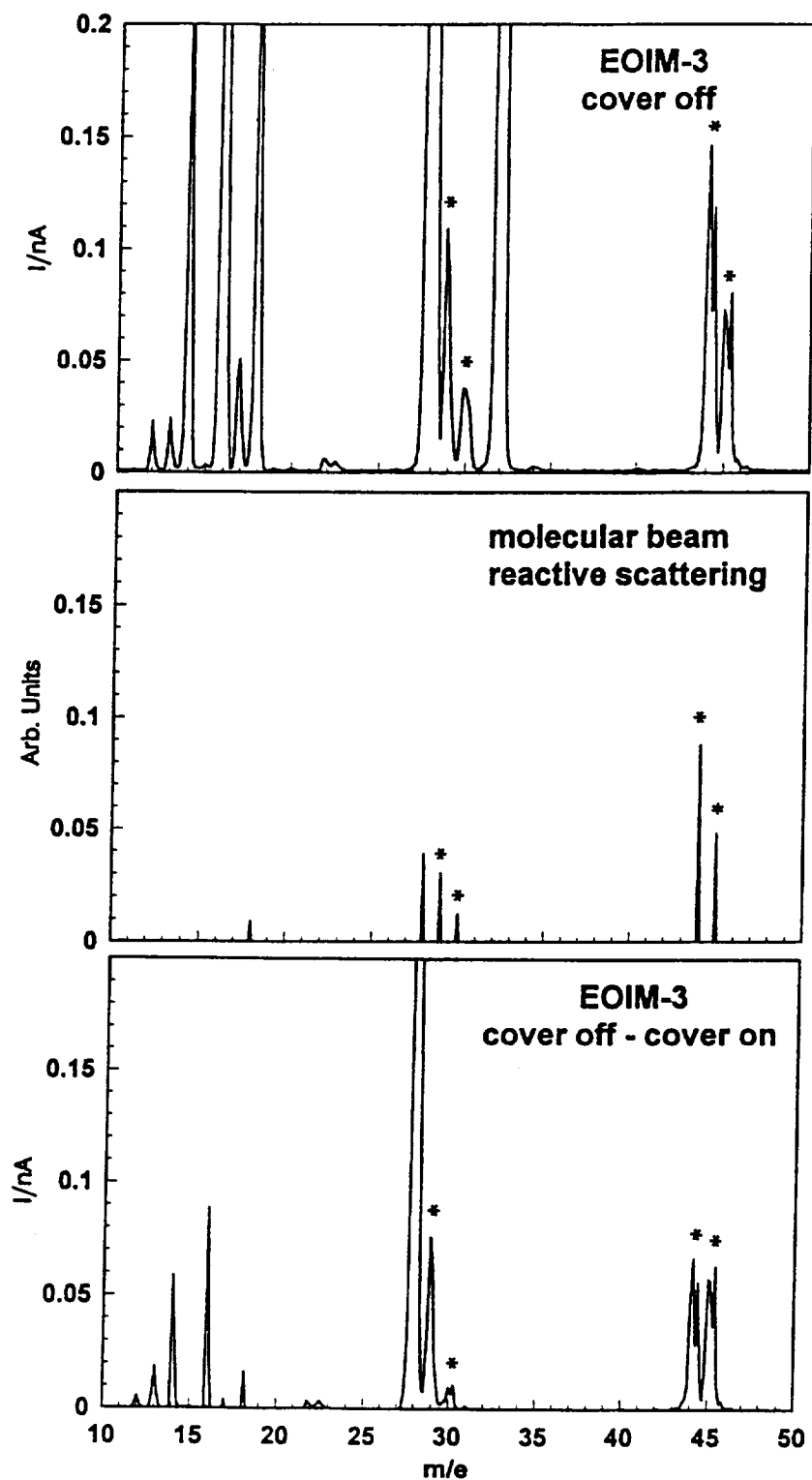


Figure 4-27. Comparison of mass spectra collected in space (top and bottom panels) and in the laboratory (center panel).

percent). Perhaps  $O_2$  adds to radical sites on the surface and/or dissociates on impact, leading to O-atom reactions on the surface. In either case, the level of surface oxidation would increase and thus favor the more highly oxidized form of carbon, i.e.,  $CO_2$ .

Although the lab and flight results are preliminary, they do appear similar. Further laboratory studies with a beam much reduced in molecular oxygen may show even better agreement with the space data. It is important to have a common point of agreement between the lab and flight experiments in order to lend credence to the laboratory experiments as representative of the interactions that take place in LEO. Our laboratory experiment is much more sophisticated than the EOIM-3 carousel experiment and can therefore reveal much more about the interaction mechanisms of hyperthermal O atoms with Kapton (or any other material); however, the value of these and future lab results to the space environment and effects community will ultimately be judged by their "calibration" with space experiments.

## 5.0 Summary and Conclusions

Test materials were successfully integrated into several sub-experiment configurations aboard the EOIM-3 platform and exposed to atomic oxygen in low Earth orbit. Specimens were integrated into ram-facing passive trays to investigate the absolute erosion rate, oxidation, and morphological changes. Materials were integrated into heated fixtures to determine the temperature dependence of the AO degradation processes. A device was developed in order to determine the effects of AO scattered from various target materials on Kapton. Pre and postflight data were collected on all the samples, including photography, AFM and SEM microscopy, HPLC, and ESCA surface analysis. On-orbit mass spectrometry of reaction products from  $^{13}\text{C}$ -enriched Kapton was performed.

The JPL EOIM-3 experiment provided new insight into atomic oxygen interactions with materials. The fluorinated polystyrene experiment demonstrated the vulnerability of the main chain "backbone" of polymers. The solar UV experiment provided interesting and yet to be explained enhanced AO reactivity and bulk processes (cross-linking or chain scission) of polystyrene and PMMA in the *night* phase. Temperature effects on the thickness of the oxide layer of germanium were observed and explained via a surface disproportionation mechanism. The mass spectrometry measurements on-orbit and in the laboratory provided very fundamental data regarding reaction products and scattering dynamics for atomic oxygen reacting with a polymer. Scattering experiments on-board EOIM-3 revealed evidence for oxidation and minor erosion of Kapton by atomic oxygen scattered from several surfaces. The EOIM-3 experiment and correlative ground studies have provided valuable data for elucidation of interaction mechanisms of atomic oxygen with materials in the space environment.

Some very useful engineering data were also obtained in the JPL EOIM-3 experiment. The use of thin film coatings for APSA was validated, with excellent performance witnessed in Ge-coated Kapton. The stability of light scattering properties of Spectrolon, including carbon-loaded low reflectance Spectrolon was demonstrated in this experiment. The effects of atomic oxygen on the thermo-optical properties of carbon/carbon composites (at elevated temperatures) and advanced white paints were determined on EOIM-3. The effectiveness of siloxane modification for protection against AO attack of a commercial polycyanate resin was also demonstrated.

## 6.0 Acknowledgements

The authors acknowledge Drs. Lubert J. Leger, Steven Koontz, and Mr. James Visentine of the NASA Johnson Space Center for providing space on the Evaluation of Oxygen Interactions with Materials Experiment-3 (EOIM-3) platform. The authors acknowledge James Soldi for his invaluable assistance and support throughout the project, and Teresa Moore for her exceptional contribution in the molecular beam scattering of the  $^{13}\text{C}$ -enriched Kapton experiment. Andre Yavrouian synthesized the  $^{13}\text{C}$ -enriched Kapton, the fluorinated polystyrene series, and provided valuable insight regarding polymer chemistry aspects of these experiments. Dr. Daniel Coulter provided helpful discussions in the analysis of molecular weight distributions of the solar UV polymers.

## 7.0 References

1. Minton, T. K., *Protocol for Atomic Oxygen Testing of Materials in Ground-Based Facilities*; Version Number 1, JPL Publication 94-02, April 1, 1994.
2. Chung, S. Y., Brinza, D. E., Minton, T. K., Stiegman, A. E., Kenny, J. T., and Liang, R. H., *Flight- and Ground-Test Correlation Study of BMDO SDS Materials*, Phase I Report, JPL Publication 93-31, December 1993.
3. Lee, Y. T., McDonald, J. D., LeBreton, P. R., and Herschbach, D. R., "Molecular Beam Reactive Scattering Apparatus with Electron Bombardment Detector," *Rev. Sci. Instrum.* **40**, 1402 (1969).
4. Brinza, D. E., Coulter, D. R., Chung, S. Y., Smith, K. O., Moacanin, J., and Liang, R.H., *A Facility for Studies of Atomic Oxygen Interactions with Materials*, *Proceedings of the 3rd International SAMPE Electronics Conference*, p. 646 (1989).
5. Caledonia, G. E., Krech, R. H., and Green, B. D., "A High Flux Source of Energetic Oxygen Atoms for Material Degradation Studies," *ALAA J.* **25**, 59 (1987).
6. Proch, D. and Trickl, T., "A High-Intensity Multi-Purpose Piezoelectric Pulsed Molecular Beam Source," *Rev. Sci. Instrum.* **60**, 713 (1989).
7. Gregory, J.C., "On the Linearity of Fast Atomic Oxygen Effects," *NASA Conference Publication CP-3257*, 193 (1994).
8. Young, P.R., Slempe, W.S., and Stein, B.A., "Performance of Selected Polymeric Materials on LDEF," *NASA Conference Publication CP-3257*, 125 (1994).
9. Ngo, T., Snyder, E.J., Tong, W.M., Williams, R.S., and Anderson, M.S., "O atom etching of graphite in low earth orbit," *Surf. Science*, **314**, L817-L822 (1994).
10. Rettner, C. T. and Ashfold, M. N. R., *Dynamics of Gas-Surface Interactions, Advances in Gas-Phase Photochemistry and Kinetics Series*, (Royal Society of Chemistry, Cambridge, 1991).
11. Rettner, C. T., Schweizer, E. K., and Mullins, C. B., "Desorption and Trapping of Argon at a 2H-W(100) Surface and a Test of the Applicability of Detailed Balance to a Nonequilibrium System," *J. Chem. Phys.* **90**, 3800 (1989).
12. Rettner, C. T., Barker, J. A., and Bethune, D. S., "Angular and Velocity Distribution Characteristic of the Transition between the Thermal and Structure Regimes of Gas-Surface Scattering," *Phys. Rev. Lett.* **67**, 2183 (1991).

13. Saecker, M. E., Govoni, S. T., Kowalski, D. V., King, M. E., and Nathanson, G. M., "Molecular Beam Scattering from Liquid Surfaces," *Science* **252**, 1421 (1991).
14. King, M. E., Nathanson, G. M., Hanning-Lee, M. A., and Minton, T. K., "Probing the Microscopic Corrugation of Liquid Surfaces with Gas-Liquid Collisions," *Phys. Rev. Lett.* **70**, 1026 (1993).
15. Krech, R. H., Gauthier, M. J., and Caledonia, G. E., "High Velocity Atomic Oxygen/Surface Accommodation Studies," *J. Spacecraft and Rockets* **30**, 509 (1993).
16. Atkins, P. W., *Physical Chemistry* (Freeman, New York, 1986) 3rd ed., pp. 782-3.



**Appendix A**  
**Tables of Materials List**

Table 1. Passive Tray Samples

Sample Code	Material	Tray	Size
M1	Amorphous teflon 1600	MSFC	2.54 cm
M2	Amorphous teflon 2400	MSFC	2.54 cm
M6	Polystyrene	MSFC	2.54 cm
M7	Backbone-fluorinated polystyrene	MSFC	2.54 cm
M8	Ring-fluorinated polystyrene	MSFC	2.54 cm
M11	TS15 carbon/carbon composite	JSC	2.54 cm
M12	SP16 carbon/carbon composite	JSC	2.54 cm
M13	SP18 carbon/carbon composite	JSC	2.54 cm
M14	Spectrolon—100-percent reflectance	JSC	2.54 cm
M15	Spectrolon—45-percent reflectance	JSC	2.54 cm
M16	Spectrolon—25-percent reflectance	JSC	2.54 cm
M17	Spectrolon—3-percent reflectance	JSC	2.54 cm
M18	Polyphosphazene-Zot paint	JSC	2.54 cm
M19	Cassini—thermal control—HINCOR	JSC	2.54 cm

Table 2(a). 333 K (60°C) Heated Tray Samples

Sample Code	Material	Size
TS15b	TS15 carbon/carbon composite	2.54 cm
SP16b	SP16 carbon/carbon composite	2.54 cm
SP18b	SP18 carbon/carbon composite	2.54 cm

Table 2(b). 473 K (200°C) Heated Tray Samples

Sample Code	Material	Size
TS15a	TS15 carbon/carbon composite	2.54 cm
SP16a	SP16 carbon/carbon composite	2.54 cm
SP18a	SP18 carbon/carbon composite	2.54 cm

Table 3. Heated Strip Samples

333 K (60°C)	473 K (200°C)
ICI Resin - Base polymer	ITO-coated Kapton
ICI Resin - Siloxane modified	Carbon-coated Kapton
ITO-coated Kapton	SiO <sub>2</sub> -coated Kapton
Carbon-coated Kapton	Germanium-coated Kapton
SiO <sub>2</sub> -coated Kapton	Kapton
Germanium-coated Kapton	
Kapton	

Table 4. Scatterometer Samples

Reactive Target Materials	Scattering Surfaces	Size
Highly oriented pyrolytic graphite	$^{13}\text{C}$ on carbon/carbon composite	1.3 cm
Highly oriented pyrolytic graphite	Aluminum	1.3 cm
Kapton	Aluminum	1.3 cm
Kapton	Polyethylene	1.3 cm
Kapton	$\text{SiO}_2$	1.3 cm
Kapton	$^{13}\text{C}$ on carbon/carbon composite	1.3 cm

Table 5. Solar UV Experiment

Sample Code	Material	Size
SUV1	Polysulfone Udel 1700	2.54 cm
SUV2	Polymethylmethacrylate standard	1.3 cm
SUV3	Teflon AF 1600	1.3 cm
SUV4	Polystyrene standard	1.3 cm

Table 6. Variable Exposure Experiment

Sample Code	Material	Size
VEE1	Highly oriented pyrolytic graphite on $^{13}\text{C}$ -coated C/C	1.3 cm
VEE2	Boron nitride on silicon	1.3 cm

## **Appendix B**

### **Mass Data**

<b>PASSIVE TRAY SAMPLES</b>			
<b>Material</b>	<b>Pre-flight (g)</b>	<b>Post-flight (g)</b>	<b>Mass Change (g)</b>
Polystyrene (PS)	0.01769	0.01492	-0.00277
Polystyrene (ground)	0.014046	0.011047	-0.002999
Backbone fluorinated PS	0.03588	0.03488	-0.00100
Ring fluorinated PS	0.01624	0.01447	-0.00177
TS15 C/C	1.70014	1.69778	-0.00236
SP16 C/C	1.74578	1.74457	-0.00121
SP18 C/C	1.72103	1.72027	-0.00076
Spectrolon-100% refl.	3.10628	3.10643	0.00015
Spectrolon-45% refl.	2.52925	2.52941	0.00016
Spectrolon-25% refl.	2.47194	2.47202	0.00008
Spectrolon- 3% refl.	2.06116	2.06198	0.00082
Polyphosphazene-ZOT	2.49990	2.49989	-0.00001
HINCOR thermal control paint	2.17340	2.17317	-0.00023

<b>HEATED STRIP SAMPLES</b>			
<b>Material</b>	<b>Pre-flight (g)</b>	<b>Post-flight (g)</b>	<b>Mass Change (g)</b>
ICI - base cyanate - flight (60C)	0.14956	0.14710	-0.00246
ICI - base cyanate - ground	0.114336	0.110935	-0.003401
ICI - modified cyanate - flight (60C)	0.15048	0.14992	-0.00056
ICI - modified cyanate - ground	0.118713	0.118229	-0.000484

<b>SCATTEROMETER SAMPLES</b>			
<b>Material/Scattering Surface</b>	<b>Pre-flight (g)</b>	<b>Post-flight (g)</b>	<b>Mass Change (g)</b>
Kapton/Aluminum	0.00828	0.00838	0.00010
Kapton/Polyethylene	0.00829	0.00830	0.00001
Kapton/SiO2	0.00823	0.00842	0.00019
Kapton/13C on C/C	0.00801	0.00802	0.00001

<b>SOLAR UV EXPERIMENT SAMPLES</b>			
<b>Material</b>	<b>Pre-flight (g)</b>	<b>Post-flight (g)</b>	<b>Mass Change (g)</b>
Polysulfone - day	0.03382	0.03233	-0.00149
Polysulfone - night	0.03474	0.03396	-0.00078
Polysulfone - both	0.02100	0.01901	-0.00199
PMMA - day	0.00738	0.00681	-0.00057
PMMA - night	0.00735	0.00677	-0.00058
PMMA - both	0.00478	0.00367	-0.00111
PMMA - ground	0.006440	0.005484	-0.000956
Polystyrene - day	0.00685	0.00649	-0.00036
Polystyrene - night	0.00455	0.00458	0.00003
Polystyrene - both	0.00470	0.00413	-0.00057
Polystyrene - ground	0.006457	0.005910	-0.000547

<b>CAROUSEL SAMPLE: 13C-KAPTON</b>				
<b>Panel</b>	<b>Pre-coat (g)</b>	<b>Pre-bake (g)</b>	<b>Post-bake (g)</b>	<b>Post-flight (g)</b>
Side 1	215.8	216.0	216.0	216.0
Side 2	210.9	211.4	211.4	211.4
45 degree	115.9	116.8	116.66	116.7
Bottom	319.2	321.0	320.95	320.9





## **Appendix C**

### **ESCA Data**

# PASSIVE TRAY EXPERIMENT

M1

Amorphous teflon 1600		
<u>Element</u>	12/3/92 Control <u>Atom%</u>	12/3/92 Flight <u>Atom%</u>
C	32.31	32.57
O	10.54	10.86
F	57.15	56.57

M2

Amorphous teflon 2400		
<u>Element</u>	12/3/92 Control <u>Atom%</u>	12/3/92 Flight <u>Atom%</u>
C	32.15	11.81
O	12.26	55.87
F	55.59	0.00
Si	0.00	31.01
Na	0.00	1.32

M6

Polystyrene			
<u>Element</u>	12/3/92 Control <u>Atom%</u>	12/3/92 Flight <u>Atom%</u>	2/2/93 Ground <u>Atom%</u>
C	94.53	65.43	69.79
O	5.47	25.21	22.06
Si	0.00	7.89	0.00
N	0.00	1.47	0.00
F	0.00	0.00	4.25
Cu	0.00	0.00	2.01
Na	0.00	0.00	1.89

M7

Backbone-fluorinated Polystyrene		
<u>Element</u>	12/3/92 Control <u>Atom%</u>	12/3/92 Flight <u>Atom%</u>
C	70.19	56.75
O	4.44	17.61
Si	3.83	3.24
F	21.54	20.21
N	0.00	2.19

M8

Ring-fluorinated Polystyrene		
<u>Element</u>	12/3/92 Control <u>Atom%</u>	12/3/92 Flight <u>Atom%</u>
C	58.90	56.15
O	2.33	15.20
N	0.00	3.23
F	38.77	25.43

## PASSIVE TRAY EXPERIMENT - continued

M14

Spectrolon - 100% reflectance		
<u>Element</u>	12/16/92 Control <u>Atom%</u>	12/16/92 Flight <u>Atom%</u>
Si	0.00	2.07
C	32.30	30.67
O	0.00	4.25
F	67.70	63.01

M15

Spectrolon - 45% reflectance		
<u>Element</u>	12/16/92 Control <u>Atom%</u>	12/16/92 Flight <u>Atom%</u>
Si	0.00	0.97
C	32.41	31.35
O	0.00	2.48
F	67.59	65.20

M16

Spectrolon - 25% reflectance		
<u>Element</u>	12/16/92 Control <u>Atom%</u>	12/16/92 Flight <u>Atom%</u>
C	32.47	31.62
O	0.00	0.89
F	67.53	67.50

M17

Spectrolon - 3% reflectance		
<u>Element</u>	12/16/92 Control <u>Atom%</u>	12/16/92 Flight <u>Atom%</u>
C	35.39	32.57
O	0.00	2.20
F	64.61	65.23

M18

Polyphosphazene-ZOT paint		
<u>Element</u>	12/5/92 Control <u>Atom%</u>	12/5/92 Flight <u>Atom%</u>
P	5.79	8.74
C	30.40	23.37
N	5.18	5.86
O	10.51	25.25
F	48.12	30.52
Si	0.00	3.21
Zn	0.00	1.74
Na	0.00	1.31

M19

Cassini-HINCOR thermal control		
<u>Element</u>	12/5/92 Control <u>Atom%</u>	12/5/92 Flight <u>Atom%</u>
Si	25.36	23.69
C	5.39	5.81
K	9.00	9.26
O	58.27	59.27
Zn	1.98	1.97

# PASSIVE and HEATED TRAY EXPERIMENTS

M11

TS15 C/C composite				
<u>Element</u>	<u>12/16/92 Control Atom%</u>	<u>12/16/92 Passive Atom%</u>	<u>1/21/93 60 C Atom%</u>	<u>1/21/93 200 C Atom%</u>
C	84.02	81.13	77.42	81.06
O	11.74	14.92	18.19	15.37
N	1.78	0.00	0.00	0.00
Si	1.09	2.48	3.30	2.98
Ca	0.75	0.00	0.00	0.00
Na	0.37	0.82	1.09	0.58
Cl	0.25	0.00	0.00	0.00
F	0.00	0.65	0.00	0.00

M12

SP16 C/C composite				
<u>Element</u>	<u>12/16/92 Control Atom%</u>	<u>12/16/92 Passive Atom%</u>	<u>1/21/93 60 C Atom%</u>	<u>1/21/93 200 C Atom%</u>
C	82.05	81.25	75.03	76.40
O	13.64	15.07	20.77	18.47
Al	2.10	0.00	0.00	0.00
Si	1.68	3.09	3.74	3.36
Cl	0.53	0.00	0.00	0.00
Na	0.00	0.59	0.46	1.77

M13

SP18 C/C composite				
<u>Element</u>	<u>12/16/92 Control Atom%</u>	<u>12/16/92 Passive Atom%</u>	<u>1/21/93 60 C Atom%</u>	<u>1/21/93 200 C Atom%</u>
C	92.50	77.66	73.00	76.81
O	6.16	17.23	20.66	17.16
Si	0.81	4.48	5.57	3.78
Cl	0.53	0.00	0.00	0.00
Na	0.00	0.63	0.77	1.74
P	0.00	0.00	0.00	0.51

# HEATED STRIP EXPERIMENT

Kapton HN					
<u>Element</u>	2/20/92 Control	1/25/93 60 C	5/28/93 60 C	1/25/93 200 C	5/28/93 200 C
	<u>Atom%</u>	<u>Atom%</u>	<u>Atom%</u>	<u>Atom%</u>	<u>Atom%</u>
C	77.30	64.20	67.88	59.92	53.57
O	16.24	23.94	22.74	25.79	32.31
N	6.46	7.19	6.89	7.56	5.04
Si	0.00	2.84	2.49	3.27	9.08
Na	0.00	1.83	0.00	2.98	0.00
Cl	0.00	0.00	0.00	0.48	0.00

ITO coated Kapton			
<u>Element</u>	1/22/93 Control	1/22/93 60 C	1/22/93 200 C
	<u>Atom%</u>	<u>Atom%</u>	<u>Atom%</u>
C	51.22	20.81	18.49
In	14.58	12.36	11.27
Sn	2.48	1.93	1.79
O	31.72	50.17	53.02
Si	0.00	14.73	15.44

Carbon coated Kapton			
<u>Element</u>	1/22/93 Control	1/22/93 60 C	1/22/93 200 C
	<u>Atom%</u>	<u>Atom%</u>	<u>Atom%</u>
C	77.04	70.82	67.71
N	6.52	3.41	4.02
O	16.44	20.71	21.97
Al	0.00	1.90	2.50
Si	0.00	1.59	2.52
Na	0.00	1.57	1.28

## HEATED STRIP EXPERIMENT - continued

SiO <sub>2</sub> coated Kapton			
<u>Element</u>	1/25/93 Control Atom%	1/25/93 60 C Atom%	1/25/93 200 C Atom%
Si	29.67	30.59	18.27
C	12.41	8.85	25.40
N	0.00	0.98	0.00
O	54.71	57.26	45.75
F	2.53	1.16	1.65
Ca	0.68	0.00	1.73
Na	0.00	1.16	7.20

Germanium coated Kapton					
<u>Element</u>	12/9/92 Control Atom%	1/22/93 60 C Atom%	5/28/93 60 C Atom%	1/22/93 200 C Atom%	5/28/93 200 C Atom%
Ge	37.73	18.94	18.93	30.57	29.86
C	18.85	11.73	11.44	10.98	11.37
O	40.76	53.38	54.06	50.15	49.61
Si	0.00	15.95	15.56	8.30	9.17
Na	2.66	0.00	0.00	0.00	0.00

ICI Base Cyanate (BCY)			
<u>Element</u>	1/25/93 Control Atom%	1/25/93 60 C Atom%	2/2/93 Ground Atom%
Si	2.66	3.71	0.00
C	77.90	69.68	62.31
N	3.94	6.70	6.54
O	14.19	19.90	24.05
F	1.31	0.00	3.87
Cu	0.00	0.00	1.67
Na	0.00	0.00	1.56

ICI Modified Cyanate (MCY)			
<u>Element</u>	1/25/93 Control Atom%	1/25/93 60 C Atom%	2/2/93 Ground Atom%
Si	4.91	24.08	28.48
C	76.69	18.98	3.68
N	4.71	3.13	0.00
O	12.44	53.00	56.58
F	1.25	0.81	9.43
S	0.00	0.00	1.32
Cu	0.00	0.00	0.52

# SCATTEROMETER EXPERIMENT

HOPG	
Element	1/21/93 Control Atom%
Au	0.22
Hg	0.10
Si	0.00
C	95.83
O	3.85

HOPG/Aluminum	
Element	1/26/93 Flight Atom%
Au	0.00
Hg	0.00
Si	1.67
C	86.37
O	11.96

HOPG /13Carbon on C/C	
Element	1/26/93 Flight Atom%
Au	0.19
Hg	0.00
Si	1.38
C	78.14
O	16.47
N	3.82

Kapton	
Element	2/20/92 Control Atom%
Si	0.00
C	77.30
N	6.46
O	16.24
F	0.00

Kapton/Aluminum	
1/27/93 Flight Atom%	5/28/93 Flight Atom%
0.97	0.94
68.97	69.44
6.36	6.48
22.88	20.56
0.82	2.58

Kapton/Polyethylene		
Element	1/27/93 Flight Atom%	5/28/93 Flight Atom%
Si	1.10	4.89
C	70.88	71.65
N	6.37	5.96
O	21.66	17.50

Kapton/SiO2		
Element	1/27/93 Flight Atom%	5/28/93 Flight Atom%
Si	0.99	6.30
Cl	0.28	0.00
C	76.45	71.81
N	5.26	4.54
O	15.60	17.35
F	1.43	0.00

Kapton/13Carbon on C/C		
Element	1/27/93 Flight Atom%	5/28/93 Flight Atom%
Si	1.75	7.61
C	66.80	63.54
N	7.01	4.53
O	23.31	24.32
F	1.12	0.00

# SOLAR ULTRA-VIOLET EXPERIMENT (SUV)

Polysulfone Udel 1700				
<u>Element</u>	12/2/92 Control <u>Atom%</u>	12/2/92 SUV1a <u>Atom%</u>	12/2/92 SUV1b <u>Atom%</u>	12/2/92 SUV1d <u>Atom%</u>
S	2.09	3.73	3.82	4.18
C	84.24	74.27	73.72	67.29
O	13.67	19.39	19.52	21.51
N	0.00	2.62	0.85	7.01
Si	0.00	0.00	2.09	0.00

Polymethymethacrylate standard					
<u>Element</u>	12/2/92 Control <u>Atom%</u>	12/2/92 SUV2a <u>Atom%</u>	12/2/92 SUV2b <u>Atom%</u>	12/2/92 SUV2d <u>Atom%</u>	3/8/93 SUV2e <u>Atom%</u>
C	73.27	71.32	69.02	69.93	58.23
O	24.96	27.82	28.53	28.73	35.03
Cs	1.77	0.87	0.79	1.35	1.24
Si	0.00	0.00	1.65	0.00	2.21
F	0.00	0.00	0.00	0.00	2.24
Cu	0.00	0.00	0.00	0.00	1.05

Amorphous Teflon AF 1600				
<u>Element</u>	12/16/92 Control <u>Atom%</u>	12/16/92 SUV3a <u>Atom%</u>	12/16/92 SUV3b <u>Atom%</u>	12/16/92 SUV3d <u>Atom%</u>
Al	1.98	1.64	2.38	0.00
C	38.23	17.71	10.45	10.68
O	38.34	49.53	56.15	57.77
N	2.06	3.06	1.09	0.00
Si	19.39	23.92	27.25	30.30
K	0.00	1.14	0.59	0.00
F	0.00	1.63	0.86	1.26
Na	0.00	1.38	1.24	0.00



## SOLAR ULTRA-VIOLET EXPERIMENT - continued

Polystyrene standard					
<u>Element</u>	12/2/92 Control <u>Atom%</u>	12/2/92 SUV4a <u>Atom%</u>	12/2/92 SUV4b <u>Atom%</u>	12/2/92 SUV4d <u>Atom%</u>	3/8/93 SUV4e <u>Atom%</u>
C	94.18	86.66	80.03	80.13	68.97
O	5.82	13.34	17.73	15.90	24.03
Si	0.00	0.00	1.45	1.82	1.39
Na	0.00	0.00	0.79	0.00	0.00
N	0.00	0.00	0.00	2.15	0.00
S	0.00	0.00	0.00	0.00	1.30
F	0.00	0.00	0.00	0.00	2.74
Cu	0.00	0.00	0.00	0.00	1.57

## VARIABLE EXPOSURE EXPERIMENT

HOPG/13C coating on C/C		
<u>Element</u>	1/21/93 Control <u>Atom%</u>	1/21/93 Flight <u>Atom%</u>
Au	0.22	0.00
Hg	0.10	0.00
C	95.83	80.13
O	3.85	15.13
Si	0.00	3.28
Na	0.00	1.47

BN on silicon		
<u>Element</u>	1/21/93 Control <u>Atom%</u>	1/21/93 Flight <u>Atom%</u>
B	45.53	20.96
C	8.08	8.85
N	42.52	17.34
O	3.59	36.87
Xe	0.28	0.00
Si	0.00	15.98



1. Report No. JPL Pub. 94-31	2. Government Accession No.	3. Recipient's Catalog No.	
4. Title and Subtitle NASA/JPL Evaluation of Oxygen Interaction with Materials-3 (EOIM-3) Final Report		5. Report Date December 1994	
		6. Performing Organization Code	
7. Author(s) David E. Brinza, Shirley Y. Chung, Timothy K. Minton, Ranty H. Liang		8. Performing Organization Report No.	
9. Performing Organization Name and Address JET PROPULSION LABORATORY California Institute of Technology 4800 Oak Grove Drive Pasadena, California 91109		10. Work Unit No.	
		11. Contract or Grant No. <del>NASA</del> NAS7-1260	
		13. Type of Report and Period Covered	
12. Sponsoring Agency Name and Address NATIONAL AERONAUTICS AND SPACE ADMINISTRATION Washington, D.C. 20546		14. Sponsoring Agency Code RF65 EY23303020828	
15. Supplementary Notes			
16. Abstract <p>The deleterious effects of hyperthermal atomic oxygen (AO) found in low-Earth-orbit (LEO) environments on critical flight materials has been known since early Shuttle flights. This corrosive effect is of considerable concern because it compromises the performance and longevity of spacecraft/satellite materials deployed for extended periods in LEO.</p> <p>The NASA Evaluation of Oxygen Interactions with Materials-3 (EOIM-3) experiment served as a testbed for a variety of candidate flight materials for space assets. A total of 57 JPL test specimens were present in six subexperiments aboard EOIM-3. In addition to a number of passive exposure materials for flight and advanced technology programs, several subexperiments were included to provide data for understanding the details of atomic oxygen interactions with materials. Data and interpretations are presented for the heated tray, heated strips, solar ultraviolet exposure, and scatterometer subexperiments, along with a detailed description of the exposure conditions experienced by materials in the various experiments.</p> <p>Mass spectra of products emerging from identical samples of a <sup>13</sup>C-enriched polyimide polymer (chemically equivalent to Kapton) under atomic oxygen bombardment in space and in the laboratory were collected. Reaction products unambiguously detected in space were <sup>13</sup>CO, NO, <sup>12</sup>CO<sub>2</sub>, and <sup>13</sup>CO<sub>2</sub>. These reaction products and two others, H<sub>2</sub>O and <sup>12</sup>CO, were detected in the laboratory, along with inelastically scattered atomic and molecular oxygen. Qualitative agreement was seen in the mass spectra taken in space and in the laboratory; the agreement may be improved by reducing the fraction of O<sub>2</sub> in the laboratory molecular beam.</p>			
17. Key Words (Selected by Author(s)) * atomic oxygen * materials * EOIM-3		18. Distribution Statement	
19. Security Classif. (of this report)	20. Security Classif. (of this page)	21. No. of Pages	22. Price

